Measurement of Hadronic Cross Sections
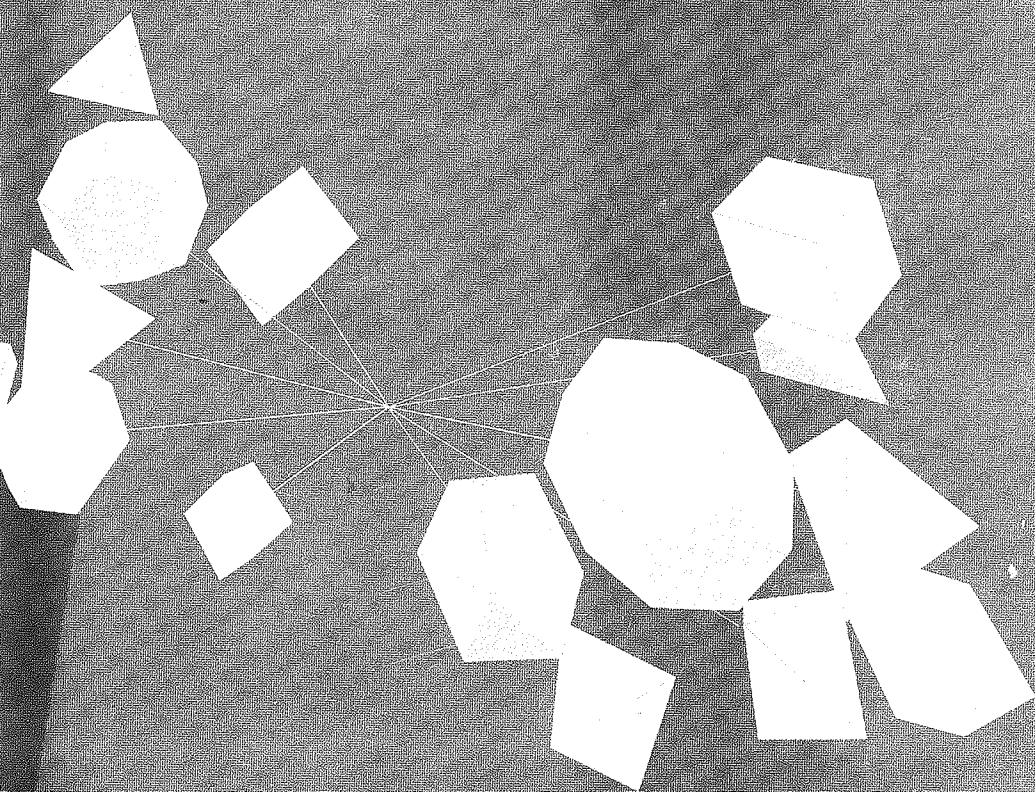# and Asymmetries on the Z-Resonance

Measurement of Hadronic Cross Sections and Asymmetries on the Z-Resonance

Measurement of Hadronic Cross Sections and Asymmetries on the Z-Resonance

Een wetenschappelijke proeve op het gebied
van de Natuurwetenschappen.

Proefschrift

ter verkrijging van de graad van doctor
aan de Katholieke Universiteit Nijmegen,
volgens besluit van het College van Decanen
in het openbaar te verdedigen
op dinsdag 17 december 1996,
des namiddags om 3.30 uur precies,

door

Hendrikus Petrus Kuijten

geboren op 30 april 1969 te Lommel.

Promotores: **Prof. Dr. R.T. Van de Walle**
Prof. Dr. E.W. Kittel

Co-promotor: **Dr. D.J. Schotanus**

Manuscriptcomissie: **Dr. G.J. Bobbink**
Dr. F. Filthaut

Acknowledgements

Contents

Introduction

For many centuries mankind has been fascinated by the question of what are the smallest constituents of matter. Ancient Greek philosophers already reasoned that matter should consist of smallest pieces called "atoms", a philosophy which turned out to be successful in the 19th century. During the 20th century, it was discovered that atoms themselves are microsystems of protons and neutrons centered in a small core, surrounded by electrons in orbits around this core.

The well-understood electromagnetic force explains the interactions between the electrons and the nucleus. The strong force describes the interactions between nucleons and the stability of the nucleus. The decay of heavy nuclei resulted in the discovery of the force known as the weak interaction.

In the decades following World War II, a large amount of particles were discovered, thought to be elementary, which gave more insight in the nature of the strong and the weak forces. The discovery of quarks as constituents of nucleons reduced the variety of "elementary" particles. The notion that not just electromagnetism but all forces could be interpreted as the result of the exchange of virtual boson quanta got confirmed; the gluon and the intermediate bosons W and Z became for the strong respectively the weak interaction what the photon was to the electromagnetic one. Insight in the dynamics of gluon exchange led to Quantum Chromo Dynamics (QCD). The unification of the electromagnetic and weak forces led to a prediction of the masses of the W and Z bosons; their discovery in 1983 at CERN was a major triumph for this model. The subsequent unification of the electroweak and the strong forces resulted in the theory presently known as the Standard Model.

Nowadays, the LEP accelerator at CERN allows high precision tests of the Standard Model. In its so-called Phase I stage (LEP-1), LEP has been running since 1989 at center-of-mass (CM) energies near the Z-resonance. In 1996, LEP entered its Phase II stage (LEP-2), running at energies above the W^+W^--threshold.

This thesis deals with LEP-1 data, collected at the L3 experiment in 1992 and 1993, specifically data on the reaction $e^+e^- \rightarrow \gamma/Z \rightarrow q\bar{q}$, i.e. the hadronic decay channel of the Z resonance. There have been several measurements of the total cross section of this reaction, but few of its forward-backward asymmetry – and none using the L3 data. Although inherently less precise when integrated over all quark species, the forward-backward asymmetry is an important quantity to determine for reasons of completeness. We will redetermine the hadronic cross section, but

1

a major part of our analysis will be devoted to measuring the forward-backward asymmetry associated with this reaction.

In chapter 1, the Standard Model description of the hadronic cross section and asymmetry are reviewed. Chapter 2 describes the experimental setup of LEP and the L3 experiment; an overview of the L3 event reconstruction programs is given. The necessary ingredients required to obtain a real detector simulation are presented in chapter 3. The selection criteria applied to obtain a hadron sample for cross section and forward-backward asymmetry measurements are discussed in chapter 4. The cross section and forward-backward asymmetries obtained are presented in chapter 5 and 6, respectively. Chapter 7 interprets these measurements in the framework of the Standard Model.

Unless specified otherwise, all quantities used in this thesis are expressed in so-called natural units based on choosing $\hbar = c = 1$.

1

Theory

The Standard Model has become a well established theory describing the unified electromagnetic, weak and strong forces. Its Lagrangian is based on the group symmetry $SU(3)_C \times SU(2)_L \times U(1)_Y$, which unites the the strong, the weak and the electromagnetic force. The carriers of these forces are the the gluon, the massive vector bosons Z and W, and the photon, respectively. In particular, the Lagrangian contains the particles onto which these boson carriers act. These particles are the quarks and leptons; they are ordered in three families. Each family is subdivided in weak isospin doublets of left-handed quarks or leptons and weak isospin singlets of right-handed quarks or leptons. In addition to an electric charge, quarks have a colour "charge". Each exchanged gluon carries a specific colour-anticolour charge combination.

The requirement of renormalisability allows mass terms of the fermions in the Lagrangian, but not of the gauge bosons. However, the masses of the latter can be brought into the picture by means of the so-called (spontaneous symmetry breaking) Higgs mechanism. It is based on the assumption of the existence of an all-pervasive Higgs field, the quantum of which is called the Higgs boson. The Higgs field is assumed to be responsible for the generation of the fermion as well as the boson masses.

On the level of the Standard Model, the masses of the leptons and the quarks are just input parameters. Experimentally the lepton masses (or in the case of neutrinos their upper limits) are relatively well known. This in contrast with the masses of quarks, due to the fact that they cannot be observed freely in nature. The masses of the light quarks are dependent on the models used to estimate them and still controversial [1]. They are generally assumed to be in the 1-10 MeV range for the d and u quark and in the 100-300 MeV range for the s quark. From the masses of the mesons containing the heavy c and b quarks one estimates c and b quark masses in the ranges of 1.2-1.9 GeV and 4.5-4.9 GeV, respectively [1]. In recent measurements at Fermilab, the mass of the top quark was found to be in the range 169-181 GeV [2].

3

From LEP-1 experiments, the mass of the Z boson is measured at the subpermille level (see chapter 7). The world average for the mass of the W boson currently lies at (80.32 ± 0.19) GeV. The 1996 LEP-2 running yielded a preliminary value of $(80.4\pm0.2\pm0.1)$ GeV [3]. From LEP-1 data, one has also been able to set a lower limit on the mass of the scalar Higgs boson of about 60 GeV at 95% confidence level [1].

In the following sections, a short summary of the relevant quantities and their relations, as derived from the Lagrangian, is presented. In the first section, the most relevant parameters are introduced. In the second, the differential cross section for $e^+e^- \rightarrow f\bar{f}$ is derived. In the third section, the radiative corrections and their effect on the total cross section and forward-backward asymmetry is discussed. The last section shortly describes the process $q\bar{q} \rightarrow$ hadrons.

1.1   Parameters of the Electroweak Lagrangian

The electroweak Standard Model Lagrangian contains gauge boson and fermion kinetic energy terms, self-interaction terms and current terms arising from the fermion interactions with the gauge bosons. The current terms are the electromagnetic current (the photon exchange), the charged weak current (the W exchange) and the neutral weak current (the Z exchange).

The $SU(2)_L \times U(1)_Y$ symmetry does not allow boson mass field terms in the electroweak Lagrangian, as these would not be local gauge invariant under the implied group transformation. However, as stated above, a solution was found by means of the hypothesis of the Higgs mechanism. Two gauge invariant terms are added to the Lagrangian, representing the Higgs field kinetic energy and the Higgs field potential, respectively. The minimum of this potential leads to non-zero mass vacuum expectation values and a corresponding set of ground states. Nature selects a specific ground state, thus breaking down the symmetry. As a result, terms show up in the ground energy state which simulate the effect of boson-fields in the Lagrangian.

The relation between the basic $SU(2)_L$ and $U(1)_Y$ fields and the physical W, Z and γ fields can be expressed in terms of a mixing angle θ_W. By means of the Higgs mechanism, θ_W can be directly related to the masses M_W and M_Z of the W and Z boson, respectively:

$$\cos \theta_W = \frac{M_W}{M_Z}. \tag{1.1}$$

The weak mixing angle is one of the most important parameters of the Standard Model Lagrangian.

The characteristics of the electroweak interactions are contained in the fermion-gauge-boson coupling constants. The electromagnetic current yields a pure vector (V) coupling of the fermion to the photon, whereas in the charged weak current, the

W boson has a pure vector minus axial vector (V-A) coupling to the fermion. The structure of the neutral weak Z-current is again a linear combination of a vector and axial vector coupling, but now with coefficients v_f and a_f depending on both the charge and the weak isospin of the fermion involved. These coefficients are given by:

$$v_f = \frac{I_3 - 2Q_f \sin^2 \theta_W}{2 \sin \theta_W \cos \theta_W}, \tag{1.2}$$

and

$$a_f = \frac{I_3}{2 \sin \theta_W \cos \theta_W}, \tag{1.3}$$

where I_3 is the third component of the weak isospin and Q_f the charge of the fermion. For left-handed fermions, I_3 equals $+\frac{1}{2}$ for the neutrinos and the positively charged quarks and $-\frac{1}{2}$ for the charged leptons and the negatively charged quarks. All right-handed fermions have weak isospin zero.

In practice, one uses the scaled coupling constants g_V^f and g_A^f, defined as:

$$g_V^f = I_3 - 2Q_f \sin^2 \theta_W \quad \text{and} \quad g_A^f = I_3. \tag{1.4}$$

Electroweak interactions can be entirely expressed in terms of the parameters M_Z, M_W, M_H, m_f, together with the QED coupling constant $\alpha(= e^2/4\pi)$. The complete Standard Model (including SU(3)$_C$) also requires to take into account α_s, the strong coupling constant. The parameter M_W is commonly replaced by the much better known parameter G_μ, the muon decay constant. In lowest order these two parameters are related by:

$$M_W^2 \left(1 - \frac{M_W^2}{M_Z^2} \right) = \frac{\pi \alpha}{\sqrt{2} G_\mu}. \tag{1.5}$$

The constant G_μ originates from the old Fermi theory, where the weak interaction was described as a 4-point interaction vertex. In the low energy limit, the W exchange diagram can be replaced by the 4-point vertex of the Fermi model. Relation 1.5 is obtained by requiring that the matrix elements, calculated within these models, agree with each other in the low energy approximation [4]. In this way, the most precisely measured and most independent set of parameters is obtained. The leptonic masses, together with M_Z, G_μ and α are very well known parameters. Less precisely known parameters are, however, the quark masses and especially the Higgs mass.

1.2 Hadronic Differential Cross Sections

At the Born level, the expression for the differential cross section $e^+e^- \to f\bar{f}$ (where f stands for any fermion) reads as follows [5]:

$$\frac{d\sigma_f^0}{d\Omega} = \frac{\alpha^2}{4s} N_C^f \sqrt{1 - 4\mu_f} \cdot$$
$$\cdot \left\{ G_1(s)(1 + \cos^2\theta) + 4\mu_f G_2(s)\sin^2\theta + \sqrt{1 - 4\mu_f}G_3(s) \cdot 2\cos\theta \right\}, \tag{1.6}$$

where s is the CM energy, N_C^f a colour factor arising from QCD (equal to 3 for quarks and to 1 for leptons) and $\mu_f = m_f^2/s^{(1)}$.

In equation 1.6, θ is the angle between the outgoing fermion with the incoming electron. Thus an event is defined as *forward* if the outgoing *fermion* travels in the forward hemisphere $0 < \theta < \frac{1}{2}\pi$ and as *backward* if it does so in the backward hemisphere $\frac{1}{2}\pi < \theta < \pi$.

The functions G_1, G_2, G_3 contain the the coupling constants v_f and a_f and are given by:

$$G_1(s) = Q_f^2 - 2v_e v_f Q_f \text{Re}\chi_0(s) + (v_e^2 + a_e^2)(v_f^2 + a_f^2 - 4\mu_f a_f^2)|\chi_0(s)|^2, \tag{1.7}$$
$$G_2(s) = Q_f^2 - 2v_e v_f Q_f \text{Re}\chi_0(s) + (v_e^2 + a_e^2)v_f^2|\chi_0(s)|^2, \tag{1.8}$$
$$G_3(s) = -2a_e a_f Q_f \text{Re}\chi_0(s) + 4v_e a_e v_f a_f|\chi_0(s)|^2, \tag{1.9}$$

where Q_f is the charge of the final-state fermion. The Breit-Wigner amplitude $\chi_0(s)$ reads:

$$\chi_0(s) = \frac{s}{s - M_Z^2 + iM_Z\Gamma_Z^0}, \tag{1.10}$$

with

$$\Gamma_Z^0 = \sum_f \Gamma_f^0 \tag{1.11}$$

the width of the Z boson and introducing Γ_f, being the partial width for fermion f:

$$\Gamma_f^0 = N_C^f \frac{\alpha}{3} M_Z \sqrt{1 - 4\mu_f} \left[v_f^2(1 + 2\mu_f) + a_f^2(1 - 4\mu_f) \right]. \tag{1.12}$$

In the calculation of expression 1.6, the Z exchange and the γ exchange channels are taken into account. Terms arising from the Higgs exchange are neglected, because of the small coupling of the Higgs particle to the initial-state electrons [7].

---

[1] Equation 1.6 is valid for any fermion, except for the electron-neutrino where there is an additional small contribution from the W exchange, which, near the Z resonance, results in a correction of about 3% to the total cross section [6]

In the expressions 1.7-1.9, terms proportional to Q_f^2 are due to the photon exchange, terms proportional to $|\chi_0(s)|^2$ to the Z-exchange and terms proportional to $Q_f \mathrm{Re}\chi_0(s)$ to the photon-Z interference terms.

In general, if the expression for the differential cross section is ϕ-independent, the total cross section is found by integrating over the polar angle θ:

$$\sigma_f = 2\pi \int_{-1}^{1} \frac{d\sigma_f}{d\Omega} d\cos\theta. \tag{1.13}$$

Defining σ_F and σ_B as the cross section for forward and backward events, respectively:

$$\sigma_{\mathrm{F},f} = 2\pi \int_{0}^{1} \frac{d\sigma_f}{d\Omega} d\cos\theta, \qquad \sigma_{\mathrm{B},f} = 2\pi \int_{-1}^{0} \frac{d\sigma_f}{d\Omega} d\cos\theta, \tag{1.14}$$

the forward-backward asymmetry is given by:

$$A_{\mathrm{FB},f} = \frac{\sigma_{\mathrm{F},f} - \sigma_{\mathrm{B},f}}{\sigma_{\mathrm{F},f} + \sigma_{\mathrm{B},f}}. \tag{1.15}$$

Substitution of equation 1.6 into equations 1.13-1.15 gives the following lowest order expressions for each fermion type:

$$\sigma_f^0(s) = \frac{4\pi\alpha^2}{3s} N_C^f \sqrt{1 - 4\mu_f} \left[G_1(s) + 2\mu_f G_2(s) \right], \tag{1.16}$$

$$A_{\mathrm{FB},f}^0(s) = \frac{3}{4} \frac{G_3(s)}{G_1(s) + 2\mu_f G_2(s)} \sqrt{1 - 4\mu_f}. \tag{1.17}$$

For an energy region around the mass of the Z, the s-dependence of equation 1.16 follows roughly the absolute square of equation 1.10, i.e. a Breit-Wigner resonance cross section, and thus yields the Z line shape. The energy dependence of equation 1.17 can be simplified for $s \approx M_Z^2$ and taking into account that the asymmetry is not measured more precisely than to a few percent. This allows neglecting the mass terms μ_f and terms proportional to Γ_Z^2/M_Z^2 in the asymmetry formulae. The s-dependence of the forward-backward asymmetry can then be expressed as:

$$A_{\mathrm{FB},f}^0(s) = \frac{3}{4} \frac{2v_e a_e}{v_e^2 + a_e^2} \cdot \frac{2v_f a_f}{v_f^2 + a_f^2}$$
$$- \frac{3}{4} \frac{2Q_f a_e a_f}{(v_e^2 + a_e^2)(v_f^2 + a_f^2)} \cdot \left\{ 1 - \frac{4v_e^2 v_f^2}{(v_e^2 + a_e^2)(v_f^2 + a_f^2)} \right\} \cdot \left(1 - \frac{M_Z^2}{s} \right). \tag{1.18}$$

The first term in equation 1.18 is due to the Z-exchange, whereas the second one follows from the $\gamma - Z$ interference.

In the case of the hadronic process $e^+ e^- \to q\bar{q}$, the total hadronic cross section and total forward-backward asymmetry are given in terms of a linear sum over all quark flavours $f = q$:

$$\sigma_\mathrm{h} = \sum_{q=d,u,s,c,b} \sigma_q \tag{1.19}$$

and

$$A_{\text{FB,h}} = \sum_{q=d,u,s,c,b} f_q \cdot A_{\text{FB},q} = \sum_{q=d,u,s,c,b} \frac{\sigma_q}{\sigma_{\text{h}}} \cdot A_{\text{FB},q} \qquad (1.20)$$

where f_q is the fraction of q-flavour production with respect to the total quark production.

The forward-backward asymmetry is not a directly measurable quantity as we cannot always distinguish fermion from anti-fermion. A related quantity which is directly observable is the forward-backward *charge* asymmetry. Its determination is based on the angle between the incident electron and the final state quarks of *negative* charge. The forward-backward charge asymmetry is then given by:

$$A_{\text{FB,h}}^{ch} = f_d A_{\text{FB},d} - f_u A_{\text{FB},u} + f_s A_{\text{FB},s} - f_c A_{\text{FB},c} + f_b A_{\text{FB},b}, \qquad (1.21)$$

where the f_q and $A_{\text{FB},q}$ are the quantities defined in equation 1.20 and 1.15, respectively and the u quark and c quark now contribute with an opposite sign. Using this definition, an event is *forward* if the quark with the negative charge travels in the forward direction and *backward* if the opposite is the case[2].

1.3   Radiative Corrections

Expressions 1.6 to 1.20 are calculated at the tree level, i.e. in lowest order. They do not agree with the real, measured data. The lowest order process $e^+e^- \to Z/\gamma \to f\bar{f}$ is modified by the so-called radiative processes. These radiative processes have to be taken into account in order to arrive at predictions which can be compared to observables.

A natural separation between the different types of radiative corrections follows from the renormalisation scheme. In the $SU(2)_L \times U(1)_Y$ symmetry, the "on-shell" scheme naturally distinguishes two gauge invariant subclasses of radiative corrections. For the $q\bar{q}$ final state, a third class appears, associated with the $SU(3)_C$ symmetry. Thus, the radiative corrections to the Born expression for the total hadronic cross section and forward-backward asymmetry can be subdivided into three categories:

- "QED corrections": these involve all diagrams where an extra photon line is attached to the Born diagram, either as a real brehmsstrahlung photon or as a virtual photon. They have by far the largest effect on the cross section but less so on the forward-backward asymmetry.

---

[2] Instead of determining the asymmetry in the production angle of the negatively charged quarks, several recent papers have resorted to measuring the net mean difference in jet charge measured in the forward and backward event hemispheres $< Q_F - Q_B > = < Q_{\text{FB}} >$ resulting from this asymmetry. Both $A_{\text{FB,h}}^{ch}$ and $< Q_{\text{FB}} >$ depend in a "diluted" way on $\sin^2 \theta_W$. For details see e.g. the OPAL [8] and ALEPH [9] publications.

- "Weak corrections": these concern the subset of diagrams with an additional internal massive vector boson attached to the Born diagram. For LEP-1 energies, only the virtual boson exchange is important, because the brehmsstrahlung process is suppressed by the large mass of the W and Z bosons. The effect of the weak corrections on the cross section is small but significant for the forward-backward asymmetry. They provide the most interesting physics, since they depend on the top quark mass and, although less sensitively, also on the Higgs boson mass.

- QCD corrections: these consists of all diagrams, with one or more gluons radiated by the final-state $q\bar{q}$ pair. The calculation of QCD corrections is rather complex, since the QCD coupling constant α_s is large and strongly depends on the energy. However, their influence both on the total cross section and the forward-backward asymmetry is not large; QCD corrections are of the order of a few percent only. Note that it are the QCD corrections which introduce α_s into our parameterisations.

In principle, the order up to which the corrections have to be calculated, depends on the precision of the experiment and the strength of the relevant coupling constant. The higher the precision and the stronger the coupling constant, the more orders to be taken into account. Since the first order QED corrections give a significant contribution (about 30%) to the Born cross section, QED corrections must be calculated up to second order. Weak corrections are calculated up to first order, which is sufficient for the cross section and the forward-backward asymmetry. Due to the size of α_s, QCD corrections have to be calculated to at least third order. Their accuracy is however limited by the difficulty of the calculations; results which take into account quark-mass effects are available only up to $O(\alpha_s)$. Recently however, the radiative corrections were calculated up to $O(\alpha_s^3)$ in the light quark $(m_q^2/s << 1)$ and the heavy quark $(m_q^2/s >> 1)$ approximation, respectively [10].

Radiative processes also modify the relation between M_W, M_Z and G_μ. Relation 1.5 is replaced by:

$$M_W^2 \left(1 - \frac{M_W^2}{M_Z^2}\right) = \frac{\pi\alpha(0)}{\sqrt{2}G_\mu} \frac{1}{1 - \Delta r}, \qquad (1.22)$$

where Δr contains all the one-loop corrections to the muon decay. In equation 1.22 we have maintained the QED coupling constant at its lowest order value as used in equation 1.5 – and therefore called it $\alpha(0)$ – and absorbed all its higher order corrections (i.e. its running) into Δr. Having fixed α, G_μ and M_Z, the practical consequence is a small change in M_W (and thus $\sin^2\theta_W$). Δr is discussed in more detail in the next subsection.

1.3.1   Weak Corrections

Three types of weak corrections can be distinguished:

- Propagator Corrections: The Z/γ propagator contains a fermion loop, primarily resulting in Z and γ self-energy contributions. However, as a consequence of this loop, also $\gamma - Z$ mixing terms arise, with a Z exchange on one side and a γ exchange on the other (see figure 1.1). Propagator corrections constitute the largest weak corrections and are of the order of a few percent.
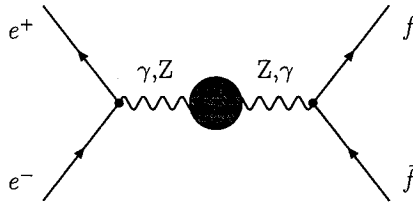
Figure 1.1: *Weak propagator corrections to the Born diagram $e^+e^- \rightarrow f\bar{f}$.*

- Vertex corrections: They are applied both to the electromagnetic and neutral weak current vertex and are illustrated in figure 1.2. The final-state corrections are sensitive to the effects of the exchange of the W boson. For light quarks these effects amount to about 1%. For the $b\bar{b}$ final state, they increase to about 2.5%, in essence because of the contributions from the heavy top-quark (see figure 1.3).
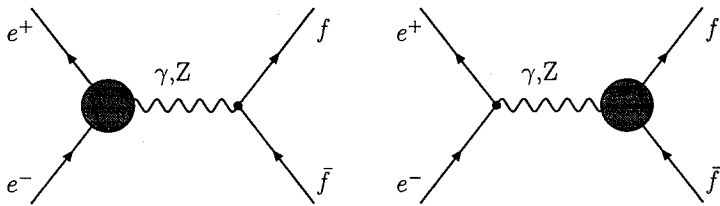
Figure 1.2: *Vertex Corrections to $e^+e^- \rightarrow f\bar{f}$.*
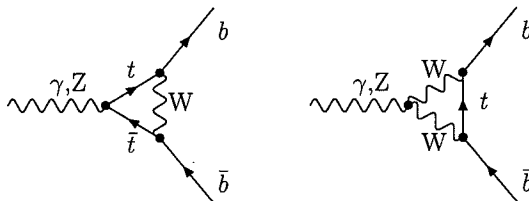
Figure 1.3: *Examples of final-state vertex corrections for the $b\bar{b}$ final state.*

- Box corrections: Box diagrams arise, when in addition to the primary massive vector boson propagator, a second vector boson is exchanged between the initial and final fermion (see figure 1.4). At LEP-1 energies, box corrections are negligibly small, since the massive gauge bosons are generally off-resonance.
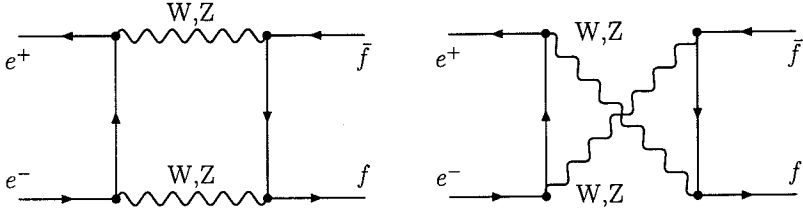
Figure 1.4: *Box Diagrams for $e^+e^- \rightarrow f\bar{f}$.*

Propagator and vertex corrections are taken into account by using what is called the improved Born approximation [5]. It is obtained through the following replacements:

- the weak mixing angle $\sin^2 \theta_W$ in equations 1.2 and 1.3 by an *effective* weak mixing angle

$$\sin^2 \bar{\theta}_W = \sin^2 \theta_W + \cos^2 \theta_W \Delta\rho; \tag{1.23}$$

- the imaginary part of the denominator of the Breit-Wigner amplitude $\chi(s)$ in equation 1.10 by $is\Gamma_Z^{\text{phys}}/M_Z$;

- the coupling constants g_V^f, g_A^f in equations 1.7-1.9 by *effective* coupling constants $\bar{g}_V^f = \sqrt{\rho}(I_3 - Q_f \sin^2 \bar{\theta}_W)$ and $\bar{g}_A^f = \sqrt{\rho}I_3$, respectively.

In these replacements the new variables $\Delta\rho$, Γ_Z^{phys} and ρ are introduced. The quantity $\Delta\rho$ in equation 1.23 is related to the mass of the top quark. Its dominating contribution is given by a m_t-dependent term:

$$\Delta\rho = 3\frac{G_\mu m_t^2}{8\pi^2\sqrt{2}} + \cdots. \tag{1.24}$$

The width Γ_Z^{phys} is now the *physical* width containing *all* electroweak and QCD corrections. The scaling factor ρ is defined as:

$$\rho = \frac{1}{1 - \Delta\rho}. \tag{1.25}$$

The parameter Δr, introduced in equation 1.22, is related to $\Delta\rho$ in the following way:

$$\Delta r = \Delta\alpha - \frac{\cos^2\theta_W}{\sin^2\theta_W}\Delta\rho + \Delta r_{rem}, \tag{1.26}$$

with $\Delta\alpha$ the change of the running QED coupling constant in going from zero energy to $\sqrt{s} = M_Z$, i.e.

$$\Delta\alpha = 1 - \frac{\alpha(0)}{\alpha(M_Z^2)}. \tag{1.27}$$

The first two terms in equation 1.26 are one-loop contributions; Δr_{rem} contains higher-order contributions. The contributions to Δr_{rem} are logarithmic; in particular, the contribution of the Higgs boson is given by [5]:

$$\Delta r_{rem}^{Higgs} = \frac{\sqrt{2}G_\mu M_W^2}{16\pi^2}\left[\frac{11}{3}\left(\ln\frac{M_H^2}{M_W^2} - \frac{5}{6}\right)\right] + \cdots. \tag{1.28}$$

The equations given above illustrate that weak corrections depend on the parameters M_H and m_t and on the internal structure of the electroweak theory.

1.3.2   QED Corrections

QED or "photonic" corrections can be subdivided into three classes: initial-state, final-state and initial-final state interference corrections. Both the initial and final-state corrections contain, amongst others, the brehmsstrahlung process. The initial-final state interference category contains box diagrams with an intermediate photon and a Z boson (or two intermediate photons) and product terms of initial and final-state photon radiation.

In the treatment of QED corrections, one generally distinguishes a "soft" and "hard" photonic component. The soft corrections are those with many low energetic photons (i.e. photons with an energy below a suitable cut value) in the final state; they are generally calculated using "exponentiation" techniques [11]. The hard corrections are those with one (or more) high energy photon(s) in the final state; they are incorporated using the convolution technique described below.

Since initial-state radiation changes the CM energy, it has a large influence, both on the total cross section and on the forward-backward asymmetry. To obtain sufficiently accurate predictions, they must be evaluated up to $O(\alpha^2)$. Their calculation is performed by means of a convolution of the (energy dependent) cross section with a kernel, which represents the probability that a photon of a specified energy is radiated from the initial e^+e^- system. Thus the QED corrected cross section and forward-backward asymmetry become [12]:

$$\sigma_{\rm h}(s) = \int_{z_0}^1 dz \cdot H^{(n)}(z)\sigma_{\rm h}^0(sz), \tag{1.29}$$

$$A_{\text{FB,h}}(s) = \frac{1}{\sigma_{\text{h}}(s)} \int_{z_0}^{1} dz \cdot H^{(n)}(z) \sigma_{\text{FB,h}}^{0}. \tag{1.30}$$

Here σ_{h}^{0} is the total cross section at the Born level and $\sigma_{\text{FB,h}}^{0}(s) = \sigma_{\text{F,h}}^{0}(s) - \sigma_{\text{B,h}}^{0}(s)$, i.e., the lowest order of the numerator of equation 1.15. The variable z represents the energy fraction of the $f\bar{f}$ system, remaining after a photon with energy $(1-z)s$ has been radiated off. The function $H^{(n)}(z)$ represents the kernel of the radiated photon and $z_0 = 4m_f^2/s$ a cut-off invariant mass. The order of the calculation is represented by n; in reference 12, kernels for both first and second order evaluations are given. Expressions 1.29 and 1.30 are also valid in the improved Born approximation. Calculations yield initial-state radiation corrections of the order 30% for the cross section and 3% to 15% for the asymmetry.

The final and initial-final state interference corrections are calculated to $O(\alpha)$ only, which is sufficiently accurate for present LEP-1 measurements[3]. The final-state corrections are found to be less than one percent and the initial-final state interference corrections of the order of a few percent.

To illustrate the relative effects of the different types of corrections, figures 1.5 show the results of the theoretical predictions before and after inclusion of the various corrections. Both the total hadronic cross section and the hadronic forward
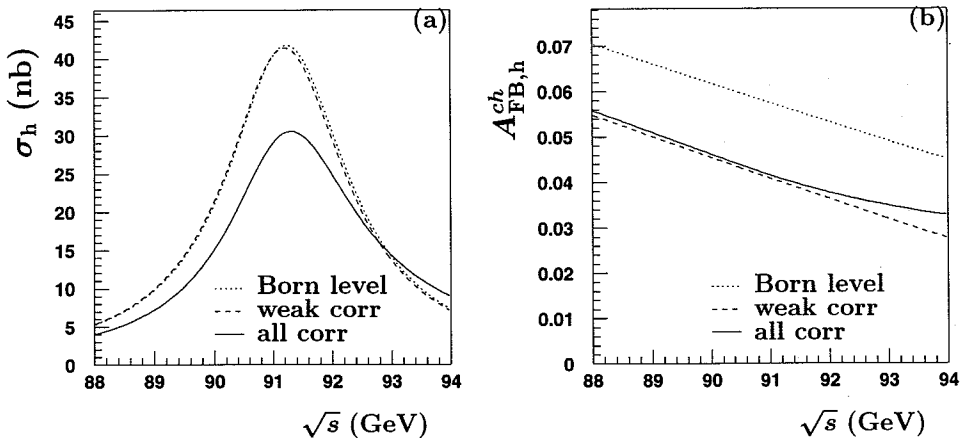
Figure 1.5: *Theoretical predictions for the $e^+e^- \rightarrow q\bar{q}$ total cross section (a) and the corresponding forward-backward charge asymmetry (b) before and after the inclusion of the various corrections.*

---

[3]Explicit formulas can be found in references 12 and 13.

backward asymmetry are calculated with a program called ZFITTER [14][4].

The left plot of figure 1.5 shows the energy dependence of the cross section at the Born level, in the improved Born approximation and after all corrections are applied. The right plot shows the energy dependence of the forward-backward asymmetry at the same three levels. The input parameters used in these calculations are $M_Z = 91.1863$ GeV, $m_{top} = 175$ GeV, $M_H = 300$ GeV, and $\alpha_s = 0.123$ [16].

The large effect on σ_h in going from the Born level to the complete set of corrections is mainly due to the initial-state QED corrections; the influence of the weak corrections (and QCD) on the line shape is very small. Note however the reversal which takes place for $A_{\rm FB}^{ch}$; now the weak corrections play the dominant role and the QED (and QCD) corrections are much smaller.

1.4   The Process $q\bar{q} \to$ hadrons

In the previous sections we discussed the decay of the exchanged γ/Z into a $q\bar{q}$ pair, as described by the electroweak Standard Model. In the real world we cannot observe quarks directly. What we detect are hadrons resulting from the original $q\bar{q}$ quarks and the subsequent gluons and quark-pairs created by them. Collectively all the quarks and gluons involved are designated as partons. Observation of the process $\gamma/Z \to q\bar{q}$ via hadrons does not imply that the configuration of the original $q\bar{q}$ pair is fully washed out. Most final-state hadrons preserve the original back-to-back geometry of the initial $q\bar{q}$, i.e. they remain grouped along the original quark direction of flight, thus forming a so-called *di-jet* structure.

The process $q\bar{q} \to$ hadrons is complex; the strong dependence of α_s on the CM energy (in particular the very large value of α_s for low energy interactions) makes exact predictions nearly impossible. Perturbative QCD is only applicable in the case of hard parton radiation; for soft parton processes, phenomenological models have to be invoked.

In the reaction $q\bar{q} \to$ final-state hadrons, one can therefore distinguish three phases:

1. Parton radiation. In this phase, the initial $q\bar{q}$ pair may radiate gluons which, in turn, may radiate additional partons; it can be described by perturbative QCD.

2. Hadronisation of the partons into hadrons. This is the phase, where perturbative QCD is no longer applicable; it is generally described by phenomenological models.

---

[4]For the calculations, ZFITTER version 4.9 is used. It should be noted that this program contains more higher order corrections than those indicated by the formulae given in section 1.3.1 and section 1.3.2, e.g. angular effects on the differential cross section due to initial state radiation (see references 10 and 15) and higher order terms in the expansions 1.24 and 1.28.

3. The decay of short-lived hadrons into detectable particles. This phase is again treated purely phenomenological, using experimentally determined input such as branching ratios, lifetimes, etc.

For the first phase, we use the so-called *parton shower model*. In this model the initial $q(\bar{q})$-quark leads to a set of final-state partons (both gluons and quarks) through a series of $q \rightarrow q+$gluon or gluon$\rightarrow q\bar{q}$ branching transitions. There is no explicit upper limit on the number of partons. Within the framework of the Parton Shower picture relevant variables are calculated using the so-called Leading Log Approximation, i.e. an approximation which takes into account all leading terms in a perturbative expansion. An alternative picture would be the *matrix element* approach, in which full calculations of the matrix elements are made up to $\mathcal{O}(\alpha_s^2)$. The disadvantage of this model is, that the number of final-state partons is at present limited to four.

For the second phase, the so-called hadronisation phase, we use the *string frag-mentation* model [17][5]. The starting point of the string fragmentation scheme is a colour-field string stretched between a q and a $\bar{q}$. The string tension grows linearly with the distance between the quarks. When the tension has become sufficiently high, the string breaks, i.e. a new $q_1\bar{q}_1$ pair is formed and two new strings are created: a $q\bar{q}_1$ string and a $q_1\bar{q}$ string. An additional $q_2\bar{q}_2$ pair can now be produced e.g. in the $q_1\bar{q}$ string, giving rise to a new $q_1\bar{q}_2$ and $q_2\bar{q}$ string, etc. The same is true for the $q\bar{q}_1$ string side. This process is continued as long as the string invariant mass remains above a certain value, depending, amongst other things, on the quark content of the string. The above description is applicable to the situation of just one $q\bar{q}$ pair after the first phase. If there are additional quark-antiquark pairs created during the parton radiation, there will be also more initial strings. If there are gluons formed during the parton radiation, the situation becomes more complicated. In the case of a $q\bar{q}g$ event, a string is stretched from the q end via the g to the $\bar{q}$ end, i.e. the gluon forms a kink on the string, carrying energy and momentum. First, the gluon splits into a $q_1\bar{q}_1$ pair, both q_1 and $\bar{q}_1$ carrying half of the gluon momentum. Then, the $qg\bar{q}$ string splits into a $q\bar{q}_1$ and a $q_1\bar{q}$ string, etc. Note, that the scheme as such does not describe baryon production. It can be incorporated by occasionally replacing the $q_1\bar{q}_1$ pair by an antidiquark-diquark pair.

In principle the relative flavour rates resulting from the string-breakups should be calculated using quantum-mechanical tools. In practice, they are fixed more or less empirically: their ratios are chosen using a mixture of ad hoc assumptions and quantum-mechanical considerations as $u\bar{u} : d\bar{d} : s\bar{s} : c\bar{c} : b\bar{b} = 1 : 1 : 0.3 : 10^{-11} : 10^{-150}$. The strong suppression of the heavy quark production is due to their large masses.

In order to describe hadronisation more quantitatively, a variable z is introduced,

---

[5]Several alternative schemes exist, e.g. the independent fragmentation or the cluster fragmentation model. In addition, there are various hybrid models combining features of the different schemes.

defined as:

$$z = \frac{E_{q\bar{q}'} + p_{L,q\bar{q}'}}{E + p_L}, \tag{1.31}$$

where $E_{q\bar{q}'}$ and $p_{L,q\bar{q}'}$ are the total energy and longitudinal momentum component of the $q\bar{q}'$-string along the direction of the q quark and E and p the energy and momentum of this "mother" quark. The probability distribution of z is given by the *fragmentation function*.

String break-up uses two types of fragmentation functions, depending on the quark flavour involved. Light quarks are assumed to hadronise according to the Lund symmetric fragmentation function, given by [18]:

$$f(z) \propto z^{-1}(1-z)^a \exp(-bm_T^2/z), \tag{1.32}$$

where $m_T^2 = m^2 + p_T^2$ is the so-called transverse mass, calculated from the q' mass m and the q' transverse momentum p_T with respect to the q quark direction. The quantities a and b are free parameters.

Heavy quarks are assumed to fragment according to the Peterson function, given by [19]:

$$f(z) \propto \frac{1}{z} \left(1 - \frac{1}{z} - \frac{\epsilon_q}{1-z} \right)^{-2}, \tag{1.33}$$

where ϵ_q is a free parameter which is expected to depend on quark mass proportional with $1/m_q^{2\,(6)}$.

The averages $< z >_c$ and $< z >_b$ of the Peterson fragmentation function are related to the fragmentation parameters ϵ_c and ϵ_b, respectively. In practice, an average $< z >$ is extremely difficult to measure; it turns out to be more convenient to replace the z-variable by x_E, defined as the ratio of the energy of the primary hadron (i.e. the first hadron created at the beginning of the fragmentation phase) to the beam energy. The averages $< x_E(c) >$ and $< x_E(b) >$ for the c and b quarks are again related to the fragmentation parameters ϵ_c and ϵ_b.

The hadronisation of partons continues until the invariant mass of all partons descends below a certain threshold energy. At that point, one has reached the third phase of the process $q\bar{q} \rightarrow$hadrons, i.e. the phase controlled by the decays of the short-lived hadrons.

A more detailed description of the above fragmentation and hadronisation processes can be found in the JETSET manual [17].

---

[6] The Peterson function was first used in framework of the the independent fragmentation scheme [17]. However, it is now also used in the Lund string fragmentation model to describe the decay of strings containing heavy flavours.

2

Data Collection and Event Reconstruction

2.1 Data Collection

LEP-1 was designed for CM energies covering the Z boson mass region; its electron and positron beams were therefore made to reach approximately 50 GeV each. The energy points at which LEP operates are a compromise between two physics needs. First, in order to get a precise measurement of the Z mass and Z width, one requires runs covering a certain region around the Z resonance. Next, one wants to make a precise study of all Z decay modes. This requires large statistics, i.e. a run at (or very near) the peak of the Z resonance only.

As a compromise between these needs, LEP performed an energy scan in the years 1991 and 1993, whereas in 1992 it ran at the Z resonance only[1]. The scan in 1991 covered seven energy points; the scan in 1993 three energy points.

For any specific reaction one observes a counting rate given by the product of $\mathcal{L}$, the *instantaneous* luminosity and the cross section of the reaction. Thus the total number of Z decays at any specific energy is proportional to the *time-integrated* luminosity at that energy. This instantaneous luminosity is defined by:

$$\mathcal{L} = \frac{N_{e^+} N_{e^-} n_b f_{rev}}{4\pi \sigma_x^* \sigma_y^*}, \tag{2.1}$$

where N_{e^+} and N_{e^-} are the number of positrons and electrons in the colliding bunches, n_b the number of bunches, f_{rev} the revolution frequency of the bunches and σ_x^* and σ_y^* the RMS spread of the beam in the x and y direction, respectively. This formula implies a measurement of the beam parameters, which is very difficult. The common way to measure the luminosity is to use the theoretically well-known (very) forward Bhabha process $e^+ e^- \rightarrow e^+ e^-(\gamma)$ as a reference reaction [20].

---

[1] The 1992 decision was also influenced by other reasons mentioned later.

The performance of LEP is expressed in terms of the time integrated luminosity. For LEP experiments, the usual unit for the integrated $\mathcal{L}$ is the inverse picobarn (pb^{-1}), i.e. the amount of events collected per pb of cross section. LEP became operational in 1989. Up to 1992 LEP ran in the so-called four-bunch mode, i.e. with four electron and four positron bunches. In 1992 and 1993, it ran both in the 4-bunch mode and in the 8-bunch mode. Over the years, the time-integrated luminosity (and thus the number of observed Z decays) has steadily increased. Specifically for L3, the recorded time-integrated luminosities were $0.6pb^{-1}$, $6pb^{-1}$, $13pb^{-1}$, $23pb^{-1}$ and $33pb^{-1}$ in 1989, 1990, 1991, 1992 and 1993, respectively. The luminosity measurements are described in great detail in references 6 and 20.

Because the precision of the Z-mass and its width depend on the exact beam energy at which the data are taken, it is important to have an accurate energy calibration of LEP. Extensive studies were done to obtain precise beam energy measurements [21, 22, 23, 24]. At present, the calibration technique yielding the most precise result is the resonant depolarisation method. This method requires that the beam has a significant amount of polarisation to begin with; this in turn depends in a rather involved way on the beam tuning parameters. In 1991, the depolarisation method was used for the first time at a beam energy of 46.5 GeV. In 1992, however, one could not obtain polarised beams. In this situation, an energy scan would not have significantly improved the errors on the Z-mass and Z-width and it was decided to run at the resonance only. In June 1993, both the resonance and two off-peak energies were successfully calibrated with the resonant depolarisation method, resulting in very small errors on the beam energies[2].

Full listings of the 1992-1993 CM energies and the calibration errors on the CM energies are given in table 2.1. The listed 1992 errors is obtained from reference 22; the 1993 errors are obtained from references 23 and 24. The year 1993 is split into two periods: the period before the energy calibration (indicated as "Pre") and the period after the energy calibration ("Scan"). Data on off-peak energies were always taken during "Scan" periods. For the scan period, the symbol "P" means a CM energy on the peak and "P±2" a CM energy shifted away from the peak by approximately plus or minus 2 GeV, respectively.

2.2   The L3 Detector

The L3 experiment was designed to study e^+e^- collisions in the 100-200 GeV range [25]. It consists of series of concentric subdetectors, embedded in a large 0.5 T magnet. The subdetectors measure the easiest to stop particles close to the interac-

---

[2]Illustrating the precision of this technique, is the dependence found of the beam energy on deformations of the LEP ring caused by the moon tides and, more recently, the discovery of small (but detectable) systematic drifts of the LEP-ring dipole magnets due to ground leak-currents in the Geneva-area caused by the arrival and departure of TGV trains.

period	E_{CM}(GeV)	ΔE_{CM} (GeV)
1992	91.294	0.018
1993 Pre	91.319	0.018
1993 Scan, P−2	89.452	0.0029
1993 Scan, P	91.211	0.0063
1993 Scan, P+2	93.034	0.0031

Table 2.1: *CM-energies and their errors resulting from the calibration. See the text for the definition of Pre, Scan and P(±2).*

tion vertex, the most penetrating ones in the outer-most subdetector. A schematic view and the coordinate system used are shown in figure 2.1. Starting from the interaction point and going outwards, one meets the following the subdetectors (see figure 2.1):
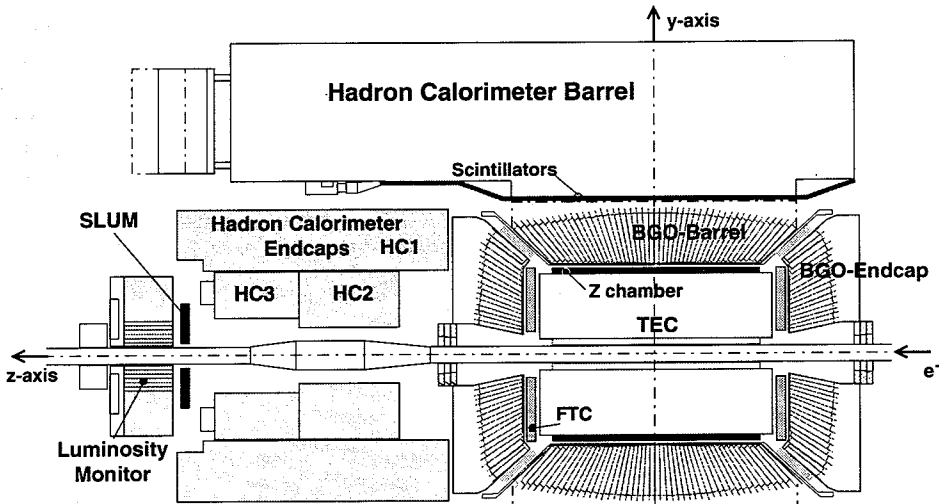
Figure 2.1: *Location of the various subdetectors in L3. Not shown are the Muon Chambers, surrounding the hadron calorimeter barrel.*

- The Central Tracking Detector, designed to measure tracks caused by charged particles. It consists of the Time Expansion Chamber (TEC), surrounded by Z-chambers in the barrel region and the Forward Tracking Chamber (FTC)

in the endcap regions. The Z-chambers consist of a double layer of cylindri-
cal proportional wire chambers with cathode strip readout; the FTC of two
cylindrical multi-wire drift chambers. Given the importance of the TEC for
our analysis, a more detailed description is given in section 2.2.1

- The Electromagnetic Calorimeter (ECAL), designed to measure the energies of
  electromagnetically interacting particles. It is an assembly of BGO (Bismuth
  Germanium Oxyde) crystals, and consists of three parts: the BGO barrel
  covering the polar range $42° < \theta < 138°$, and two endcaps covering the polar
  ranges $11.6° < \theta < 38°$ and $142° < \theta < 168.4°$. The barrel contains 7680
  crystals, mounted in 48 rings of 160 crystals; each of the two endcaps comprises
  1527 crystals arranged in 16 sectors, fifteen of which having 96 and one 87
  crystals. The ECAL thickness corresponds to 21.4 radiation lengths [25].

  Test runs were performed to calibrate the ECAL [25]. Subsequently, the re-
  sults were improved by using Bhabha events and (low energy) TEC-measured
  electrons. With these improvements one obtains an analytical formula for the
  ECAL-energy precision [26]:

  $$\frac{\sigma(E)}{E} = \sqrt{\left(\frac{1.54}{\sqrt{E}} + 0.38\right)^2 + (1.18)^2 + \left(\frac{0.25}{E}\right)^2} \% \,, \qquad (2.2)$$

  with E expressed in GeV. At 45 GeV, the energy precision is about 1.3% .

- The Hadronic Calorimeter (HCAL), designed to measure the energies of had-
  rons. It consists of four parts: a barrel calorimeter, two endcaps and a muon
  filter around the barrel. The HCAL is made of uranium layers interspersed
  with layers of gas-filled proportional wire chambers. The uranium acts as
  absorber material for the hadrons; of the charged particles in essence only
  muons are able to get through. On average its thickness corresponds to 3.5
  nuclear interaction lengths [25] [3]. Also the HCAL required extensive energy
  calibration test runs. After calibration, an energy precision is found, given
  by [27]:

  $$\sigma(E)/E = (55/\sqrt{E} + 5)\% \,, \qquad (2.3)$$

  with E again expressed in GeV.

- The Muon Chambers (MUCH), designed to measure the momentum of muons.
  It consists of large drift chambers, mounted octagonally on two so-called Ferris
  wheels. Each octant has three P-chambers, measuring the $r\phi$-plane parameters
  of the tracks. On the top and bottom of the inner and outer layer, Z-chambers

---

[3]Note that the ECAL, the muon filter and the support tube effectively add respectively 0.9, 1.0
and 0.5 interaction lengths to this number.

are installed to measure the $r\theta$-plane parameters. For muons traversing the three MUCH layers the momentum precision is 2.5% at 45 GeV; when the momentum is determined using only two layers, this precision worsens to around to 20% [28].

- The luminosity monitor (LUMI), designed to measure the luminosity for each LEP fill at the location of the L3 detector. It consists of two disks placed at $z = \pm 2.8$m, both, like the ECAL, made of BGO crystals (304 in total). The polar range covered is 24.7 mrad $< \theta < 69.3$ mrad and $\pi - 69.3$ mrad $< \theta < \pi - 24.7$ mrad, respectively. Used stand alone, the LUMI reaches a luminosity precision of approximately 6‰ [6].

  In 1993, two additional silicon detectors (SLUM) were installed in front of the LUMI calorimeters. Each one contains 4096 silicon strips mounted in three layers: an R-measuring layer (at $z = \pm 2.61$ m), a ϕ-measuring layer (at $z = \pm 2.65$ m), and another R-measuring layer (at $z = \pm 2.69$ m); these layers cover a 2π azimuthal angle between radii of 76 and 154 mm. The use of the SLUM diminished the systematic error of the luminosity measurement from 6‰ to 1.5‰ [29].

- Scintillation Counters, primarily designed to distinguish cosmic muons from muons originating from Z-decays. At present their timing signals are also used to trigger on e^+e^- interactions. They are mounted on the inner side of the HCAL barrel and consist of 30 plastic scintillation counters. The trigger system will, given its importance, be treated in more detail in section 2.2.2.

Particles passing the different subdetectors deposit part – or in some cases the whole – of their energy in these components. These energy depositions, further to be the called *hits*, lead to the specific subdetector-signals. How these hits and signals are subsequently handled to obtain tracks, bumps, etc. up to completely reconstructed events, forms the subject of section 2.3.

2.2.1 The Time Expansion Chamber

The TEC is the heart of the central tracking detector. It was designed for the purpose of measuring the curvature and the direction of charged particles. It can thus be used to determine the charged multiplicity of the event and to reconstruct the primary e^+e^- interaction point and possibly secondary vertices. It consists of two concentric cylindrical drift chambers with common end plates and a common gas volume. The inner radius is 8.5 cm, the outer 46.9 cm. All wires are grouped parallel to the beam direction. Their sensitive length is 98.2 cm. The TEC is filled with 80% CO_2 and 20% iC_4H_{10}, at a temperature of 291 K and pressure of 1.2 bar. This allows for low drift speeds of the electrons produced by the tracks, and hence for more accurate measurements of the track parameters.
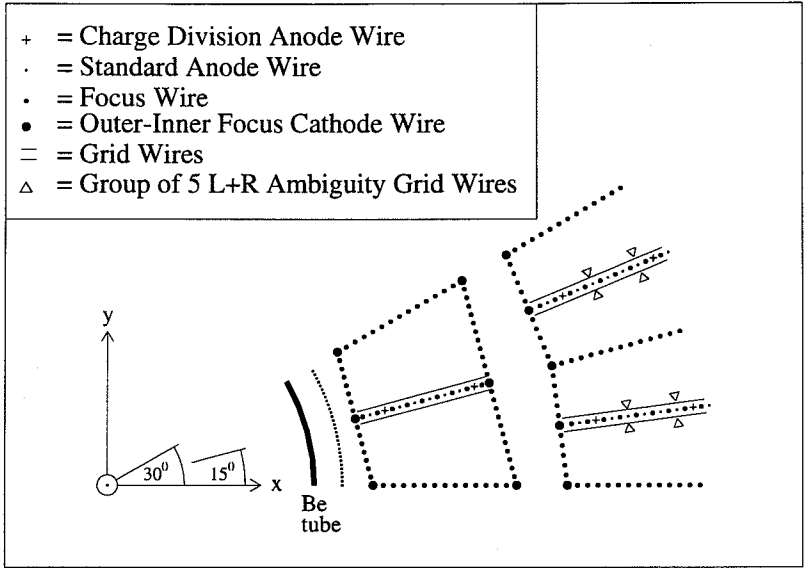
Figure 2.2: *Geometry of the TEC wires.*

The TEC contains several wire planes, effectively dividing it into 12 inner and 24 outer ϕ-sectors. The boundaries of those sectors are the cathode wire planes. In the middle of the sectors are the anode wire planes. The high field amplification region at the anode-sense wire planes is separated from the low field drift region by additional drift wire planes; these grid wires make the field in the low field drift region homogeneous.

Two kinds of anode wires are distinguished: standard wires to measure the $r\phi$-plane coordinates of the track, and charge division (CD) wires to determine the θ-coordinate. Fixed groupings consisting of 5 grid wires are used, in order to resolve the inherent wire chamber left-right (LR) ambiguities. The inner sectors consist of 6 standard wires and 2 CD wires. The outer sectors consist of 31 standard wires, 9 CD wires and 14 LR wire groups. The grouping of all these wires in the TEC is shown in figure 2.2.

The drift time is determined by a center of gravity method. The anode pulses are sampled by Flash Analog to Digital Converters (FADCs). As the amount of data collected by the TEC is very large (about 2 Mb/event), data reduction processors are installed to diminish the amount of data to be stored; a reduction by approximately a factor 20 is obtained.

Also the TEC is an L3 subdetector which requires extensive calibrations. With

these calibrations a wire precision is obtained of approximately 60 μm [30]. This results in a relative transverse momentum precision of $\sigma(p_T)/p_T \approx 0.02 \cdot p_T$, with p_T measured in GeV. These numbers apply only to the regions, where the electric field is homogeneous. Near the cathode and the anode there are inhomogeneities which make the TEC calibration more difficult and the precision correspondingly worse. These deficiencies will play an important role in our discussion about the detector simulation in chapter 3 and the forward-backward hadron selection in chapter 4.

2.2.2 The L3 Trigger System

In order to reduce detector "dead time" and to avoid too large an amount of tape writing, L3 needs an efficient trigger system. The data in each subdetector are digitised and sent to the trigger system. The L3 trigger system consists of 3 levels of which level 1 decides, if the detector has to be reset to receive data from the next bunch crossing ~ 22 μs later in the (4×4) bunch mode, 11 μs in the (8×8) bunch mode – or if the data have to be analysed by the level 2. If the outcome of the highest level (level 3) is positive, the data are written onto tape.

The level 1 trigger needs fast decision logic, because it has to be ready before the next bunch crossing. It is a logical OR of the signals from the following detector-triggers:

- The energy trigger (coming from the ECAL, HCAL and LUMI); this trigger consists of different subtriggers, which checks quantities such as the total energy and the number of hits. There is also a total energy subtrigger, obtained from the sum of the trigger signals of the two calorimeters. A detailed description of this trigger is given in reference 6.

- The muon trigger; also the muon trigger consists of different subtriggers. Track searches are performed by looking for coincidences between muon chamber P- and Z-layers.

- The TEC trigger; this trigger works in a way analogous to the muon trigger. All the fired LR wires in the outer TEC chamber are read out. Each half sector is divided into two ϕ-regions. In each sector, a quick track search is performed by grouping the hit-patterns obtained from the LR-wires.

- The scintillation trigger. This trigger consists of a multiplicity trigger and a coincidence pattern trigger. The first trigger imposes a requirement on the number of pairs of hits; the second one requires that at least two of the hits be separated more than 90° in azimuth.

With the threshold settings used in the standard L3 running and under normal beam and detector conditions, the level 1 triggers at a rate of approximately 8 to 12 Hz.

After each positive level 1 decision, the level 2 trigger is called upon. Level 2 rejects background using the complete level 1 trigger information. First, it checks if the event numbers of the subdetectors coincide. If not, the data are considered not synchronised. Then, the energy distribution of the event is analysed, together with the track information provided by the TEC charge division wires; this CD wire information is now fully usable, because the available time is sufficient compared to the drift times involved. The rate of level 2 positive decisions is about 6 to 10 Hz. However, one out of ten events rejected by level 2 are sent to level 3 anyhow – this in order to allow for level 2 efficiency and background studies.

The level 3 trigger inspects all results from the level 1 and level 2 trigger and the fully digitised data. Up to this point, the latter information could not be used because the data reduction processors from the TEC require 20 ms to fulfill their task. The level 3 trigger again reduces the amount of data, now by approximately a factor of 3. When the decision of level 3 is positive, the data are written onto tape; thus the resulting tape-writing rate is approximately 2 to 3 Hz.

Because the conditions of the detector are time-dependent, the status of the detector is continuously monitored during data-taking; in addition special status-information is collected and written into a data-base at the start of each new run.

2.3   Event Reconstruction

The events written onto tape can be used in a variety of analyses. In order to calculate the relevant event features, a general reconstruction program (REL3) has been written. This program reads the data from tape and reconstructs event properties, such as the visible energy and the number of tracks.

Before the reconstruction of events, the data-base is read out, in order to obtain the necessary information about the detector status, i.e., amongst others, the high voltage status of the TEC sectors, the status of the TEC-wires and the TEC-calibration constants, the status of the ECAL crystals and their ADC-gains, the high voltage status of the HCAL modules and their wire ADC-gains, etc.

The reconstruction of the event takes place in 3 steps. In a first step, all hits are grouped into subdetector primitive objects such as a bump in the ECAL or a track in the TEC. In a second step, the primitive objects themselves are correlated to find the event's particles. In a third step, these particles are used to derive event properties.

Different types of tape formats are used to store relevant data, depending on the nature of the analyses involved. The most basic format is the one leading to the so-called Data AcQuisition (DAQ) tapes. DAQ tapes are written during data taking and contain all the subdetector signals. The Data REconstruction (DRE) tapes again contain the subdetector signals and all the information obtained after the first, second and third reconstruction steps. The tape format used in the present

analysis is the Data SUmmary (DSU) tape. DSUs are derived from DRE tapes: they omit the subdetector signals from the DAQ/DRE tapes, and contain only a fraction of the reconstruction information stored on the DREs. Running over DSU-tapes goes faster than running over DAQ tapes (by a factor of approximately 4) and requires less storage space than for DRE-tapes (by a factor of approximately 7).

2.3.1 Reconstruction of Primitive Objects

TEC objects reconstruction

The TEC reconstruction software is one of the more complicated subprograms of REL3, as the hits have to be treated three-dimensionally. Because the z-information of the hits is very poor, tracks are reconstructed in two steps: the first step attempts to reconstruct the $r\phi$-plane track projections; the second step aims at reconstructing three dimensional tracks.

Specifically, the first step consists of combining hits, fitting circles, splitting groups of hits and refitting circles, until all circle fits show no further improvement and ambiguities are resolved. In the beginning, only hits lying more or less on a radial line are combined; later on, only hits nearby a fitted circle. Kinks are detected by comparing the χ^2 of fits on either side of a presumed kink position. Ambiguities arise when there is no LR information; most of these can be resolved using the hits in the inner TEC. The first step thus leads to the following $r\phi$-plane track parameters: a Distance of Closest Approach (DCA) with respect to the fill vertex, the ϕ at the intersection with the xy-plane and the curvature κ.

In the second step, the θ-coordinate of each track is calculated. For each track, the polar angle is obtained from a straight line fit in the sz-plane to all CD wire hits and to the Z-chamber hits, whenever present.

All tracks thus found constitute the primitive objects in the TEC, the so-called "TTRKs". A more detailed description of the TEC reconstruction is given in reference 30.

ECAL objects reconstruction

The primitive objects in the ECAL are bumps and called "EBMPs". A bump is an energy deposition, which, in principle, corresponds to one particle. Bump reconstruction in the ECAL is relatively easy since the coordinates of the crystals are directly given in terms of the θ and ϕ parameters. Primarily, the procedure consists of grouping adjacent crystals into clusters. The crystal energies are calculated from the ADC contents and the calibration constants stored in the data-base. The energy deposited in each crystal has to be at least 10 MeV, and a cluster has to have at least 40 MeV. In principle, every cluster corresponds to a single bump, but often a cluster has to be split, because of the possibility of two or more particles being so close as to form one single (and possibly deformed) cluster. The number of bumps,

into which each cluster is separated, thus equals the number of local maxima in the cluster. Bumps caused by electronics noise and identified by their rectangular shape and homogeneous crystal-energy distribution, are excluded from the list of ECAL primitive objects at the event reconstruction level.

HCAL objects reconstruction

The HCAL reconstruction is again complex, since, like in the TEC, the hits are deposited three dimensionally and separate reconstructions in the barrel, endcap and muon filter are required. In order to reject the noise resulting from the natural radioactivity of uranium, all hits with an energy smaller than 4 MeV are excluded from the reconstruction.

The reconstruction in the barrel starts with a search for pre-clusters in each of the 144 modules. If pre-clusters in neighbouring modules are sufficiently close, they are merged together into a new single cluster. In this way, more or less spherical clusters are reconstructed. After this a second algorithm is called upon, identifying minimum ionising particles (muons) traversing the HCAL barrel.

In the HCAL endcaps, the procedure is different, as the endcaps are differently segmented. Clusters are now found by repeatedly searching hits carrying more than a specific minimum energy and grouping them with neighbouring hits. No search for minimum ionising particles is performed.

In the muon filter, the particle multiplicity is low. In addition, given the thinness of this filter, the energy depositions lie on a nearly straight line. As a consequence, the muon filter reconstruction consists of relatively simple straight line fits.

The clusters and tracks thus found in the barrel, endcap and muon filter constitute the primitive objects in the hadron calorimeter.

MUCH objects Reconstruction

The muon chamber reconstruction is again relatively simple as the Z-event muon track multiplicity is low and the energy depositions lie – to a good approximation – on a helix. The muon tracks observed are mainly coming from dimuon events, tau-decays, B-decays and cosmics. One starts from the hit signals in the P- and Z-chambers, and groups them into segments. In each octant, the segments found in the Z-chambers are matched with the segments in the P-chambers. In this way, three dimensional information is obtained. The muon tracks thus found are the primitive objects in the MUCH. A more detailed description of the muon chamber reconstruction is given in reference 28.

2.3.2   Reconstruction of Particles

After the reconstruction of primitive objects in the subdetectors, the "Across REL3" (AXL3) reconstruction combines these objects into "particles" on the detector level.

Three types of reconstructed entities are distinguished:

- an ASRC (Across L3 cluster): a primitive object from the ECAL and/or the HCAL, either associated with (a) TEC-track(s) or stand-alone;

- an ATRK (Across L3 track): a TEC track, matched with a calorimeter object;

- an AMUI (Across L3 muon track): a track in the muon chambers associated with minimum ionising ECAL or HCAL objects.

The ASRC search is initiated by locating the ECAL and HCAL primitive objects and subsequently trying to correlate them. In this procedure, one distinguishes "front" and "deep" calorimetric objects. In essence, all bumps in the ECAL are front objects. Most HCAL-clusters are deep objects; exceptions are HCAL-objects in the first few layers of the HCAL covering the gap between the ECAL-barrel and the ECAL-endcaps. The deep objects are all HCAL clusters deposited behind a front object. Thus, in essence each ECAL and HCAL correlation consists of a matching of a front and a deep object.

The ATRKs are found by matching the primitive objects in the TEC with the closest front object in the ECAL or, exceptionally, in the HCAL. The search for the closest object is performed using the track θ-information if available; if not, the closest object in ϕ is taken. Subsequently, TEC-tracks are matched to ASRCs. An ASRC may correspond to more than one particle, e.g. if there is more than one associated TEC track; each ATRK however always corresponds to a single charged particle.

After matching a TEC track with a front calorimeter object, the θ of the track is refitted by considering the front object as an extra hit of the track. If the original TEC track does not have a θ-determination, this leads to a substantial matching improvement. Further improvements are obtained by searching for nearby Z-chamber or FTC hits and performing a second refit of the track parameters.

The AMUI reconstruction will not be further discussed here.

ASRC Energy Determination

In principle, after the calibrations, the ASRC energy, defined as the sum of the energies of the corresponding primitive calorimetric objects, should correspond to the real particle energy. In reality it does not, because there are detector gaps and inefficiencies as well as shower fluctuations. Thus, further corrections are needed. They are implemented by the introduction of the so-called G-factors. For the geometry dependence of the G-factors we distinguish nine different regions (see below). As the energy loss mechanisms involved are different for electromagnetically interacting particles (photons and electrons) and hadronically interacting particles, two sets of G-factors are considered: an electromagnetic set and an hadronic set. One also distinguishes data G-factors and Monte Carlo ones. For the data, they are

determined by minimising the difference between the visible energy and the CM energy. For the Monte Carlo, they are found by comparing the average Monte Carlo energy depositions with those of the data. In both cases electromagnetic G-factors are determined by using Bhabha events and hadronic G-factors by employing di-jet hadron events [31].

The corrected particle energy is then given by:

$$E_{\text{ASRC}} = \sum_i G_i^c E_i, \tag{2.4}$$

where E_i is the primitive object energy in detector region i and G_i^c the corresponding G-factor. The superindex c indicates the type of the ASRC: electromagnetic or hadronic. Note that the definition does not include the momenta of the TEC-tracks belonging to the ASRC. One distinguishes nine G-factor regions; they are defined as shown in figure 2.3.
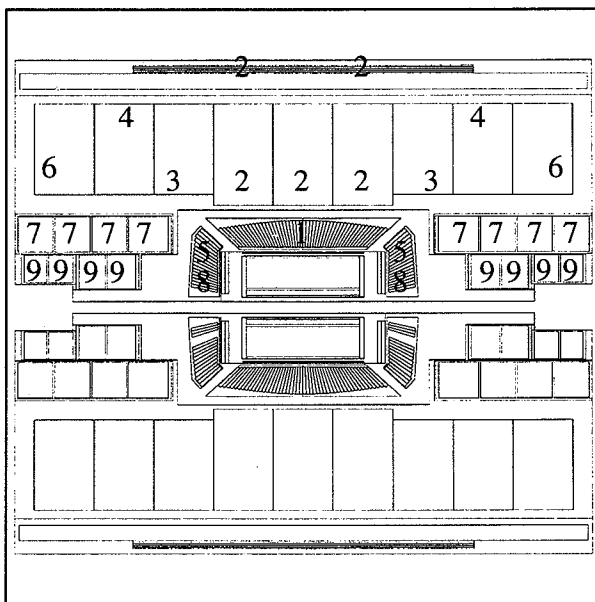
Figure 2.3: *The nine detector subregions distinguished in the particle energy determination.*

Obviously, the proper determination of the energy of an ASRC depends on its correct identification as being either electromagnetic or hadronic. This decision is made on the basis of the following quantities:

- The probability p_E that the cluster is of electromagnetic origin using ECAL information only. A ratio E_9/E_{25} is calculated, i.e. the total energy of the 9 crystals in a (3×3) array centered around the most energetic crystal, divided by the total energy of the 25 crystals in a (5×5) array around this same crystal. Comparing E_9/E_{25} with a reference distribution, obtained from test-beam data, a χ^2 is calculated as:

$$\chi^2_E = \frac{(E_9/E_{25} - r_{test})^2}{\sigma^2_{test}}, \tag{2.5}$$

where r_{test} is the average of the test-beam distribution and σ_{test} the corresponding width. The probability is then given by $p_E = P(\chi^2_E, 1)$, where $P(\chi^2, n)$ is a χ^2-probability distribution for n degrees of freedom.

- The probability p_{TE} that the cluster is electromagnetic using both TEC and ECAL information. Now the crystal energy sum E_9 is compared with the TEC momentum p. A ratio E_9/p is calculated and a χ^2 evaluated:

$$\chi^2_{TE} = \frac{(E_9/p - 1)^2}{\delta^2(E_9/p)}, \tag{2.6}$$

where $\delta(E_9/p)$ is the error on the E_9/p measurement. This χ^2_{TE} leads to the probability $p_{TE} = P(\chi^2_{TE}, 1)$.

- The probability p_{TH} that the cluster is electromagnetic using both TEC and HCAL information. This probability is derived in the same way as for p_{TE}, but with E_9 replaced by E_{HCAL} (Note that for this calculation, the HCAL energy is provisionally calibrated with the electromagnetic G-factors).

- The probability p_{TEH} that the cluster is electromagnetic using TEC and the *joint* ECAL and HCAL information. Analogous as for p_{TH}, but using as the energy the sum of the ECAL and HCAL energies (Also here, the total calorimetric energy is provisionally electromagnetically calibrated).

- The ratio r_H of the total front HCAL energy to the total HCAL energy.

- The ratio r_{EH} of the total front calorimetric (ECAL+HCAL) energy to the total calorimetric energy.

The probabilities p_E, p_{TE}, p_{TH} and p_{TEH} are combined into one joint electromagnetic probability. An extra weight is given to the ECAL-only probability, by considering the quantity

$$p_{TOT} = P[(\chi^2_E + \chi^2_{TX}), 2], \tag{2.7}$$

and using χ^2_{TX} for the χ^2 corresponding to the maximum of the probabilities p_{TE}, p_{TH} and p_{TEH}.

The final algorithm used to decide on the fact whether the ASRC considered is electromagnetic or not is to ask that at least one of the following conditions be satisfied:

- $p_{TOT} > 0.001$;

- $r_{EH} > 0.95$;

- $r_H > 0.95$.

Distributions of p_{TOT}, r_H and r_{EH} are shown in figure 2.4[4]. Note that all the plot ordinates given are of the type (number of events)/(abscissa bin width). Unless specified otherwise, this convention will be used in all further plots in which the ordinate represents a number of hits, tracks, events, etc.

2.3.3   Reconstruction of Jets

The aim of the jet reconstruction is to identify all jets in an event (see section 1.4) and to measure their direction and energy. The procedure starts from the calorimetric "particles", i.e. the ASRCs. It consists of subjecting these ASRCs to a so-called "jet algorithm". Also included in this procedure are the AMUIs; they are temporarily treated as the equivalent of an ASRC. The ATRKs are not included in order to avoid a double counting of the charged particles[5].

Over the years, many jet reconstruction algorithms have been developed, ranging from relatively simple to very complex algorithms. The algorithm used in the present analysis is an example of a very simple one: the Simple JeT (SJT) algorithm. It only distinguishes "high energetic" and "low energetic" jets.

High energetic jets are identified as follows: in a first step, the ASRC with the maximum energy is localised and all ASRCs which are within a 30° cone around its direction, assigned to it; a jet-axis is calculated using the energy-vectors of the ASRCs belonging to the jet. In subsequent steps, the same procedure is repeated, but now only using the ASRCs *remaining* after the previous step. This procedure is stopped when none of the remaining ASRCs has an energy larger than 7 GeV. In a third and final step, all remaining ASRCs lying within a 20° cone around an ASRC already assigned to a jet, are added to the jet containing that ASRC.

In order to find low energetic jets, the high-energy-procedure as described above is repeated on all the remaining ASRCs, but with different cut values. The cut on

---

[4]Note that for this figure and also for the figures in chapter 3, we use data samples the selection of which is discussed in chapter 4.

[5]The effect of double counting the minimum ionising energy depositions of the AMUIs in the calorimeters is negligible.
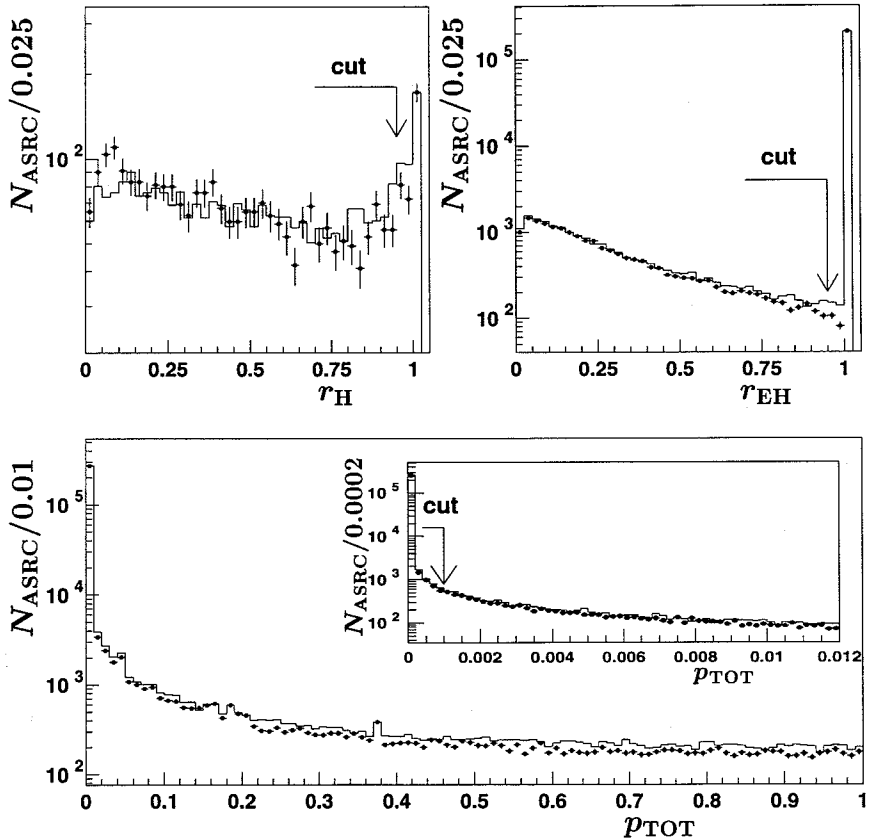
Figure 2.4: *Distributions of the variables r_H, r_{EH} and p_{TOT} used for the identification of electromagnetic ASRCs. The dots correspond to the data (see chapter 4); the histograms to the Monte Carlo predictions. The Monte Carlo histograms are normalised to the number of ASRCs in the data. In order to better visualise the position of the p_{TOT}-cut, a blow-up of the low p_{TOT}-region is inserted.*

the ASRC energy-maximum is loosened to 2 GeV and the initial 30° cone reduced to a 20° one.

If, after the high and low energy jet search, there remain ASRCs which are not assigned to any jet, they are stored separately for further calculations as *free* ASRCs.

In principle, the jet energy is the sum of the energies of all particles in the jet. (For muons, we use the energy as given by the AMUI reconstruction.)

2.3.4 Definition of Global Quantities

A certain number of global event-quantities are of direct relevance for our analysis. The first quantity is E_{vis}, the total visible energy. It is defined as:

$$E_{vis} = \sum_{jets} E_{jet} + \sum_{free} E_{ASRC}^{free}, \qquad (2.8)$$

with E_{jet} the jet energy and the second sum is over all free ASRCs. An equally important quantity is the vectorial ASRC energy sum, defined as:

$$\vec{E} = \sum_{ASRCs} E_{ASRC} \cdot \hat{n}_{ASRC} + \sum_{AMUIs} \vec{p}_{AMUI}, \qquad (2.9)$$

where $\hat{n}_{ASRC}$ is the direction of the ASRC as seen from the interaction point and $\vec{p}_{AMUI}$ the AMUI momentum. Quantities derived from $\vec{E}$ are the perpendicular and longitudinal energy imbalances, i.e.[6]:

$$E_{\perp} = \frac{\sqrt{E_x^2 + E_y^2}}{|\vec{E}|}. \qquad (2.10)$$

$$E_{\parallel} = \frac{|E_z|}{|\vec{E}|}, \qquad (2.11)$$

The event thrust and event thrust axis are derived from the expression:

$$T = \max_{\hat{n}_T} \frac{\sum_{jets} E_{jet} \cdot |\hat{n}_{jet} \cdot \hat{n}_T| + \sum_{free} E_{ASRC} \cdot |\hat{n}_{ASRC} \cdot \hat{n}_T|}{\sum_{jets} E_{jet} + \sum_{free} E_{ASRC}}, \qquad (2.12)$$

where T is the thrust and $\hat{n}_T$ the axis which maximises this expression. Conventionally, this axis is assigned the direction of the maximum energy flow.

Finally, the sphericity tensor is defined:

$$S^{ij} = \frac{\sum_{ASRC} E_{ASRC}^2 \cdot \hat{n}_{ASRC}^i \cdot \hat{n}_{ASRC}^j}{\sum_{ASRC} E_{ASRC}^2}, \qquad (2.13)$$

where $i, j = x, y, z$ denote the components of the unit vector $\hat{n}_{ASRC}$. By diagonalising one finds the eigenvalues $\lambda_1 > \lambda_2 > \lambda_3$. The sphericity variable S is then given by:

$$S = \frac{3}{2}(\lambda_2 + \lambda_3), \qquad (2.14)$$

where the factor $\frac{3}{2}$ is introduced to obtain $0 < S < 1$.

---

[6] When there are low energetic electromagnetic particles in the jet, their contribution to the jet energy is calculated with hadronic G-factors instead of electromagnetic ones. This – in principle (slightly) incorrect procedure – is necessary to compensate for the equally (slightly) incorrect procedure followed during the calibration test runs. Note that this is also the reason why equation 2.9 is used to calculate the energy imbalances instead of the strict vectorial analogue of 2.8.

3

Detector Simulation

A standard way to study the efficiency and purity of the collected data is to compare them with Monte Carlo (MC) simulated data. The simulation of events is performed in two stages: the first one is the event generation and describes – in our case – the reactions $e^+e^- \to \gamma/Z \to q\bar{q} \to$ final state particles. The second stage simulates the way the final state particles pass through the various subdetectors, i.e. how they deposit their energy and cause the detector signals.

In order to make precision measurements, these stages have to be correctly simulated. The first one relies on the theoretical models given in chapter 1; the second relies both on the modelling of the interactions of the particles with the detector materials and on the quality of the monitoring of the subdetector conditions.

When the detector components are 100% efficient, the detector is called "ideal", and the second stage produces the "ideal" detector simulation. In reality, however, the detector is never ideal. When the facts related to this reality are taken into account, the second stage leads to a "real" detector simulation.

Before going into detail in the real simulation of the most important detectors for our analysis (the TEC and the calorimeters), a short summary of the event generation and the ideal detector simulation is given.

3.1 Event Generation – Ideal Detector Simulation

The primary event generation consists of the simulation of the process $e^+e^- \to Z/\gamma \to q\bar{q} \to$ final state particles. For background purposes one also has to simulate the reactions of e^+e^- into other final states. The program used for the simulation of the main process is JETSET 7.3, a description of which is given in reference 17. The programs needed to simulate the background event types will be mentioned in chapter 4. The specific software packages used for the detector simulation are GEANT3 [32] and SIL3 (SImulation of L3). The first package is very general and

can be used to simulate the interaction of any particle with any detector material; the second package is L3 specific.

Simulation of the detector is a very detailed process; on an HP 9000/715 it takes about one minute of computing time per event. Input for this simulation are the detector geometry, material properties, particle lifetimes, cross sections of the particles with the nuclei in the detector material, multiple scattering estimates, etc. Primary output of the simulation are – amongst other things – the TEC hits and the ECAL- and HCAL-energy depositions. In the simulation of the momenta in the TEC, the most important input quantities are gas properties and multiple scattering parameters. Likewise, for the simulation of the ECAL and HCAL shower energies and dimensions, the most important inputs are the BGO and uranium conversion c.q. interaction lengths. Simulation not only takes into account backscattering processes from TEC or ECAL edges into the TEC, but also backscattering from the HCAL into the ECAL. At the "ideal" detector level, the only noise which is simulated is the one due to uranium decay. The energy spectrum used is derived from test runs [33].

When events have passed the second simulation stage, they are written onto tape in the same format as for the real data, so that their properties can be reconstructed with the same program as the one used for data reconstruction (see chapter 2).

3.2 Real Detector Simulation

Starting point of the real detector simulation is to evenly distribute the Monte Carlo events over the runs belonging to the periods which have to be simulated. This is achieved by means of the time-integrated luminosity of the runs: the number of Monte Carlo events assigned to each run is chosen proportional to the luminosity of that run.

For each subdetector, real detector simulation primarily acts on the hit level. The event is reconstructed after modifying c.q. rejecting the hits per run, according to the detector status information stored in the data-base. Sometimes additional (a-posteriori) operations on either the track or the event level are required (such as smearing, noise adding) in order to make the Monte Carlo simulation fully agree with the data.

In the following subsections, we will first treat ECAL simulation, which is important both for cross section and forward-backward asymmetry measurements. Next, the TEC simulation is presented, which only affects the asymmetry measurements. Note that in principle also the HCAL requires a real detector simulation. However, at the present level of our statistics, its effect on the cross section (and forward-backward asymmetry) measurement turns out to be negligible. The discussion of the HCAL real detector correction is therefore omitted.

3.2.1 ECAL Simulation

The task of the real ECAL calorimeter simulation is to account for the deficiencies in the ECAL. These are mainly inactive or noisy crystals and inefficient electronics. For each run, this information is read from the L3 data-base and taken into account for the event reconstruction.

Figure 3.1 above shows the activity of the ECAL crystals for a typical running period, at the positive z side of the ECAL. The crystals are shaded according to their activity; the light ones are the most active and the darkened ones the least
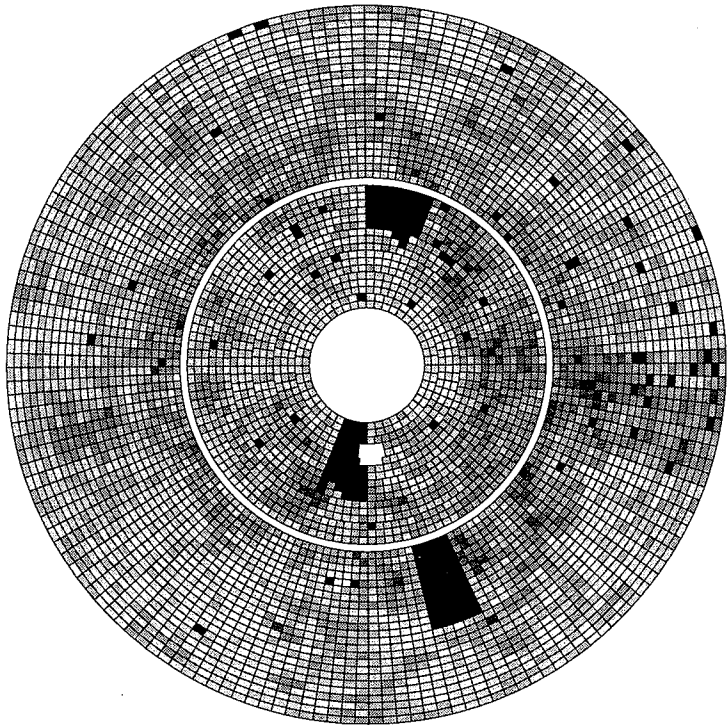
Figure 3.1: *The activity of the crystals on the positive z-side of the ECAL for a typical running period.*

active. The figure is shown as seen from the vertex: the inner disc corresponds to the endcap, the outer disc to the positive-z half-barrel[1]. The black boxes reflect

---

[1]The small hole inside the endcap reflects the entry point of the beam-pipe of an additional low-energy calibration device, the RFQ [34]. This instrument was developed to provide an additional low energy calibration and was only used from 1995 onwards.

dead rings and dead crystals. After the real detector simulation, the Monte Carlo reproduces this plot very well.

The impact of all these ECAL deficiencies on the energy imbalance distributions of the $q\bar{q}$ events is shown in figure 3.2. As can be seen, both the longitudinal and
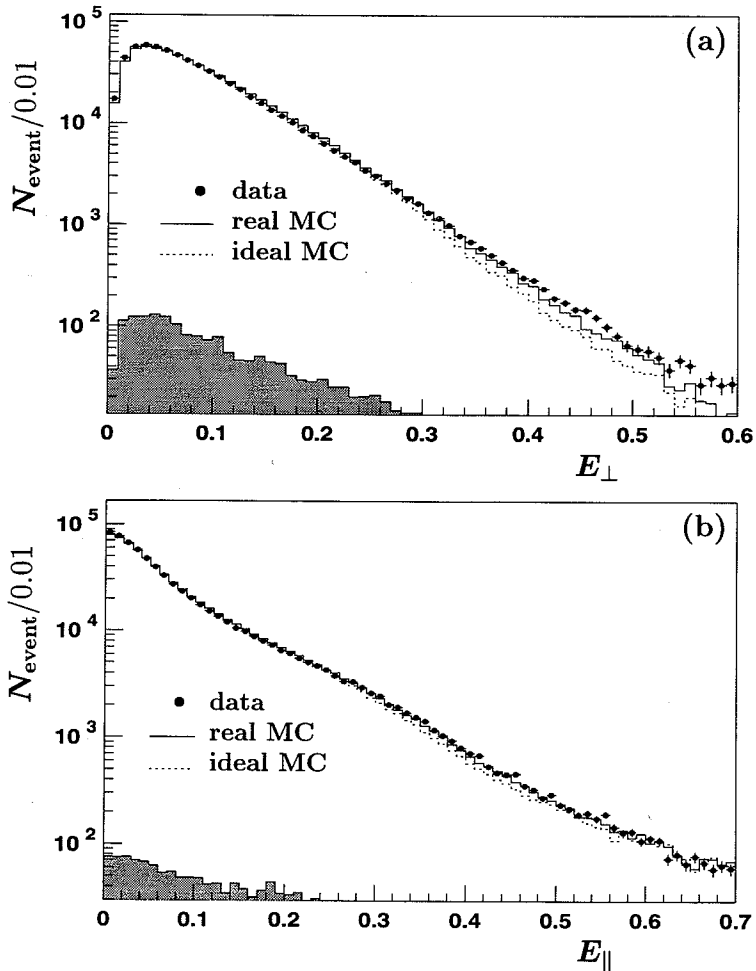
Figure 3.2: *The transverse (a) and longitudinal (b) energy imbalance distributions of $q\bar{q}$ events before and after real detector simulation. Dots represent the data (see chapter 4); the lines (solid or dashed) the various Monte Carlo predictions. The shaded area denotes the background contribution. The Monte Carlo histograms are normalised to the number of data-events in the acceptance region.*

transverse energy imbalance Monte Carlo predictions lie substantially closer to the data after real detector simulation. Once more the data used in these plots are from a sample, the selection of which will be described in chapter 4.

For the cross section measurements, there is one additional (a-posteriori) real detector correction to the number of clusters (N_{ASRC}), in order to take better into account ECAL noise events. It is obtained from a study of so-called beam-gate data. These data are taken without any trigger requirement once every 10 seconds at beam crossing time and therefore representative for the ECAL noise background mentioned.

The distribution of the number of ECAL bumps (N_{EBMP}), obtained from beam gate data is shown in figure 3.3. A double exponential is fitted to these distributions. Using the fit results, a number of bumps is generated which is added to the number of ASRCs on the Monte Carlo level. Thus, a convolution of the distribution of N_{ASRC} resulting from the Monte Carlo with the N_{EBMP} distribution from the beam gate data is realised. On average, a number of 0.36 and 0.30 bumps per event is added to the 1992 and 1993 $q\bar{q}$ Monte Carlo, respectively.
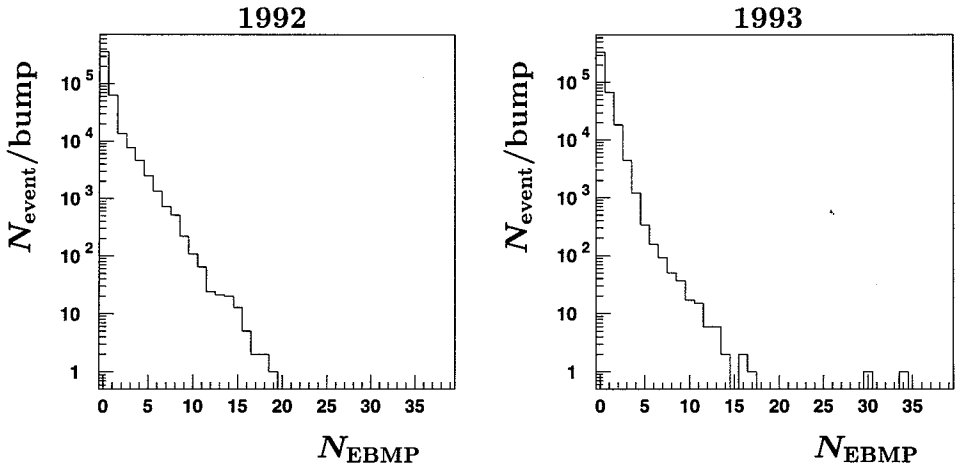
Figure 3.3: *The number of bumps N_{EBMP} in the ECAL observed in beam-gate data.*

3.2.2 TEC Simulation

After ideal Monte Carlo simulation of the TEC, discrepancies remain in the distributions of track parameters, because one has not yet properly taken into account the inhomogeneities in the electric field near the anode and cathode planes, the wire

precision, the inefficient wires, the malfunctioning TEC sectors, etc. As an illustration of these remaining problems, figure 3.4 shows a comparison with ideal Monte Carlo predictions of the track transverse momentum distribution of the data. Note the logarithmic scale of the y-axis. Ideally, all discrepancies observed, and especially those at high transverse momenta, should vanish after real-TEC corrections.
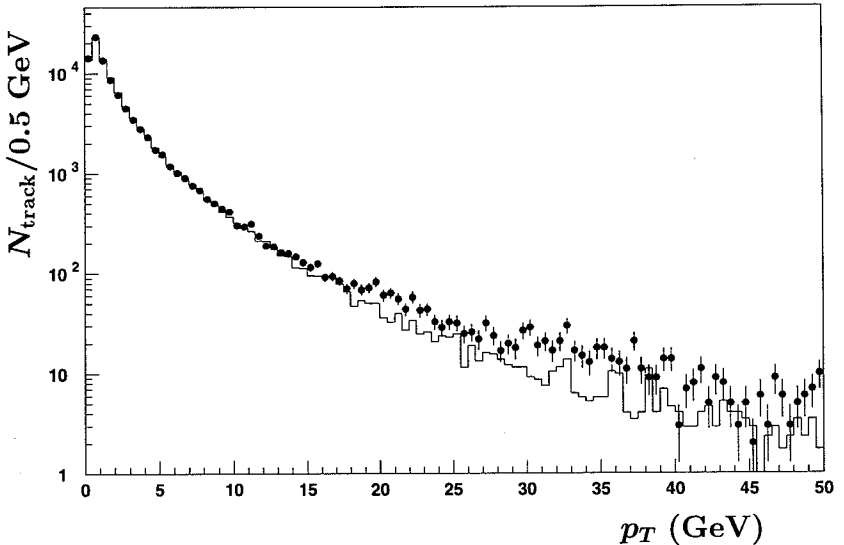
Figure 3.4: *The track transverse momentum distribution as measured by the TEC for a typical 1993 run period (dots) compared with the ideal detector Monte Carlo (histogram). The Monte Carlo distribution is normalised to the number of data-tracks after the selection (see text).*

Figure 3.4 is obtained using tracks satisfying the following criteria:

- a distance of closest approach with respect to the fill vertex $|\text{DCA}| < 10$ mm;

- a transverse momentum $p_T > 0.3$ GeV;

- a number of hits, retained for the final circle fit (see 2.3.1) $N_{\text{hit}} \geq 20$;

- a polar angle θ satisfying $|\cos\theta| < 0.9$.

The cuts on the DCA and the p_T discriminate between backscattered tracks (see section 3.1) and tracks from the vertex. Tracks which need both the DCA and p_T cut to be eliminated are in essence backscattered tracks which coincidentally pass near the vertex. About 85% of the tracks genuinely originating from the vertex

survive the DCA and p_T cuts. As will become clear from section 4.2, the p_T cut also functions as a rather loose charge-measurement quality selector. Together the third and fourth cut create a fiducial volume for tracks; it is illustrated in figure 3.5, where the number of hits is plotted as a function of θ. The figure is made without the track selection criteria. The N_{hit} cut effectively removes tracks with a large
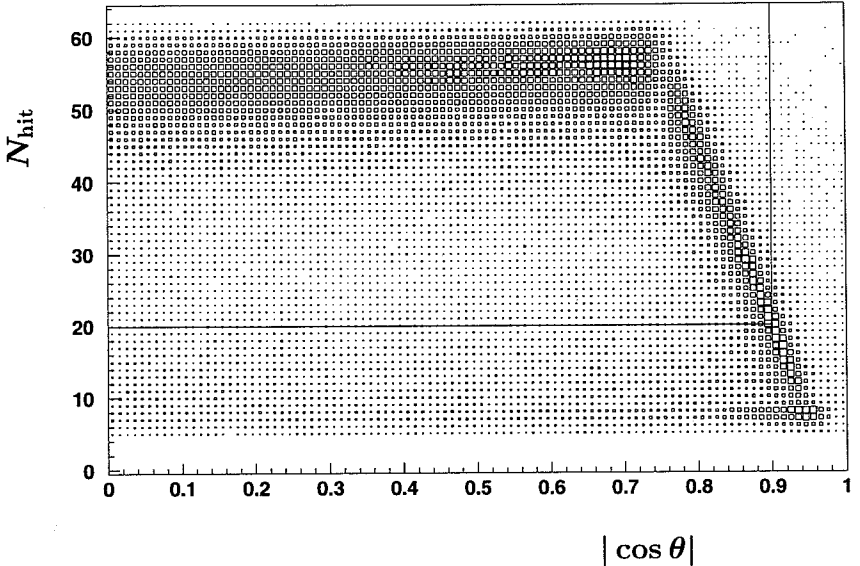
Figure 3.5: *The number of hits as a function of θ. The size of each square is proportional to the number of tracks it contains. No track selection criteria are applied. The straight lines delineate the N_{hit} versus $|\cos\theta|$ acceptance region.*

error on the transverse momentum; however, imposed after the previous cuts, this eliminates only a small amount of tracks. The $\cos\theta$-cut eliminates the very forward and backward regions, where the p_T precision deteriorates rapidly. Unless specified otherwise, the above selection criteria are imposed in all distributions shown below.

For our determination of the real-TEC correction, the most crucial variable turns out to be the *spread* of the TEC-hits around the "real" TEC track. To study this spread, use will be made of d_{hit}, a weighted circle-fit distance, defined as:

$$d_{\text{hit}} = \frac{D_{\text{hit}}}{\delta_{\text{hit}}}, \tag{3.1}$$

where D_{hit} is the distance (in the xy-plane) of the hit to a fitted circle, as described in section 2.3.1, also called the xy-*residual*, and δ_{hit} the error on the position of that hit in the same plane. The width of the D_{hit} distribution is a measure of the average spread of the hits around a TEC track. The error δ_{hit} results from the TEC calibration and is a function of the distance to the anode and cathode wire planes [35, 36]. The net effect of the already mentioned inhomogeneities of the electric field is a larger spread of the hits (i.e. larger errors) if the particle passes nearby the anode and/or cathode wires than in the case when the particle passes far away from these wires.

As input for the smearing and elimination techniques to be discussed further on we examine the dependence of $\sigma(d_{hit})$ on ϕ_{local} and p_T.

Figure 3.6 shows the dependence of the width $\sigma(d_{hit})$ on the local azimuthal angle ϕ_{local}, i.e. the angle between the track and the nearest left-lying inner TEC-sector cathode plane. Note that each inner TEC sector is associated with *two* outer TEC sectors (see figure 2.2). In practice, four TEC regions are distinguished:
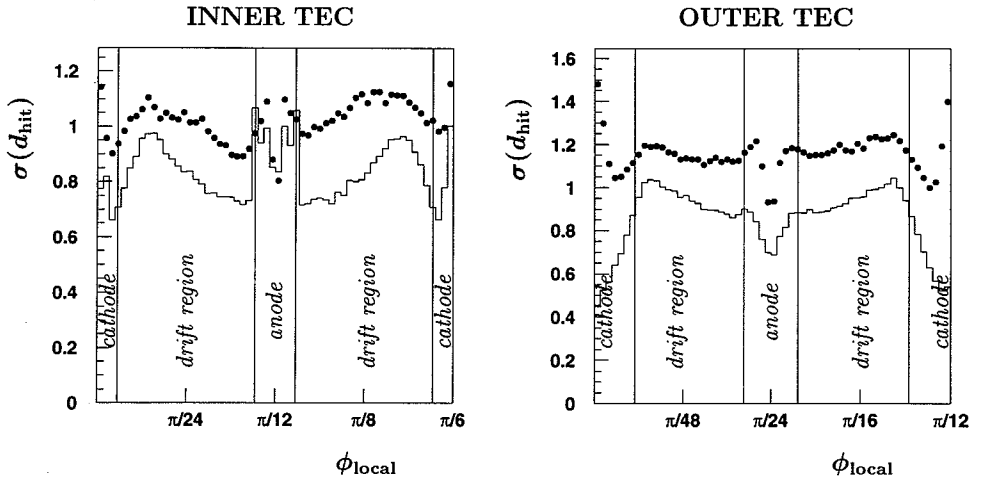
Figure 3.6: *The dependence of the width of d_{hit} on ϕ_{local}. Dots represent the data; the histogram the Monte Carlo prediction.*

- $\phi_{local} < 0.03$ and $(\pi/6 - \phi_{local}) < 0.03$,
  i.e. the inner TEC cathode and part of the outer TEC cathode region;

- $|\phi_{local} - \pi/12| < 0.03$,
  i.e. the inner TEC anode and the remaining outer TEC cathode region;

- $|\phi_{\text{local}} - \pi/24| < 0.02$ and $|\phi_{\text{local}} - \pi/8| < 0.02$,
  i.e. the outer TEC anode region;

- the remaining regions of ϕ_{local}, i.e. the drift regions.

As observed in figure 3.6, $\sigma(d_{\text{hit}})$ varies rapidly in the cathode and anode regions but behaves more smoothly in the drift regions. The Monte Carlo prediction shows qualitatively the same behaviour as the data, apart from the cathode regions of the outer TEC. As observed, for data in all regions, $\sigma(d_{\text{hit}}) \approx 1$, indicating that the error has been correctly estimated. For Monte Carlo however, the average $\sigma(d_{\text{hit}})$ is much lower, indicating that in the ideal Monte Carlo the spread is underestimated.

As low energetic tracks suffer more from multiple scattering than high energy ones, one a-priori also expects a p_T-dependence of d_{hit}. To illustrate this dependence, the width of d_{hit} is plotted as a function of p_T in figure 3.7. One observes that for
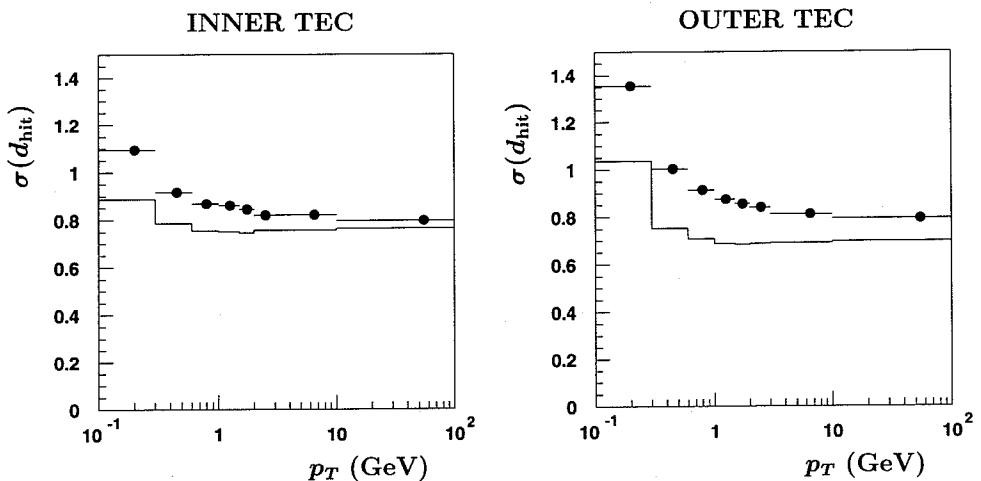
Figure 3.7: *The dependence of the width of d_{hit} on the transverse momentum. Dots represent the data; the histogram the Monte Carlo prediction.*

decreasing p_T the width increases below 0.6 GeV for the inner TEC and below 2 GeV for the outer TEC; above these values, the width is nearly constant.

Hit Elimination and Hit Smearing

The agreement between data and the ideal Monte Carlo can be improved by smearing (i.e. by artificially broadening) the hit distribution in the Monte Carlo and by

eliminating poorly measured hits in the data. In detail, this is implemented via the following three steps[2]:

1. Smearing in x-y of d_{hit} of all Monte Carlo track hits and recalculation of the smeared hit coordinates and errors.

2. Exclusion of the $r\phi$-plane information of track hits which are too close to the cathode or the anode, using the following cuts:

   – a hit-distance to the cathode $d(\text{hit}, \text{cathode}) < 2$ mm;
   – a hit-distance to the anode $d(\text{hit}, \text{anode}) < 3.2$ mm.

3. Refitting the remaining hits in order to obtain new $r\phi$ track parameters.

The first step essentially fits the Monte Carlo d_{hit} distribution to the data. After this step, new xy-plane coordinates and errors have to be calculated, because these coordinates are correlated with d_{hit}. The second step eliminates regions where there are large discrepancies between the data and the Monte Carlo. The cut values on the hit-distances chosen are a compromise between momentum precision improvement and loss of near-anode and cathode tracks. The cut on the distance to the anode was varied between 3.2 mm, i.e. the exact distance from the TEC grid wires (see figure 2.2) to the anode wires, and 4.5 mm. Higher values than 3.2 mm did not significantly improve the momentum precision. The cut on the distance to the cathode was varied from 1 mm to 3 mm. The value of 1 mm turned out to be insufficient, as it left remaining discrepancies in the ϕ_{local} distribution. A cut of 2 mm was chosen because further cutting did not improve the transverse momentum precision anymore. The total number of track hits surviving this step is denoted by $N_{\text{hit}}^{r\phi}$. Note that step 2 leaves the sz-information of the track unaffected, since this step only removes the $r\phi$-information of hits which are too close to the anode or cathode. It preserves the z-information of these hits, as this coordinate is unaffected by the $r\phi$-inhomogeneities of the electric field. The third step is self-evident.

The function used for the hit smearing is based on the distributions of d_{hit}. To take into account effects due to the amount of the detector material traversed by the tracks, the inner and outer TEC are treated separately. Including the full p_T-dependence of d_{hit} in the smearing function would add an extra dimension to the problem. A relatively easy and sufficient smearing is obtained by only considering tracks in p_T regions for which $\sigma(d_{\text{hit}})$ is nearly independent of p_T. These regions are $p_T > 0.6$ GeV for the inner TEC and $p_T > 2.0$ GeV for the outer TEC (see figure 3.7). Although these p_T-regions are different we use – as a compromise – a common

---

[2] The description as given is correct in principle. In practice a pre-selection on the anode hits is required because of the unequal way in which the TEC calibration was performed near the anode and cathode, respectively. The description of this complication is omitted for the sake of simplicity. Note however that the "before-smearing" plots 3.7, 3.8 and 3.9 are made *with* this pre-cut.

region, namely $p_T > 1$ GeV. The function thus found is subsequently used to smear tracks for the whole p_T-spectrum.

Figure 3.8 shows the distributions of d_{hit} for data and Monte Carlo, before and
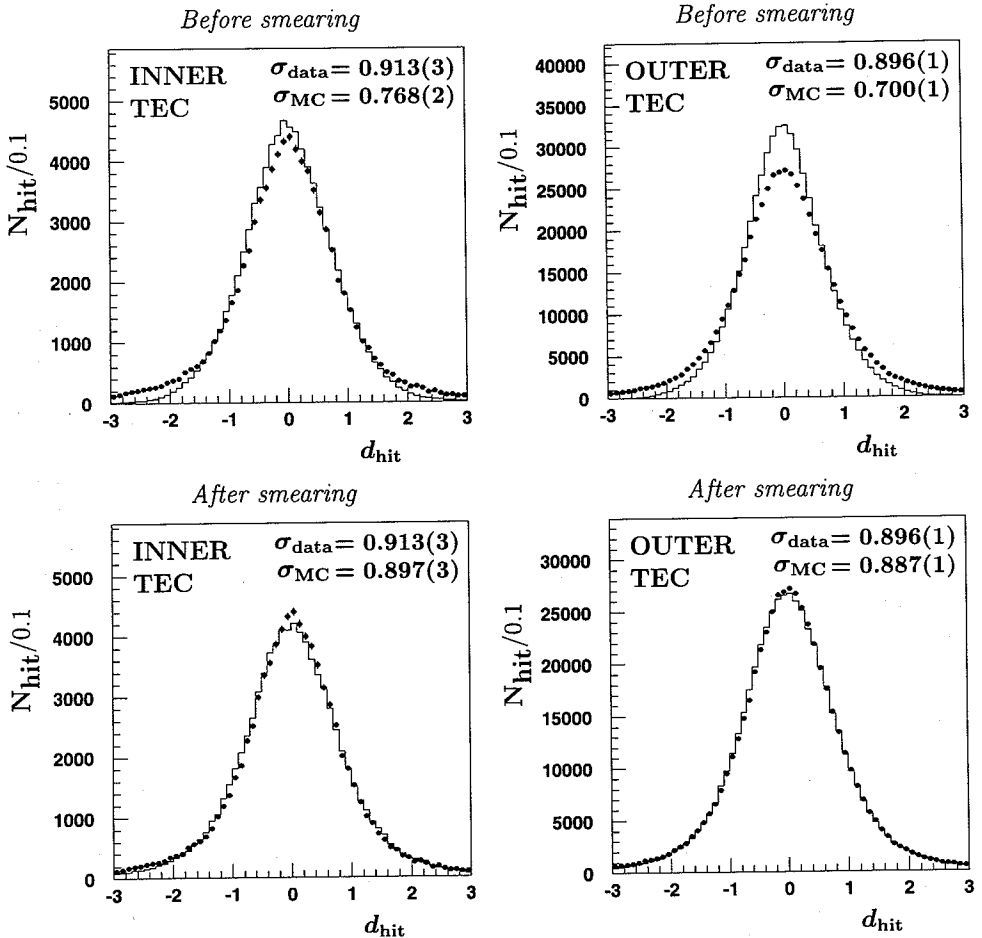
Figure 3.8: *Distributions of d_{hit} for data (dots) and Monte Carlo (histograms). The upper plots show the comparison before smearing; the lower ones the comparison after smearing. Hits on tracks with $p_T < 1$ GeV are excluded from the plots.*

after smearing. All hits on tracks with $p_T < 1$ GeV are excluded from these distribu-

tions. Both for the inner and the outer TEC, a nearly perfect agreement is obtained after smearing. More technical details about the smearing are given in appendix A.

As additional checks, a comparison of d_{hit} as a function of ϕ_{local} and as a function of p_T before and after hit smearing are shown in figures 3.9 and 3.10 respectively. Note that in contrast to figure 3.6 (but consistent with figure 3.8), again hits on
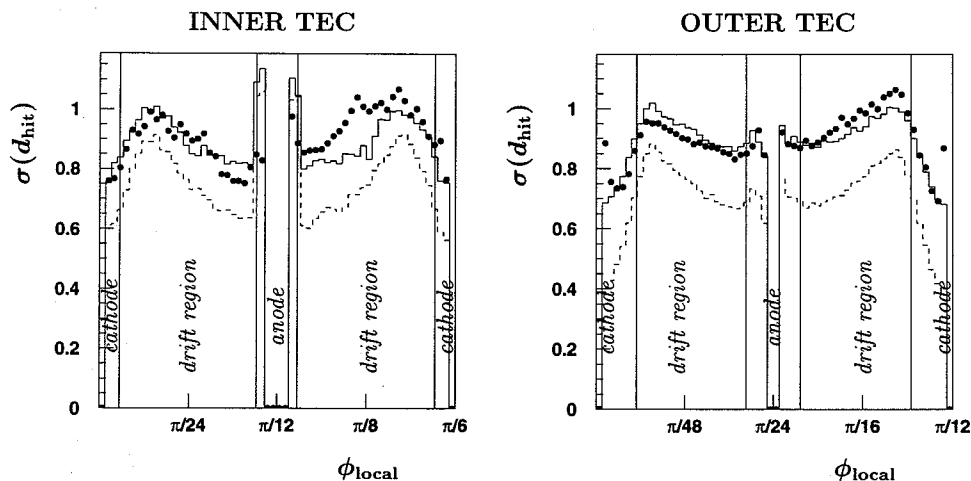
Figure 3.9: *The dependence of the width on the local azimuthal angle. The dots represent the data, the solid line the Monte Carlo after and the dashed line the Monte Carlo before hit smearing and elimination. Hits on tracks with $p_T <1$ GeV are excluded from these distributions.*

tracks with $p_T <1$ GeV are excluded from the plots in figure 3.9, which leads to lower average values for $\sigma(d_{hit})$. After smearing, the agreement between data and Monte Carlo in figure 3.9 is significantly improved, although some discrepancies remain, in particular in the part of the drift region of the outer TEC near the cathode (both on the left and the right side of the anode). The discrepancy in the inner TEC anode region also persists. The plots in figure 3.10 show a certain oversmearing for tracks having a transverse momentum $p_T > 2$ GeV, and an undersmearing below 2 GeV. The overall impact of these effects will be found to be relatively small however.

Further distributions of track parameters are shown in figures 3.11 and 3.12. As these plots show, hit smearing and elimination has a significant positive effect on the agreement between the track parameter distributions of the data and the Monte Carlo. Both the p_T and the DCA Monte Carlo distributions broaden after hit smearing. The Monte Carlo ϕ_{local} distribution reproduces the dips in the data more faithfully. The peak of the Monte Carlo distribution of the number of hits (which is

INNER TEC   OUTER TEC
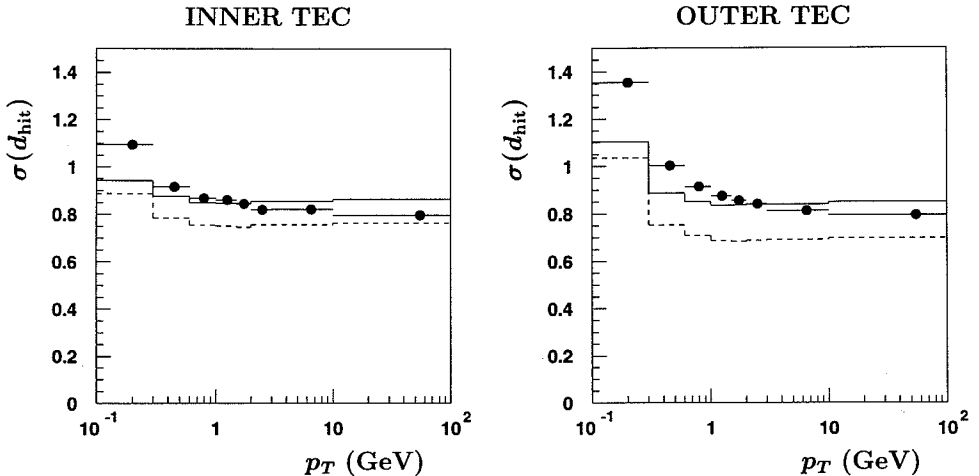
Figure 3.10: *The dependence of the width of d_{hit} on the transverse momentum. Dots represent the data; the solid line the Monte Carlo after and the dashed line the Monte Carlo before hit smearing and elimination.*

the number of hits containing $r\phi$-information *after* smearing and elimination) shifts to the right and gets broader, although the width observed in the data is still not yet fully reproduced. The same observation applies to the χ^2/df distribution associated with the track circle fit (see chapter 2). The Monte Carlo distribution $P(\chi^2, df)$ changes dramatically; its shape becomes qualitatively the same as the one for the data (except for very low probabilities) and there is an overall improved agreement between the two distributions.

Several effects could be responsible for the remaining discrepancies between the data and Monte Carlo distributions. The most important ones are those related to the remaining discrepancies visible on the right of the inner TEC anode region in figure 3.9 after the Monte Carlo smearing. Other effects which are not or incompletely taken into account and therefore could be a reason for these discrepancies, are the Lorentz force (the left-right asymmetry in figure 3.9), multiple scattering (see figure 3.11(d)), noisy wires (figure 3.12(b)) and inhomogeneities of the electric field near the TEC flanges. The overall influence of these remaining effects on the asymmetry are estimated in chapter 6 and turn out to be small.
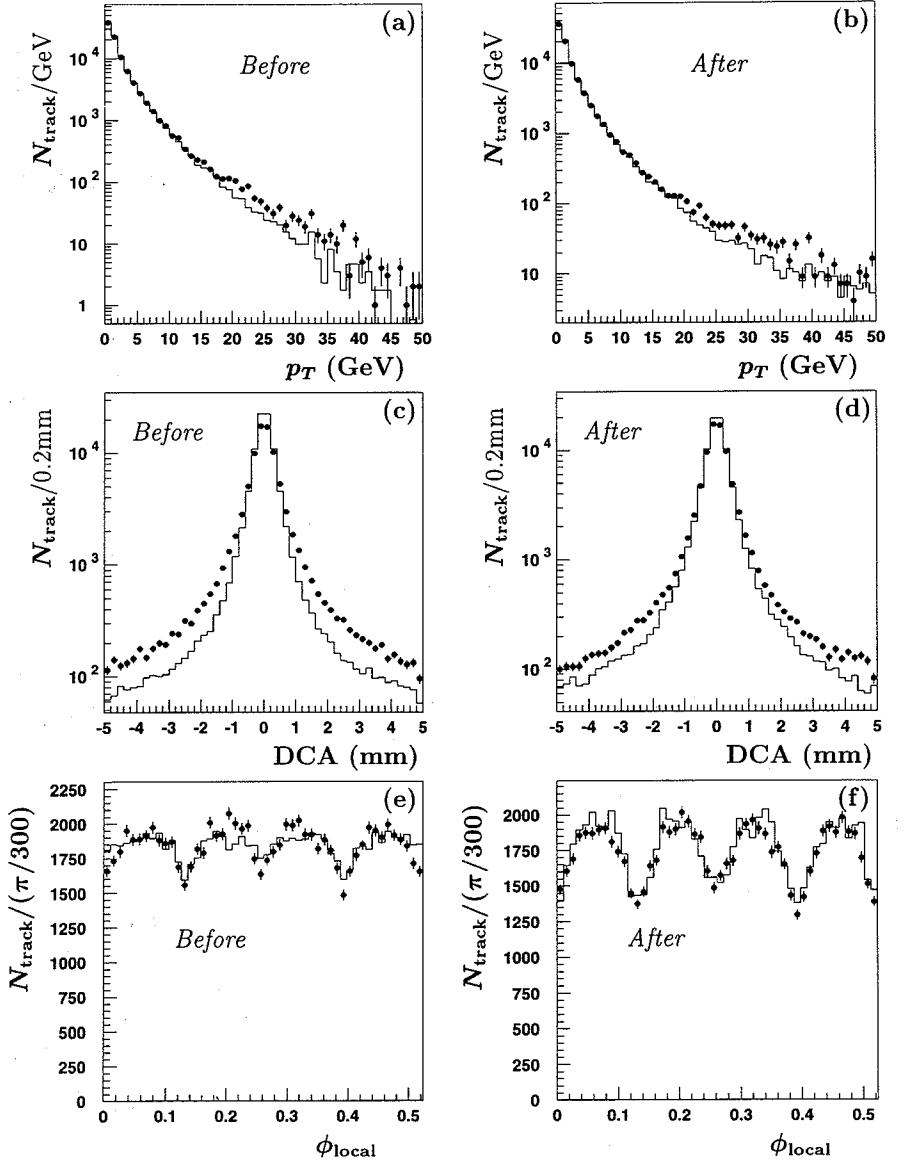
Figure 3.11: *Comparison of track parameter distributions before and after TEC-hit smearing and elimination. Dots represent the data; the histograms the Monte Carlo predictions. The Monte Carlo histograms are normalised to the number of accepted data-tracks before and after hit elimination, respectively.*
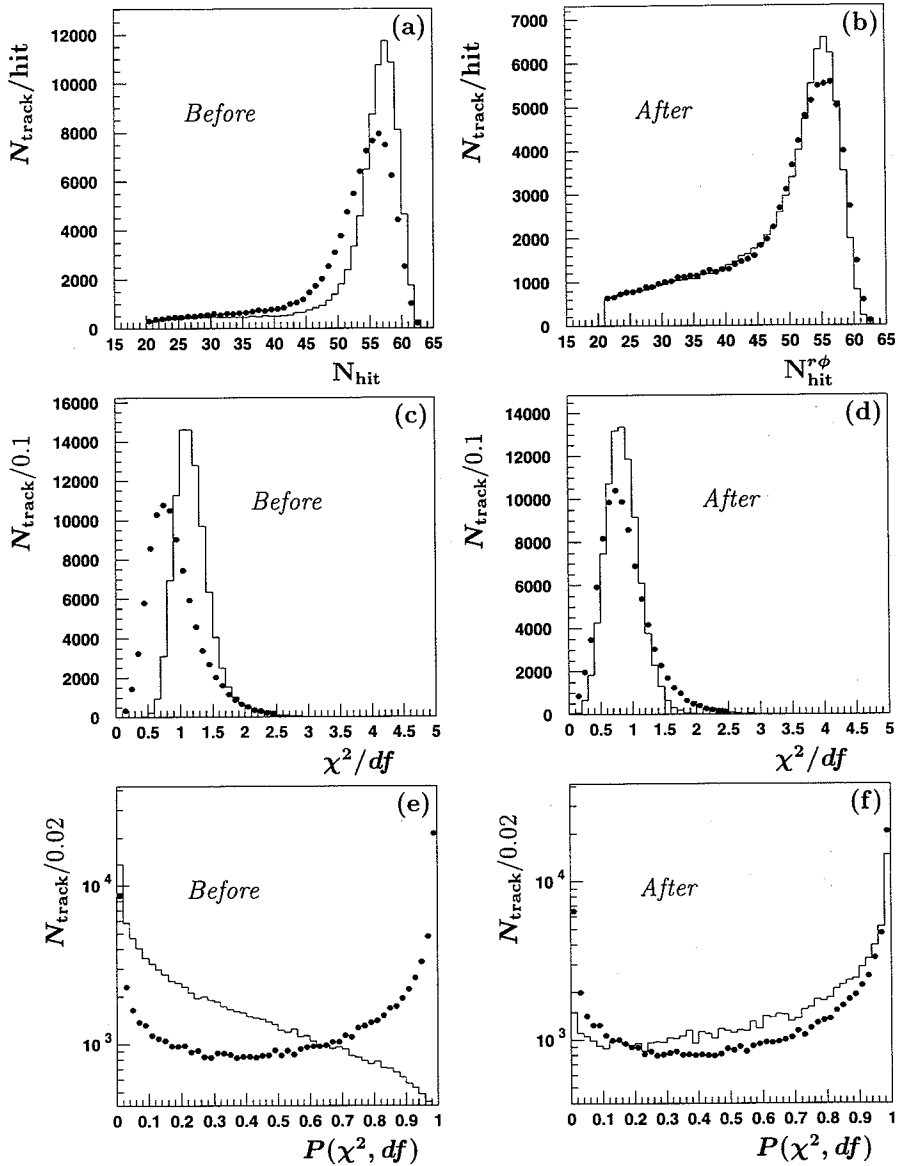
Figure 3.12: *Comparison of track parameter distributions before and after TEC-hit smearing and elimination. Dots represent the data; the histograms the Monte Carlo predictions. The Monte Carlo histograms are normalised to the number of data-tracks before and after hit elimination, respectively.*

Sector Inefficiencies

In the previous section global effects, i.e. effects which are the same for all sectors (and could therefore be averaged) were discussed. There are also local effects which are different from sector to sector; they are briefly discussed below.

During data taking, several local effects can reduce the track selection efficiency. If a (half)sector is noisy, e.g. because of poor beam conditions, the high voltage power supply gets saturated and the sector must be switched off. If the voltages are insufficiently high, wires do not function properly and yield less track-hits than expected. In addition, there can be "dead" channels which do not produce signals for a prolonged period of time.

In principle, the L3 data-base keeps track of all this information. However, the data-base information on the TEC is not always sufficient. If the (half)sector high voltages are too low for only a very small period of time, it may remain unnoticed by the on-line monitoring program. These effects can be taken into account a posteriori by monitoring each TEC (half)sector separately by means of the track-rate of the $q\bar{q}$ channel in the half-sector under consideration. As discussed in reference 30, the optimum length found for the monitoring time interval is four minutes, leading to a so called "four-minute-list".

Figure 3.13 shows a comparison of the number of $q\bar{q}$-event tracks in each half-sector with Monte Carlo after inclusion of the four minute list. As can be seen, all deviations are compatible with normal statistical fluctuations, with one exception: the left-half of sector 4. This half-sector indicates an effect significant at the 95% CL. The effect is due to the bad groundings of the grid wires of this sector, which in turn makes the electric field not well defined. This effect is too intermittent to be incorporated in the four-minute list.

A straightforward solution for this remaining discrepancy is an additional correction just for tracks in the left-half of sector 4. A probability is calculated using the ratio of the observed number of tracks in this half-sector to the expected number of tracks, calculated from all other half-sectors combined. Thus, an additional half-sector inefficiency is derived for the left-half of sector 4, of

$$1 - \varepsilon_{4,L} = 0.227 \pm 0.031, \tag{3.2}$$

where error quoted is estimated using the variance on the number of tracks in the other half-sectors. The probability is used to randomly reject Monte Carlo tracks in the sector concerned.
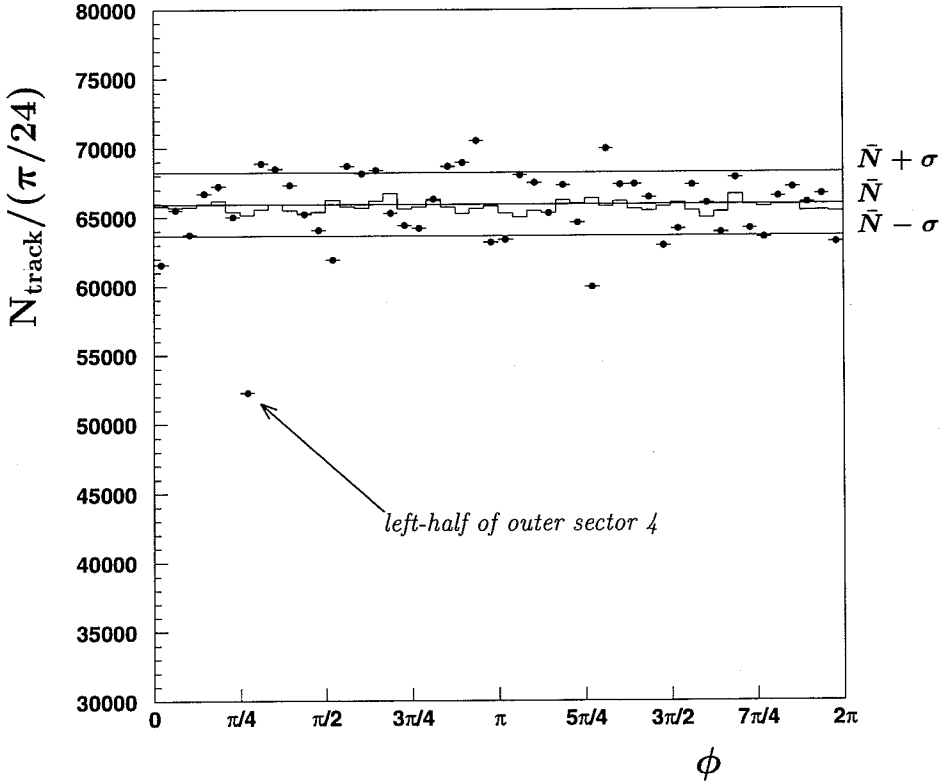
Figure 3.13: *The number of tracks found in each TEC half-sector compared with the Monte Carlo prediction taking into account the four minute efficiency list. The binning is such, that each bin corresponds to one half-sector.*

4

Event Selection

A precise measurement of the cross section requires a large data sample with a small background. A measurement of the forward-backward asymmetry on the other hand, needs a sample carrying sufficient charge information; this in turn requires events with sufficient TEC-tracks satisfying appropriate charge-measurement quality criteria. In this chapter, we first discuss the hadronic cross-section event selection criteria. Subsequently we discuss in more detail the methods used to obtain a $q\bar{q}$ sample containing reliable charge information.

4.1 Hadron Selection

4.1.1 Hadron Characteristics and Background Sources

A pure hadron sample can only be obtained by applying selection criteria which sharply differentiate real hadrons from background events. This requires a thorough understanding of all background sources. These sources are all the non-$q\bar{q}$ e^+e^--interactions, the cosmic muons, the beam-wall events, the beam-gas events and the electronics noise in the (sub)detector(s).

Since the CM energy $\sqrt{s}$ is high, the hadronisation process of a $q\bar{q}$ pair yields a large number of particles. Thus, a large (charged) multiplicity is expected. In a $q\bar{q}$ event, the number of particles which decay weakly is small. Therefore, only a small fraction of the initial energy is carried away by neutrinos. The average visible energy is expected to be close to $\sqrt{s}$ and the energy-momentum configuration of the event well balanced[1].

The characteristics of a genuine $q\bar{q}$-event have to be compared to those of the

---

[1]Only in $b\bar{b}$ events, one has a somewhat larger energy fraction carried off by neutrinos. However, this fraction is not so large as to lead to significant differences in the above mentioned characteristics.

events which can contribute to its background:

- e^+e^- background: resulting from $e^+e^- \to \gamma/Z \to e^+e^-$, the Bhabha events. They have a high visible energy, but a low multiplicity. Because of the possibility of t-channel photon exchange, a substantial fraction of the events concentrate in the forward and backward regions of the detector[2]. Since there are no neutrinos, the energy distribution is well balanced.

- $\mu^+\mu^-$ background: resulting from $e^+e^- \to \gamma/Z \to \mu^+\mu^-$. Dimuon events again possess a low multiplicity and a momentum sum close to the CM energy.

- $\tau^+\tau^-$ background: resulting from $e^+e^- \to \gamma/Z \to \tau^+\tau^-$. Tau events show a relatively low visible energy and display more energy imbalance. This is because the τ lepton decays into hadrons, electrons or muons, under the emission of neutrinos. Compared to a hadron event, the multiplicity is still low, but higher than a typical dimuon or Bhabha event.

- $e^+e^- f\bar{f}$ background: These are the so-called two photon events and are formed by double initial state radiation: both the incoming electron and positron radiate a photon, which in turn, interact to form a $f\bar{f}$ pair. The remaining electron and positron are so little deflected that they usually stay in the beam pipe and are therefore undetectable. Two photon events have a low visible energy and a large longitudinal energy imbalance. The multiplicity is low in the case $f = e, \mu, \tau$. When $f = q$, the multiplicity is higher than the average tau-event multiplicity, but still lower than the $q\bar{q}$ multiplicity.

- cosmic background: A cosmic event can be just one cosmic muon, or a whole "shower" of cosmic particles. In the first case, the multiplicity is low; in the second case, it is high. Their visible energy distribution covers a wide range; the same is true for the energy imbalance distributions. Cosmics can occur at any moment, hence, also during a bunch crossing and even (although improbable [37]) in coincidence with an e^+e^- interaction.

- beam-wall background: This background source comes from the interaction of beam electrons (or positrons) with the edges of the beam pipe. Beam-wall events have a low visible energy, their energy longitudinal imbalance is high and so is their multiplicity.

- beam-gas background: This background source results from the interaction of beam electrons (positrons) with molecules still left in the beam pipe as the result of the vacuum not being perfect. Beam-gas events have essentially the same characteristics as beam-wall events.

---

[2]It is precisely a subsample of these extremely forward and backward Bhabhas, which is used for the luminosity measurement.

- electronics noise background: Possible causes of this background source are varied and numerous: insufficient electronics grounding, movements of the support tube or even the lights in the L3-hall, etc. For this analysis, the relevant electronics noise usually manifests itself as fake HCAL energy depositions[3]. HCAL noise typically has a very low associated ECAL energy and a high hit multiplicity in the HCAL.

Apart from the electronics noise, the background channels can be divided in two categories. The first category contains the background sources which *scale* with the Z-resonance cross section, i.e. the e^+e^-, $\mu^+\mu^-$ and $\tau^+\tau^-$ backgrounds. The second category contains the sources which do *not* scale with this resonance cross section and is generally denoted as the *non-resonant* (NR) background: two photon, cosmic, beam-gas and beam-wall events.

The characteristics of the channels as given above are limited to those observable using the calorimeters and the muon chambers. The TEC is not used, since its angular coverage is limited; a measurement of the cross section based on TEC information would therefore be significantly less accurate.

4.1.2 Selection Criteria

From the characteristics of the $q\bar{q}$ channel and the background channels, it is clear that requiring the ASRC multiplicity to be high and the visible energy close to $\sqrt{s}$ will provide the primary differentiation between signal and background. However, these two cuts are not sufficient. Three significant background sources remain: the remnant taus, the non-resonant events and the electronics noise events. Tau events exceptionally can have a large multiplicity when the tau decays hadronically and a large visible energy when the decay neutrino is emitted with relatively low energy. NR events have large visible energy when a beam particle is subjected to a "hard" collision with a gas or a beam-pipe molecule, or when the photons radiated off from an electron and positron have large energy. Electronic noise events sometimes display large hit multiplicities in the HCAL, thus leading to many ASRCs.

The usual L3 $q\bar{q}$ selection criteria are as follows:

(1) $0.5 < E_{\mathrm{vis}}/\sqrt{s} < 2.0$;

(2) $N_{\mathrm{ASRC}} \geq 13$ (for barrel events: $|\cos\theta_T| < 0.743$)
    $N_{\mathrm{ASRC}} \geq 17$ (for endcap events: $|\cos\theta_T| > 0.743$)

(3) $E_\perp < 0.5$;

(4) $E_\parallel < 0.6$;

---

[3]It can also appear as fake ECAL bumps, i.e. as an unphysically large array of adjacent crystals containing very low energy depositions. However, this noise background is already eliminated by exclusion of such bumps types during the event reconstruction (see chapter 2)

(5) $E_{\mathrm{ECAL}} > 5.0$ GeV;

(6) $N_{\mathrm{hitHC}} < 600$.

The quantities E_{vis}, $E_{\perp}$ and $E_{\parallel}$ are those defined by equations 2.8, 2.10 and 2.11, respectively. As explained in chapter 2, they are calculated from calorimetric and MUCH information. The choice of the rescaled quantity $E_{\mathrm{vis}}/\sqrt{s}$ instead of E_{vis} is because of the scaling of the visible energy with the beam energy. The number N_{ASRC} is the total number of ASRCs and directly related to the particle multiplicity of the event, as seen by the calorimeters. A distinction has to be made between barrel and endcap, since the ECAL endcaps have roughly the same crystal segmentation as the ECAL barrel but the endcap crystals are on average further away from the interaction point; this leads to larger average multiplicities for all channels in the endcaps. The angle θ_T is the polar angle of the thrust axis, defined in 2.12. The two energy imbalance cuts reject remaining tau and NR background. The last two cuts are introduced to remove HCAL noise events. The symbol E_{ECAL} represents the total ECAL energy; N_{hitHC} the hit multiplicity in the HCAL.

Distributions of the selection variables are shown in figures 4.1 to 4.4.
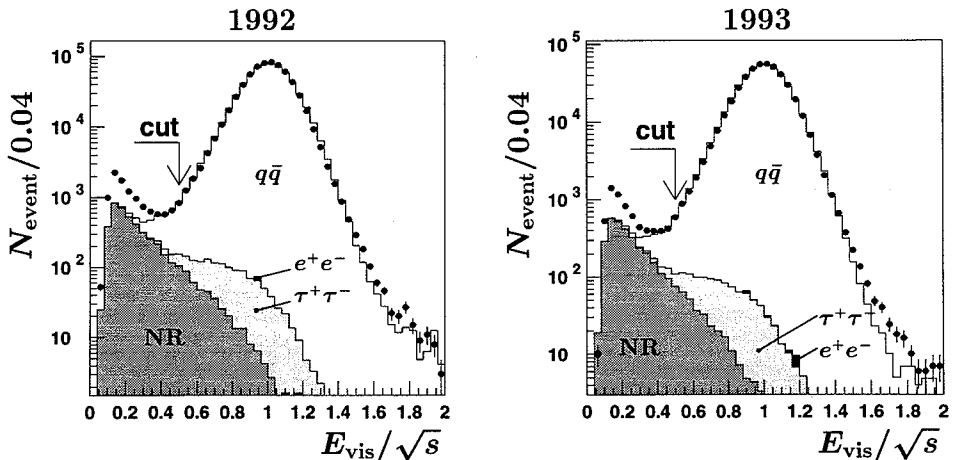
Figure 4.1: *Distributions of the scaled visible energy for 1992 and 1993 peak data, compared with the Monte Carlo predictions. Dots represent the data; the cumulative histogram shows the Monte Carlo predictions. The different shadings (from white to grey) indicate the $q\bar{q}$-contribution and the background contributions, respectively. The Monte Carlo distributions are normalised to the number of accepted hadrons in the data. Note that the upper cut on E_{vis} coincides with the figure border.*

1992 Barrel

1993 Barrel

1992 Endcap

1993 Endcap
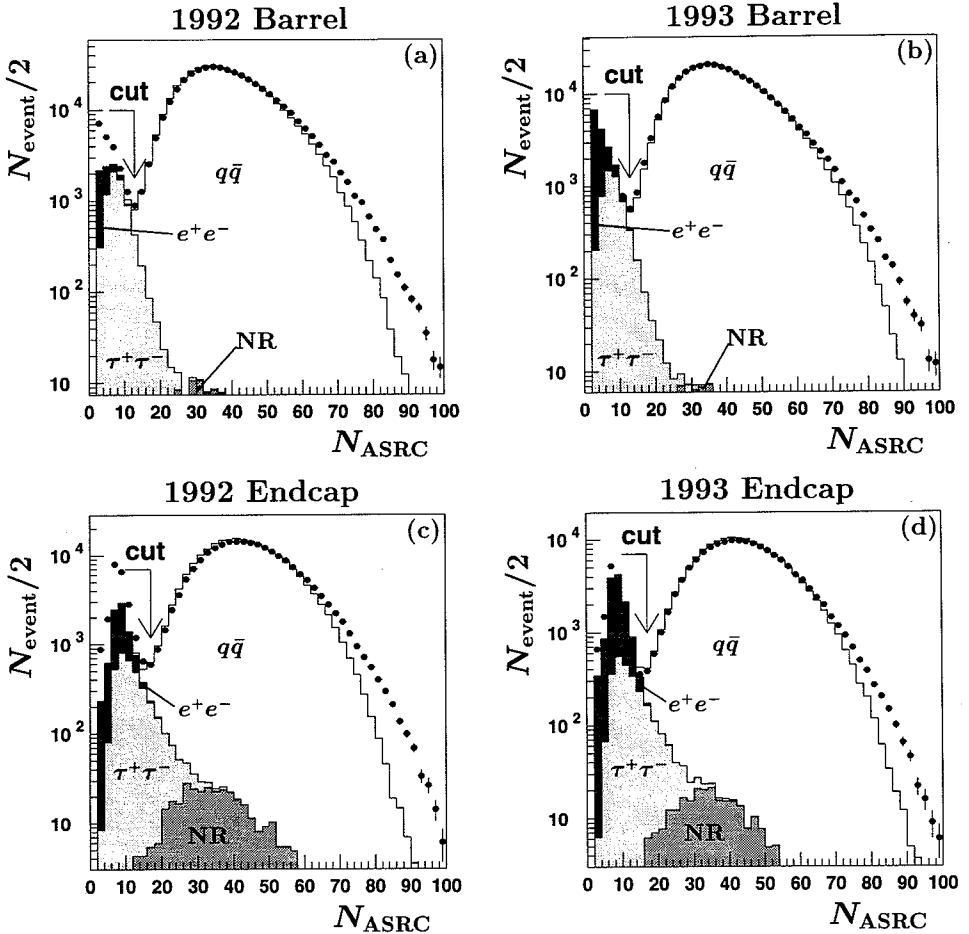
Figure 4.2: *Distributions of the multiplicity N_{ASRC} for 1992 and 1993 peak data, compared with the Monte Carlo predictions. The definition of the symbols, shadings and normalisations are the same as for figure 4.1.*

For the 1993 distributions, only the Z-peak data are shown; the distributions for off peak data are very similar. The histograms are made after applying all the cuts, except for the one on the variable which is plotted. Notice the log scale of all distributions.

In the distributions shown, the Monte Carlo channels considered are $q\bar{q}$, e^+e^-, $\tau^+\tau^-$ and NR. The Monte Carlo hadrons were generated using the JETSET program [17] (version 7.3; see chapter 3). The $\tau^+\tau^-$ background was simulated with the KORALZ program [38]. For the 1992 data, the Bhabha background was sim-
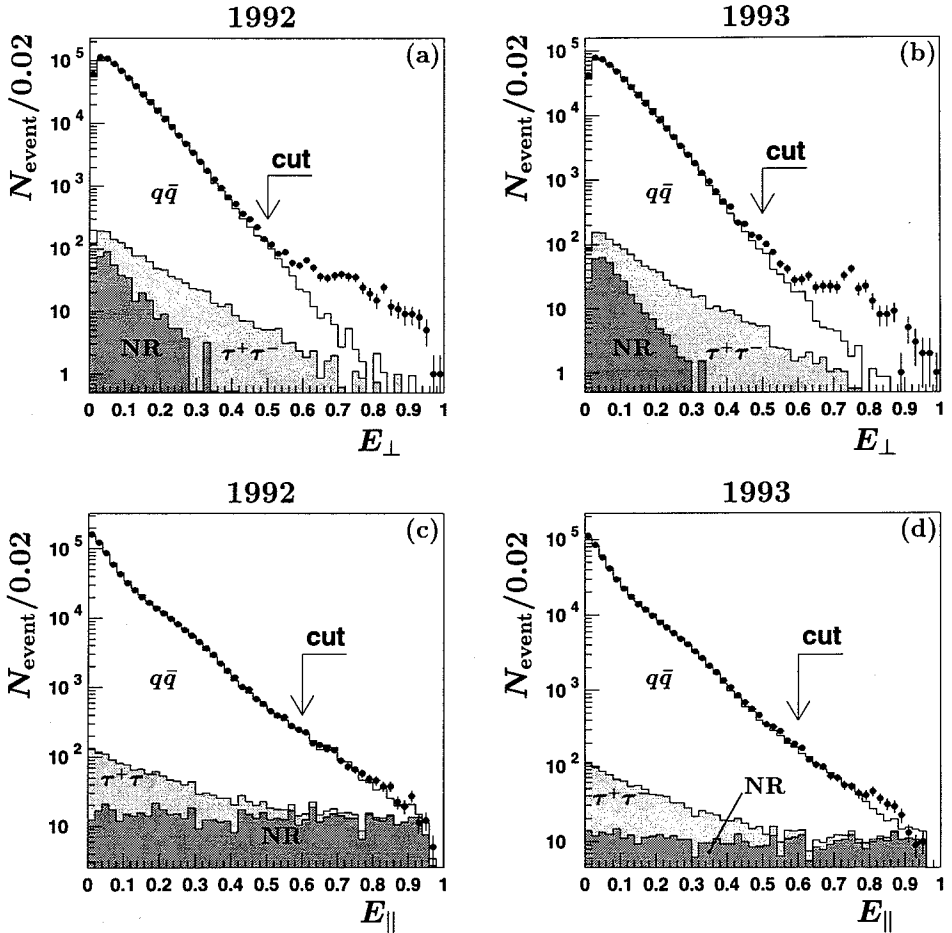
Figure 4.3: *The energy imbalance distributions for 1992 and 1993 peak data, compared with the Monte Carlo predictions. Figures (a) and (b) are the transverse imbalances; (c) and (d) the longitudinal imbalances. The definition of the symbols, shadings and normalisations are the same as for figure 4.1.*

ulated with the BABAMC program [39]. For 1993, BABAMC was replaced by the BHAGENE program [40], because it yielded in principle a better description of the t-channel contribution. The two photon interactions were simulated using the DIAG36 program [41]. All events entered in the Monte Carlo distributions are subjected to the complete real detector simulation described in chapter 3.

The selection criteria used do not distinguish the various background sources which contribute to the non-resonant background. In the following, the assumption
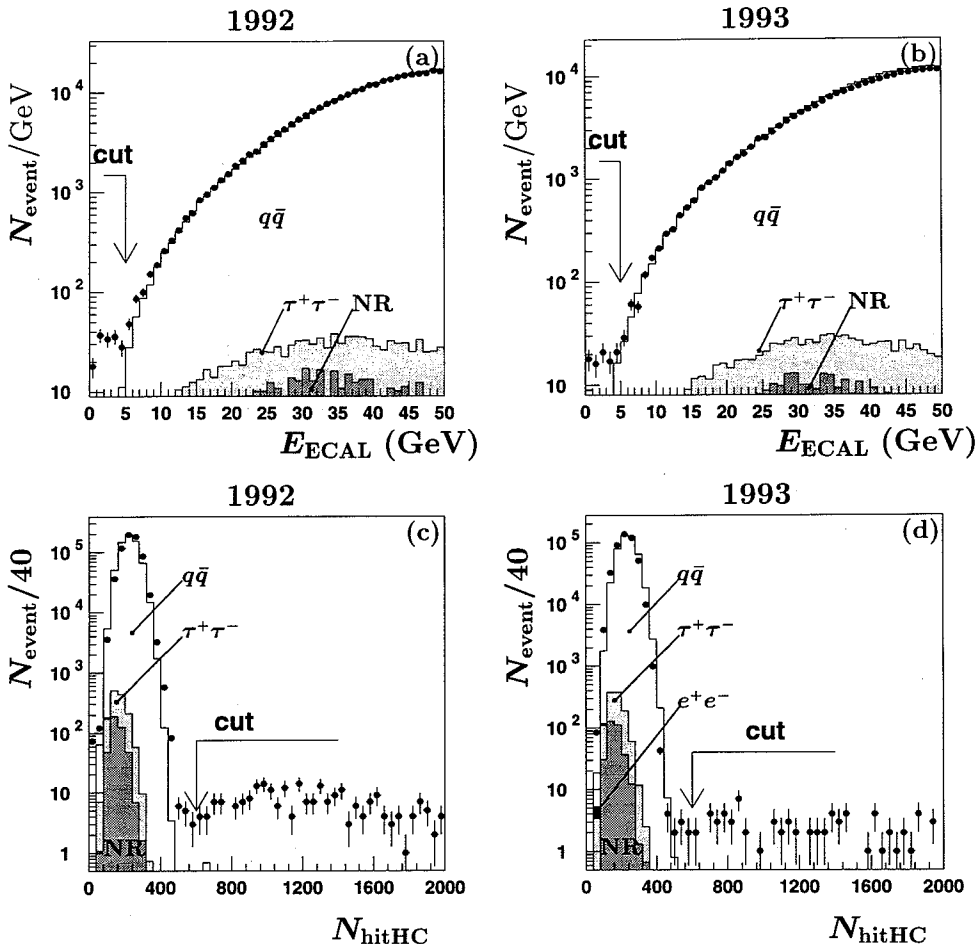
Figure 4.4: *The ECAL energy and HCAL hit multiplicity distributions for 1992 and 1993 peak data, compared with the Monte Carlo predictions. The definition of the symbols, shadings and normalisations are the same as for figure 4.1.*

is made that the distributions of the cut variables for beam-gas and beam-wall events are the same as for $e^+e^-q\bar{q}$ events. Therefore, the DIAG36 program is used for all histograms of the NR background. Consequences of this assumption will be discussed in chapter 5.

Most distributions show a good agreement between data and Monte Carlo, but discrepancies remain, although some of them are not directly relevant as they are located outside the acceptance regions. The Monte Carlo visible energy distributions

(figure 4.1) disagree in the region below the cut $E_{\mathrm{vis}}/\sqrt{s} = 0.5$. As will be explained in chapter 5, this discrepancy is related to the estimation of the non-resonant background.

The distributions of the number of ASRCs (figure 4.2) display discrepancies between data and Monte Carlo in the region below the cut and for events with very high multiplicity ($N_{\mathrm{ASRC}} > 70$). Differences at low multiplicities between 1992 and 1993 Monte Carlo predictions are due to the use of different Bhabha generator programs; for the region selected by the cut, these differences are negligible. The discrepancies in the high multiplicity region are partly understood to be due to an imperfect simulation of the interaction of charged pions in the HCAL material [7]. A visual scan confirms that the events in this region are all genuinely hadronic.

The transverse energy imbalance (figures 4.3(a) and (b)) shows discrepancies between data and Monte Carlo from the region $0.5 - 0.6$ GeV onwards. This effect is understood to be caused by cosmics and to a lesser extent by beam-wall and beam-gas background. The resulting small effect on the cross section is taken into account in the systematic error. The longitudinal energy imbalance (figures 4.3(c) and (d)) displays a good agreement between data and Monte Carlo over the whole range of $E_{\parallel}$.

Also the ECAL energy data distributions (figures 4.4(a) and (b)) agree well with the Monte Carlo distributions for the events retained. Below the cut the data are flatter than the Monte Carlo prediction because of the presence of HCAL noise. The agreement between N_{hitHC} (figures 4.4(c) and (d)) data and Monte Carlo can be qualified as adequate, in spite of a small peak shift (in opposite directions for 1992 and 1993). As this figure shows, the cut on the HCAL hit multiplicity is rather loose; there is still some noise present in the acceptance region. This will be taken into account as a background contribution.

4.1.3 Results

The hadron selection criteria are in principle imposed on all the events collected during the 1992 and 1993 running years. In reality about 1.4 million events were collected but not all the data recorded could be used. In 1992, a significant amount of events were lost because of computer communication problems during the event reconstruction. For some runs, both in 1992 and 1993, the conditions of the detector and/or the beams were of insufficient quality for the data to be usable. A run was marked "bad" if one or more of the following hardware problems were detected:

- low HCAL voltages or HCAL readout errors;
- "dead" ECAL rings;
- incorrectly calibrated HCAL components;
- excessive energy trigger or background rates;
- event readout timings not synchronous with the bunch crossing;
- luminosity measurement problems.

As a result of all the above effects about 1.3 million hadrons were selected for the cross section measurements in the period 1992-1993. A breakdown of the event samples for data and Monte Carlo are presented in table 4.1, together with the Monte Carlo efficiencies.

Period	Source	N_{event}	$\epsilon(\%)$
1992	Data	646,112	–
	MC $q\bar{q}$	937,124	99.220±0.009
	MC e^+e^-	30,000	≈0.007
	MC $\tau^+\tau^-$	251,784	3.19±0.04
	MC $e^+e^-q\bar{q}$	64,999	1.22±0.04
1993 Pre	Data	165,831	–
	MC $q\bar{q}$	405,148	99.270±0.013
	MC e^+e^-	115,250	≈0.004
	MC $\tau^+\tau^-$	68,982	3.69±0.07
	MC $e^+e^-q\bar{q}$	40,150	1.32±0.06
1993 P−2	Data	85,038	–
	MC $q\bar{q}$	260,676	99.199±0.017
	MC e^+e^-	214,992	≈0.003
	MC $\tau^+\tau^-$	58,998	3.58±0.08
	MC $e^+e^-q\bar{q}$	102,500	1.38±0.04
1993 P	Data	280,550	–
	MC $q\bar{q}$	704,251	99.261±0.010
	MC e^+e^-	200,500	≈0.004
	MC $\tau^+\tau^-$	120,011	3.69±0.05
	MC $e^+e^-q\bar{q}$	69,850	1.32±0.04
1993 P+2	Data	121,536	–
	MC $q\bar{q}$	226,840	99.227±0.018
	MC e^+e^-	216,000	≈0.004
	MC $\tau^+\tau^-$	46,444	3.74±0.09
	MC $e^+e^-q\bar{q}$	95,000	1.17±0.03

Table 4.1: *The 1992 and 1993 event samples and Monte Carlo hadron selection efficiencies used for the cross section measurements.*

4.2   Forward-Backward Hadron Selection

4.2.1   Selection Criteria

In order to obtain a $q\bar{q}$ sample with reliable and sufficient charge information, additional criteria are imposed on the hadron sample surviving the cross section criteria. These criteria can be split in two groups. The first group acts on the event level, whereas the second group selects "high" quality TEC tracks.

The first group consists of the following event criteria:

(1) a sphericity $S < 0.12$;

(2) a thrust axis in the range $|\cos\theta_{\mathrm{T}}| < 0.8$;

(3) a momentum for all charged particles below the beam energy $p < E_{\mathrm{beam}}$;

(4) a number of charged tracks in *each* hemisphere ≥ 3.

The cut on the sphericity suppresses events with hard gluon radiation; its purpose is to make the thrust axis agree better with the original quark directions. This cut is loose enough so as not to unduly suppress the fraction of the $b\bar{b}$ events compared to the fraction other $q\bar{q}$ events. The cut on the polar angle of the thrust axis is imposed because the TEC-information becomes less accurate in the very forward-backward regions[4]. The cut on the track momenta is applied to avoid poorly measured high momentum tracks. The cut on the number of tracks per hemisphere is related to the required amount of charge information (see chapter 6). Note that the hemispheres are defined by the plane perpendicular to the thrust axis.

The location of the sphericity cut is illustrated in figure 4.5, where hadron data are compared with the hadron Monte Carlo prediction. The distribution is made for all hadrons selected by the cross section criteria; a very good agreement between data and Monte Carlo is observed.

The application of the second group of criteria (those on the TEC track level) starts by subjecting all charged tracks to the TEC Monte Carlo real detector selection criteria enumerated and described in detail in section 3.2.2. Subsequently, in each hemisphere the tracks surviving this selection are ordered according to their momentum component $p_{\parallel}$ parallel with the thrust axis:

$$p_{\parallel} = |\vec{p} \cdot \hat{n}_T|, \tag{4.1}$$

with $\hat{n}_T$ as defined in 2.12.

Finally, the following requirements are imposed:

---

[4]Note that the chapter 3 track $\cos\theta$-cut is more or less consistent with the $\cos\theta_T$-cut made above. For a typical width of a jet cone (30°) only about 15% of the tracks belonging to an event with $|\cos\theta_T| = 0.8$ will spill over into the region above $|\cos\theta| = 0.9$.
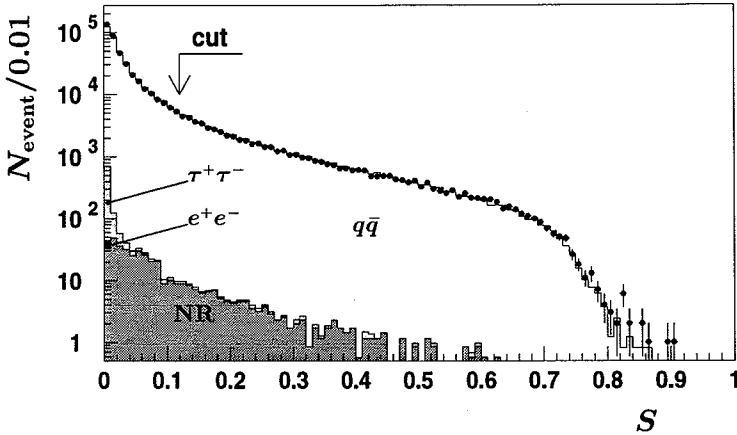
Figure 4.5: *The sphericity distribution for 1993 data. The dots represent the data, the histograms the Monte Carlo $q\bar{q}$ and background contributions. The Monte Carlo histogram is normalised to the number of accepted hadrons by the cross-section sample selection criteria. The definition of the symbols, shadings and normalisations are the same as for figure 4.1.*

(5) in *each* hemisphere, the *three leading $p_\parallel$* tracks, must be "good" tracks.

For a TEC-track to be "good", one requires:

(5a) a number of hits with $r\phi$-information $N_{\text{hit}}^{r\phi} \geq 20$ (see section 3.2.2);

(5b) a *charge confusion $CC < 10\%$* .

If one of the leading tracks is not "good", the event is rejected as a whole.

The charge confusion is a new variable related to the probability that the charge of the track is wrongly identified. It can be defined as:

$$CC[p_T, \sigma(p_T^{-1})] = \frac{1}{\sqrt{2\pi}} \int_{x=1/[p_T\sigma(p_T^{-1})]}^{\infty} \exp\left(-\frac{1}{2}x^2\right) dx, \qquad (4.2)$$

where p_T^{-1} is the inverse transverse momentum of the track (i.e. the quantity directly measured by the TEC) and $\sigma(p_T^{-1})$ its precision. This definition uses the error function as charge confusion estimator. For an increasing p_T but a fixed $\sigma(p_T^{-1})$, the lower limit x of the integral decreases and the charge confusion increases. For $p_T = \infty$, the track is a straight line: the lower limit of the integral becomes $x = 0$ and the charge confusion (appropriately) 50% .

The dependence of the charge confusion on the track charge information does not display a pronounced optimum; one therefore has a certain leeway in choosing the

CC cut-off value. A study of the track-fit χ^2/df-dependence on CC suggests that values of 5% to 15% are appropriate. For reasons of statistics – and as decreasing CC-cuts diminish the statistics – a compromise value was found to be in the vicinity of 10% . Retaining all tracks with a $CC < 10\%$ leads both to sufficient statistics and adequate rejection of leading tracks without sufficient charge information.

The distribution of the charge confusion is shown in figure 4.6. The agreement between data and Monte Carlo below the CC cut is adequate, but will nevertheless be the subject of further analysis in chapter 6. The sudden drop at $CC \approx 0.45$ is due to cut (3).
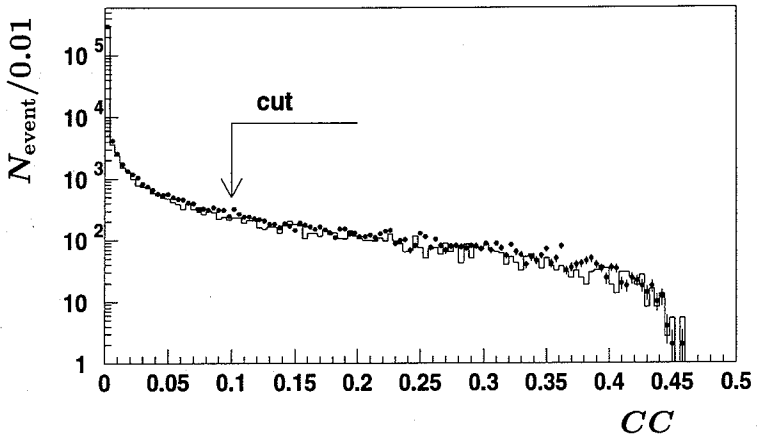
Figure 4.6: *The charge confusion distribution for the three leading tracks in each hemisphere. The dots represent the data, the histograms the Monte Carlo. The Monte Carlo histogram is normalised to the number of accepted hadrons after imposing all cuts.*

There is a relation between the CC-cut and the accepted transverse momentum region. Indeed, fixing $CC = 10\%$ implies a value for the lower limit of the integral in 4.2:

$$x = \frac{1}{p_T \sigma(p_T{}^{-1})} = 1.282, \tag{4.3}$$

hence $CC < 10\%$ implies $x > 1.282$, or, expressed in p_T:

$$p_T < p_T^{max} = \frac{1}{1.282 \cdot \sigma(p_T{}^{-1})}. \tag{4.4}$$

Note that although the CC (or the p_T^{max} variable) is only a function of $\sigma(p_T{}^{-1})$, the latter variable itself is a very complex function of the local azimuthal angle $\phi_{local}(=$

ϕ mod $\pi/6$), the polar angle of the track $|\cos\theta|$ and the number of hits remaining with accepted $r\phi$ information $N_{\text{hit}}^{r\phi(5)}$. Figure 4.7 illustrates this dependence by showing the three dimensional hyperplane $CC = 10\%$ in function of those variables for the barrel and endcap, respectively. In the barrel region, there is no dependence on $|\cos\theta|$, thus the plot only shows the dependence on N_{hit} and ϕ_{local}. In the endcap region, the dependence on $|\cos\theta|$ is strongly correlated with the N_{hit} dependence (see figure 3.5). In order to allow a three dimensional illustration, we can eliminate the N_{hit} dependence by fixing N_{hit} to its average value for the ϕ_{local} and $|\cos\theta|$ under consideration.

The effect of applying the ensemble of all cuts is illustrated by the plots in figure 4.8. Plot (a) shows the $|\cos\theta_T|$ distribution before the cuts; plot (b) the same distribution after all the cuts. The lines show the position of the $|\cos\theta_T|$-cut at 0.8. In both plots, the Monte Carlo events are in reasonably good agreement with the data, but there are some remaining discrepancies. In particular, there is a disagreement around $|\cos\theta_T| = 0.76$; this is traceable to the imperfect modelling of the gaps between the ECAL barrel and the endcaps. However, these discrepancies do not influence the forward-backward asymmetry since this quantity does not explicitly depend on absolute number of events in each $|\cos\theta_T|$ bin and the residual migration effects are small.

Figure 4.9 shows comparisons between data and Monte Carlo for the same track variables as shown in figures 3.11(b),(d),(f) and 3.12(b), now however restricted to the three leading tracks in each hemisphere. Most distributions display a good agreement between data and Monte Carlo. The discrepancies remaining are of the same type and appear at the same places as in the previous track distributions. The p_T-plot 4.9(a) shows that the average transverse momentum of the leading tracks is about 3 GeV. From distributions for each of the leading tracks separately, it is found that the combined DCA-p_T cuts, imposed to obtain tracks originating from the vertex (see chapter 3), preserve 99.9% , 99.7% and 98.7% of the first, second and third leading track respectively; i.e. numbers which are significantly larger than the 85% of overall tracks accepted by this cut (see chapter 3). Both the peaks of the DCA and N_{hit} distributions (plots 4.9(b) and 4.9(c), respectively) are narrower than those of the corresponding distributions given in chapter 3. The dips in the ϕ_{local} distribution 4.9(d) are more pronounced than in the similar plot of figure 3.11, since the leading tracks are more sensitive to the CC-cut than an average track.

---

[5]In fact, as a result of the dependence of d_{hit} on p_T (see figure 3.7), there is even a (small) dependence on p_T; as for d_{hit} this dependence will be neglected.
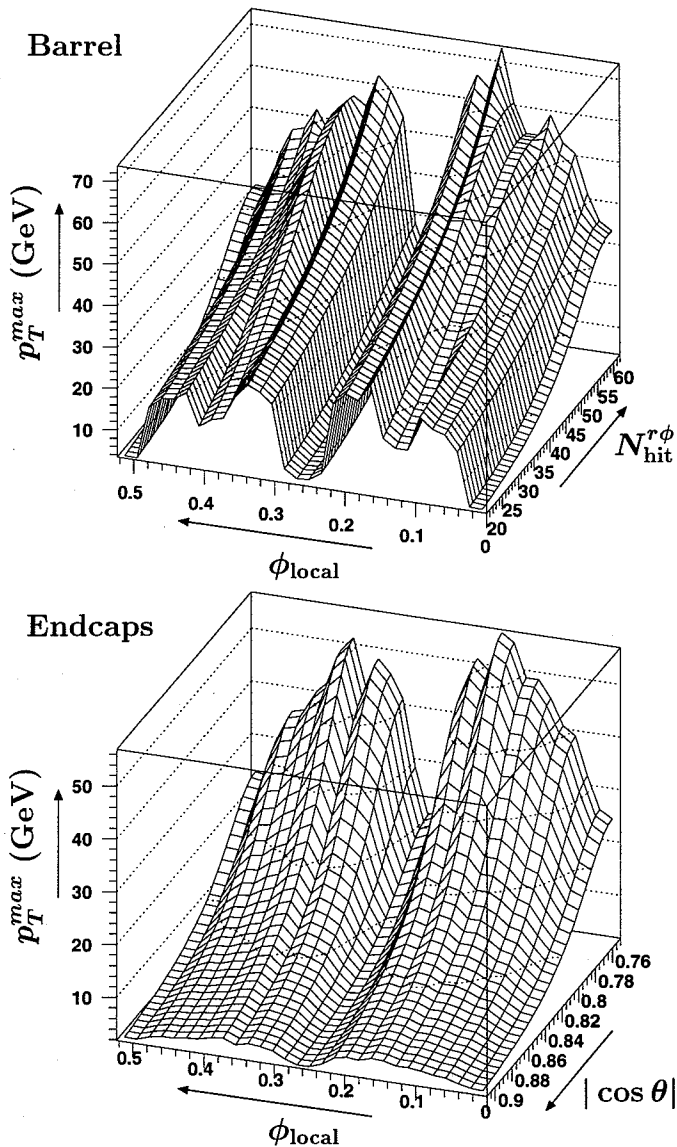
Figure 4.7: *The plane of constant charge confusion CC=10% in the barrel and endcap regions. Note that in the barrel region, there is no dependence on $|\cos\theta|$. In the endcap region, the $N_{\text{hit}}^{r\phi}$ dependence has been eliminated as explained in the text.*
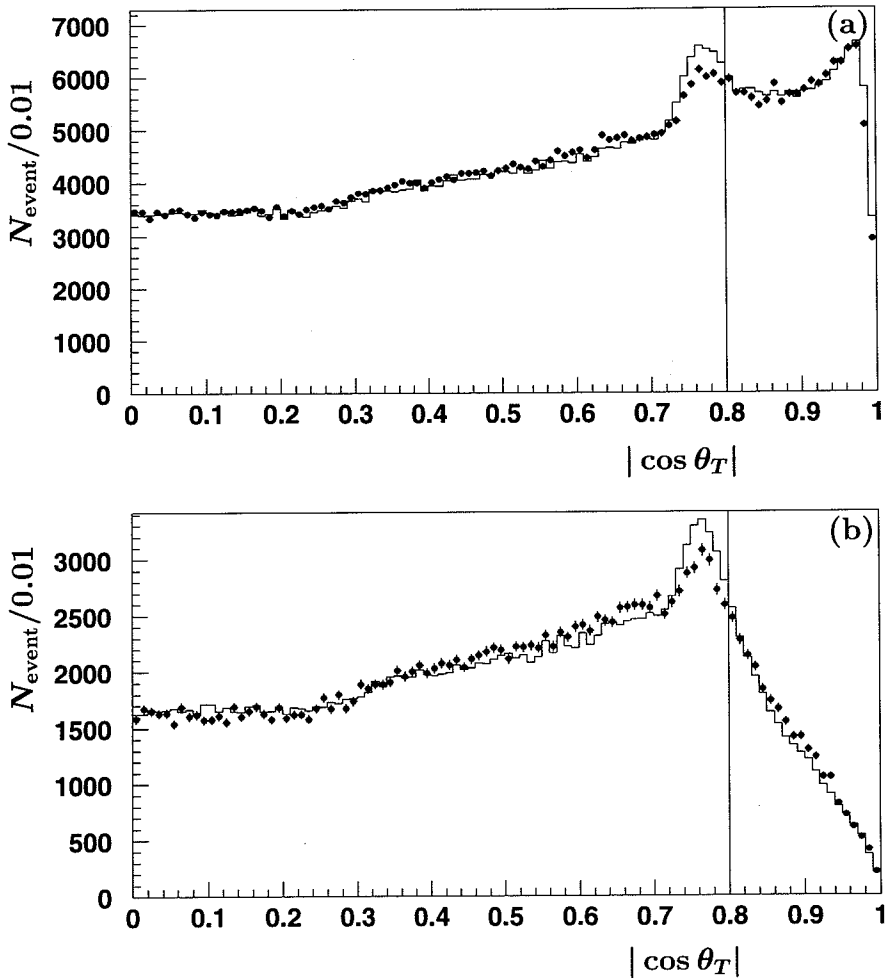
Figure 4.8: *Polar angle of the thrust axis distributions for 1993 data. Plot (a) is the thrust angle distribution before the forward-backward hadron selection; plot (b) after this selection. The Monte Carlo in plot (a) is normalised to the number of hadrons for the cross section measurements, in plot (b) to the number of hadrons after the forward-backward selection.*
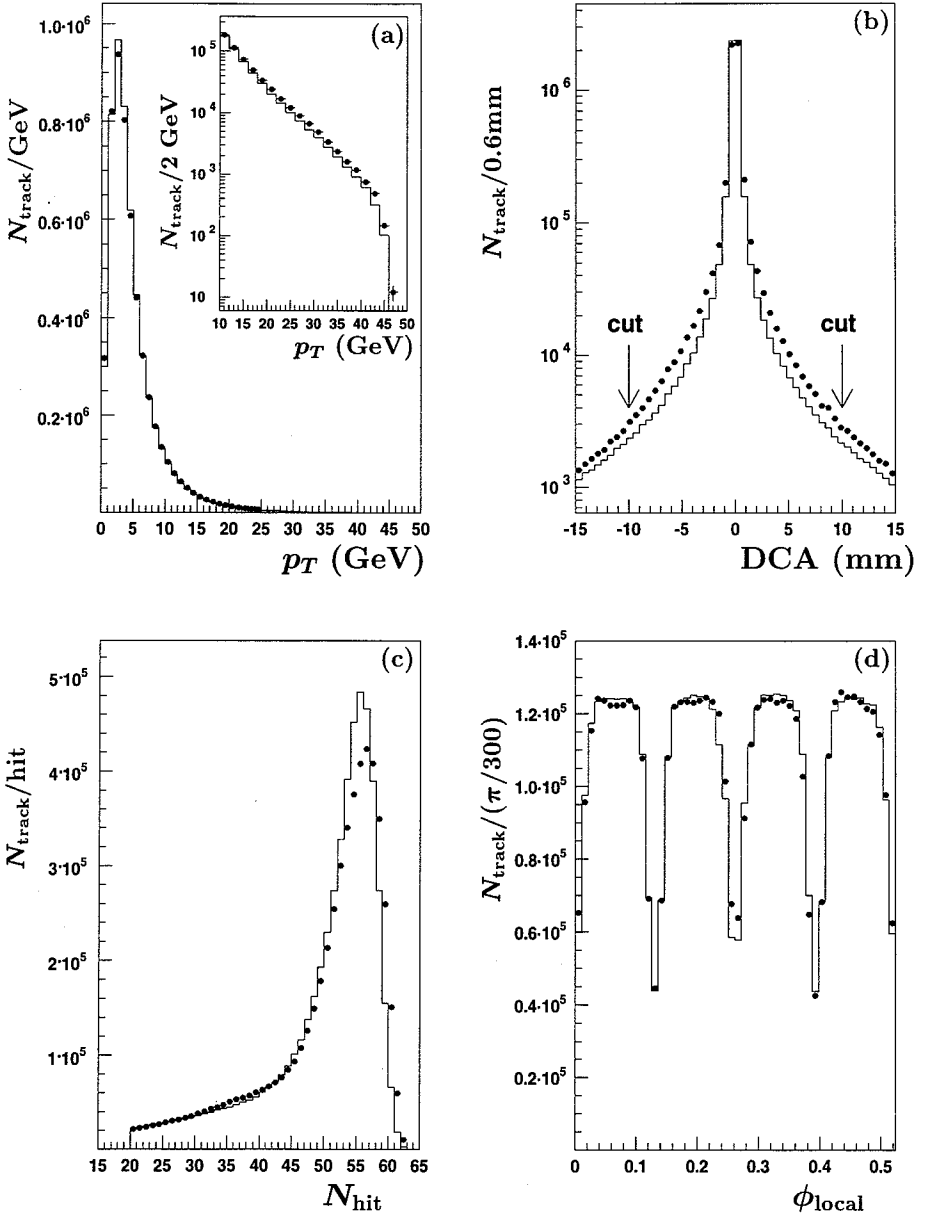
Figure 4.9: *Distributions of track parameters for the 3 leading tracks in each hemisphere. The insert in the p_T plot is a blow-up of the tail, i.e. the region $p_T > 10$ GeV. The dots represent the data; the histogram the Monte Carlo. The Monte Carlo plots are normalised to the number of accepted hadrons in the data.*

4.2.2 Results

The event statistics for the 1993 data and the Monte Carlo sample, after applying the ensemble of cuts are shown in table 4.2. A data sample of about 166,000 hadrons is obtained. Also shown are the percentages of data and Monte Carlo events surviving after each specific cut. Given the fact that errors on the fractions are statistical only, the agreement between the data and Monte Carlo percentages can be qualified as adequate. Note that this agreement can be considered a measure of the success of our smearing technique.

		Monte Carlo		Data	
	Cut	N_{events}	fraction(%)	N_{events}	fraction(%)
	N_{had}	1,584,910	–	652,986	–
(1)	$S < 0.12$	1,365,313	86.14±0.03	566,406	86.74±0.04
(2)	$|\cos\theta_T| < 0.8$	1,020,205	64.44±0.04	423,563	64.87±0.06
(3)	$p < E_{\text{beam}}$	655,648	41.37±0.04	279,182	42.75±0.06
(4)	$(3+3)$ tracks	619,648	39.10±0.04	265,141	40.60±0.06
(5)	$(3^* + 3^*)$ tracks	408,679	25.79±0.04	166,377	25.48±0.05

Table 4.2: *The 1993 event sample remaining after the application of the different forward-backward hadron sample selection criteria. The 3* indicates 3 leading tracks passing criteria (5a) and (5b) (see text).*

Comparing the event losses after each cut, one concludes that with respect to the sample remaining just prior to the cut, selection criteria (3) and (5) are the most severe ones. An alternative selection strategy, which would compensate for the event losses caused by criterion (5), would be to use the fourth (and fifth) track and retain the event if this (these) track(s) pass (5). The price to be paid however would be that one has to accept more events with tracks that contain significantly less quark information.

5

Cross Section Measurements

The decay of the Z is dominated by the hadronic channel; the decay probability for $Z \rightarrow q\bar{q}$ is approximately seven times larger than the one for $Z \rightarrow l\bar{l}$. Thus, the hadronic channel provides large statistics and its cross section can be measured precisely. On the other hand, again as a result of this large statistics, many systematic effects become significant and have to be carefully taken into account.

In the following, the calculation of the hadronic cross section is reviewed. The sources of systematic errors are discussed, and the necessary corrections applied. In the last sections, the results are listed for the 1992 and 1993 data taking periods. Our analysis and results can be considered a continuation of the thesis of F. Filthaut in which the measurements for 1990 and 1991 were presented [7].

5.1   Hadron Cross Section Determination

In principle a cross section is measured by the ratio:

$$\sigma = \frac{N_{\text{event}}}{\int \mathcal{L}dt},$$
(5.1)

where N_{event} equals the total number of events produced in a certain period of time and $\int \mathcal{L}dt$ the time-integrated luminosity for that same period.

As discussed in section 4.1.1, in practice one has to distinguish the signal from background processes. This is the purpose of the selection criteria. Such criteria are however never perfect. The number of selected events thus becomes a linear combination of σ_S and σ_B, the cross sections of the signal and background channels respectively, with coefficients depending on the various selection efficiencies involved. Specifically for the hadron channel $\gamma/Z \rightarrow q\bar{q}$, the net consequence is a replacement

of equation 5.1 by:

$$\sigma_{\mathrm{h}} = C_E \cdot \frac{\left(N_{\mathrm{event}} - N_{\mathrm{noise}}^{\mathrm{HCAL}}\right)}{\varepsilon_t \varepsilon_{\mathrm{h}} \cdot \int \mathcal{L}dt} - \frac{1}{\varepsilon_t \varepsilon_{\mathrm{h}}} \cdot \left(\varepsilon_{\mathrm{NR}} \cdot \sigma_{\mathrm{NR}} + \varepsilon_{\tau\tau} \cdot \sigma_{\tau\tau} + \varepsilon_{\mathrm{ee}} \cdot \sigma_{\mathrm{ee}}\right), \qquad (5.2)$$

where C_E is the correction factor arising from the beam energy spread, ε_t the hadronic trigger efficiency and $N_{\mathrm{noise}}^{\mathrm{HCAL}}$ the number of HCAL noise background events; σ_{NR}, $\sigma_{\tau\tau}$, σ_{ee} are the cross sections and $\varepsilon_{\mathrm{NR}}$, $\varepsilon_{\tau\tau}$, $\varepsilon_{\mathrm{ee}}$ the efficiencies of the various background channels involved. Note that effects of the beam spread on the background sources themselves are assumed to be negligible.

From equation 5.2 it follows that twelve quantities have to be determined in order to arrive at the hadronic cross section. Nearly all these quantities are sensitive to the detector conditions. As explained in chapter 2, the luminosity is measured using the small-angle Bhabha process. The results of the luminosity measurements for the runs selected are given in table 5.1. On average, the 1992 data sample has a 0.6% and the 1993 data sample a 0.15% luminosity error [6, 29]. The substantially smaller 1993 error reflects the improvements made possible by the SLUM detector. The hadron

Period	$\int \mathcal{L}dt(\mathrm{nb}^{-1})$	N_{events}	$\varepsilon_{\mathrm{h}}(\%)$
1992	21,359±22±128	646,112	99.220±0.009
1993 Pre	5,459± 9± 8	165,831	99.270±0.013
1993 P−2	8,502±11±13	85,038	99.199±0.017
1993 P	9,350±12±14	280,550	99.261±0.010
1993 P+2	8,806±11±13	121,536	99.227±0.018

Table 5.1: *Luminosities of the accepted runs and the corresponding number of selected hadron events and selection efficiencies for the various running periods. The first error on the luminosity is statistical, the second systematic.*

selection efficiencies for the various channels are derived from the corresponding Monte Carlo events; they were already listed in table 4.1. For completeness, the numbers of selected $q\bar{q}$ events and the corresponding Monte Carlo efficiencies are repeated in table 5.1.

5.2   Background Contributions

The background contributions of the leptonic channels can be derived from their experimentally measured cross sections and their Monte Carlo determined acceptances. The errors on these contributions then must take into account the limited Monte Carlo statistics and the cross section uncertainties. The $\tau^+\tau^-$ background

5.2. Background Contributions

is calculated this way. For the Bhabha cross section, due to the lack of reliable L3 endcap cross section measurements, the theoretically calculated cross sections are preferred (see section 4.1.2).

The background contribution N_{noise}^{HCAL} is obtained from a straight line fit to the N_{hitHC} distribution in a range 500 to N_{max}, with N_{max} ranging between 1000-1500. Subsequently, an extrapolation is performed to the region $N_{hitHC} < 500$. The integral of the fitted line in the range $0 < N_{hitHC} < 600$ then leads to an estimate for the electronic noise background contribution in the acceptance region and the error on this quantity to a corresponding systematic error.

The background contributions obtained are given in table 5.2. For a typical $q\bar{q}$ sample of about one million events and a peak cross section of approximately 30 nb, one expects a statistical error of about 30 pb. Thus, the $\tau^+\tau^-$ contribution is of the order of the statistical error. The Bhabhas constitute an extremely low background; in the distribution of N_{ASRC}, background Bhabhas are only clearly visible below the cut value. The HCAL noise background is one order of magnitude smaller than the expected statistical error.

Period	$\varepsilon_{e^+e^-} \cdot \sigma_{e^+e^-}$ (pb)	$\varepsilon_{\tau^+\tau^-} \cdot \sigma_{\tau^+\tau^-}$ (pb)	N_{noise}^{HCAL}
1992	0.45±0.31	46.5±1.0	54±11
1993 Pre	0.82±0.21	54.4±1.1	11.3±2.9
1993 P−2	0.56±0.22	18.1±0.6	18.7±3.5
1993 P	0.82±0.21	54.4±1.1	25.3±4.1
1993 P+2	0.72±0.24	25.6±0.7	18.7±3.5

Table 5.2: *Background contributions from the channels e^+e^-, $\tau^+\tau^-$ and from the HCAL noise.*

The non-resonant background cross section σ_{NR} is rather difficult to deter since the two photon background, just using calorimetric information and wi using additional assumptions, cannot be distinguished from beam-gas and beam background, and because the individual cross sections of the non-resonant pro are not known. Estimates of these contributions can be made using three me all based on the distributions of E_{vis} and $E_{\parallel}$. The first and the second meth performed under the assumption made in chapter 4 that all cut variable distri for the beam-gas and beam-wall events are the same as for the two photon The third method does not use this assumption and is only used as a chec first and the second method.

The first method is based on the visible energy distribution: an expor is made to the data in the low energy region $0.15 \lesssim E_{vis}/\sqrt{s} \lesssim 0.4$, afte tion of the Monte Carlo hadron, tau and Bhabha contributions. The r

Comparing the results of the non-resonant background determinations from the first and second method, one observes results compatible for the 1993 P and 1993 P+2 running periods, but different for the 1992, 1993 Pre and 1993 P−2 runs. For the first group of periods we can therefore evaluate an error-weighted average; for 1993 Pre and P we calculate an unweighted average and use half the difference as an estimate of the error on this average. The results thus obtained are shown in table 5.5. They are consistent with the upper limits derived using the third method. As the effective non-resonant cross sections σ_{NR} all agree with each other, the validity of the assumption that the this background is independent of the period and energy is confirmed.

Period	$\varepsilon_{NR} \cdot \sigma_{NR}$(pb)		σ_{NR}(nb)
1992	21.8±	7.4	1.8±0.6
1993 Pre	35±	20	2.7±1.5
1993 P−2	15.6±	3.4	1.13±0.25
1993 P	13.7±	1.0	1.04±0.08
1993 P+2	11.7±	1.0	1.00±0.09

Table 5.5: *Averaged non-resonant background contributions from the first and second method together with their errors.*

5.3 Cross Section Corrections

In the previous section we discussed all the background sources influencing the cross section. In this section we study the remaining factors, namely the beam energy spreads C_E and the trigger efficiencies ε_t, which are additional effects and are treated as corrections to the cross section[2].

5.3.1 Beam Energy Spread

The fact that the energy of all electrons (positrons) in each bunch is not exactly the same, results in the cross section measurements not being made at a single energy point. One actually measures an average over energies in a small region around this point, given by the spread in the beam energy. The cross sections can be corrected

---

[2]In principle there could also have been a correction to the cross section due to the fact that some of the JETSET hadronisation parameters were set at an incorrect value during the Monte Carlo generation. This error does lead to a small correction on the forward-backward charge asymmetry evaluation (see chapter 6), but has no measurable effect on the cross section determinations.

for this effect by convoluting the theoretically known cross section behaviour with the measured energy spread. In practice, only the spread correction on the hadronic channel has to be considered, since the corrections on the background channels turn out to have a negligible influence on the $q\bar{q}$ cross section.

The beam spreads for 1992 and 1993 and the corresponding cross section corrections obtained are given in table 5.6. The corrections are positive for the peak points, where the theoretical curve is concave, and negative for the off-peak points, where the theoretical curve is convex.

Period	Beam spread (MeV)	$\Delta\sigma/\sigma(\text{‰})$
1992	51±3	+1.40±0.16
1993 Pre	55.4±1.0	+1.62±0.06
1993 P−2	54.6±1.0	−1.04±0.04
1993 P	55.4±1.0	+1.67±0.06
1993 P+2	55.6±1.0	−0.60±0.05

Table 5.6: *Corrections to the total hadronic cross section due to the beam energy spread.*

5.3.2 Trigger Efficiencies

The best way to estimate a trigger efficiency would be by means of a complete real detector trigger simulation. However the possibility of such a simulation was not available for the present analysis. For the hadron sample, an estimation of the level 1 trigger inefficiencies is possible using the data themselves [7], exploiting the redundancy of the relevant subtriggers and assuming that the subtrigger data are statistically independent. For the hadrons, the relevant subtriggers are the energy, the scintillator and the TEC trigger. The number of events is counted which are triggered by each subtrigger or a combination thereof. A likelihood fit to these numbers then yields the overall trigger (in)efficiency for the combined subdetector information as well as the different subtrigger (in)efficiencies. The method crucially depends on the assumption that the subtriggers are statistically independent, which is however a priori not unreasonable since the signals come from different subdetectors.

Because of the detector geometry, the trigger efficiencies are dependent on the polar angle of the thrust axis. Thus the above technique must be applied for each $|\cos\theta_T|$ bin separately. For the 1993 hadron sample, the results for the combined level 1 trigger efficiency and its different subtriggers are shown as a function of $|\cos\theta_T|$ in figure 5.2; the 1992 inefficiencies display an analogous behaviour.
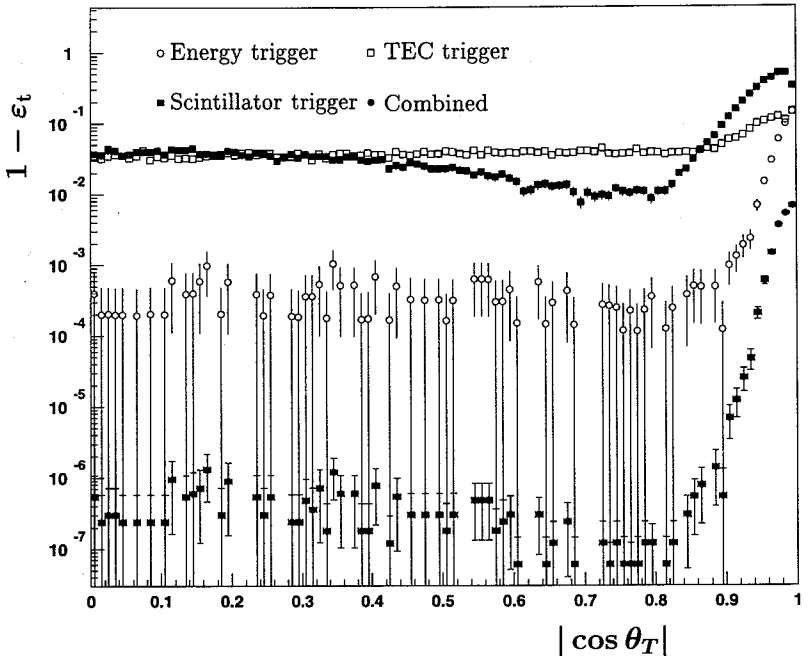
Figure 5.2: *Level 1 inefficiencies for the 1993 hadron sample as a function of the polar angle of the thrust axis.*

All trigger efficiencies show significant drops in the very forward and backward regions, i.e. above $|\cos\theta| > 0.94$. In particular, the energy trigger efficiency drops because of the limited endcap coverage, whereas the scintillator efficiency drops because for the data used in this analysis, no forward-backward scintillators were installed. The TEC trigger efficiency remains however more uniform, because of the larger angular coverage of this subdetector[3]. As a result, the total inefficiency is negligible in the regions $|\cos\theta| < 0.94$ for both 1992 and 1993 and equal to $(0.25\pm0.03)\%$ and $(0.29\pm0.03)\%$ in the very forward-backward regions for 1992 and 1993, respectively.

The corrections to the cross section are obtained by means of event-reweighting per $|\cos\theta_T|$-bin; on average they amount to $\Delta\sigma/\sigma = (+0.17 \pm 0.02)\%$ and $\Delta\sigma/\sigma = (+0.19 \pm 0.02)\%$ for 1992 and 1993, respectively.

The assumption that all subtriggers are statistically independent is tested by

---

[3]Note that this fact does not contradict the argument given in chapter 4 that a selection based on TEC information would not be sufficiently accurate. To use such a selection one would need to define *good quality* tracks, which would again lead to an angular coverage limited to the barrel region.

making distributions for each subtrigger under all yes/no conditions for the other subtriggers. No significant differences are observed between these distributions.

A determination of the level 2 inefficiency can be made using the one-out-of-ten events which are rejected by level 2 but are passed to level 3 anyway (see chapter 2). In the accepted hadron sample, about 100 of such events were found for both 1992 and 1993 and the number of level-2-missed hadron events is therefore about 900. It has been verified from an event scan that these 100 events are genuine $q\bar{q}$ decays; only a few of them appear to be cosmics. Furthermore, their selection variable distributions are similar to the ones shown in chapter 4, except for the visible energy which has a somewhat lower average. The major fraction of these events are in the forward and backward regions. The cross section corrections obtained for the different running periods are shown in table 5.7.

Period	$\Delta\sigma/\sigma(\permil)$
1992	1.48±0.14
1993 Pre	1.34±0.27
1993 P−2	1.69±0.42
1993 P	1.26±0.20
1993 P+2	1.70±0.36

Table 5.7: *Corrections to the cross section due to trigger level 2 inefficiencies.*

5.4 Systematic Errors

Sources of systematic errors are the uncertainties on all the quantities used in equation 5.2 which transform N_{event} into a cross section. The systematic errors resulting from these quantities are:

- the luminosity errors listed in table 5.1;

- the $q\bar{q}$ acceptance errors resulting from the limited hadron Monte Carlo statistics and summarised in table 4.1;

- the errors on the lepton background contributions due to the limited background Monte Carlo and, for the taus, the experimental errors on the cross sections and displayed in table 5.2;

- the errors on the non-resonant background contributions resulting from the uncertainties on its determination and presented in table 5.5;

- the errors on the HCAL noise contributions given in table 5.2;

- the errors of the beam energy spread corrections listed in table 5.6;

- the errors of the trigger inefficiencies given in section 5.3.2.

In addition to the above sources, two other ones can lead to systematic errors on the hadronic cross section: the uncertainties in the event selection procedures and the variations of the detector performance with time. They are discussed in more detail in sections 5.4.1 and 5.4.2.

There is in principle a third source which could contribute to the systematic errors: the deficiencies in the detector simulation. It turns out however that the main elements in this simulation (i.e. the inefficient crystals and/or rings and the noisy crystals) are described with negligible systematic error consequences as a result of the accuracy with which they are described by the data-base information [42].

Other sources of systematic error one could consider to be contributing are the choices made in the theoretical description of the process $q\bar{q} \rightarrow$ hadrons (e.g. the choice of the Parton Shower model for the fragmentation and the string model for the hadronisation, and the parameter choices made within the framework of these models). The standard way to examine such model dependencies is to calculate the prediction of alternative models. At the present moment and for the specific goal considered here (a cross section determination at the permille level) there are no satisfactory alternatives available however. The standard alternative for the fragmentation phase (the Matrix Element model) suffers from its limitation to just four final state partons; the HERWIG cluster fragmentation model alternative [43] for the hadronisation phase lacks adequately tuned parameters. As for the possible effects resulting from choices of the parameters in the JETSET (Parton Shower and string) model, here the required standard procedure (variation of the parameters on the generator level and repeating the simulation on the detector level for each parameter variation individually) is such a computing-time consuming task that it is in practice impossible. The often used "trick" of just calculating the consequences of the parameter variations on the generator level and assuming that the observed differences are also representative for those occurring on the detector level cannot be used here as for some of the very crucial selection variables (e.g. $E_\perp$ and $E_\parallel$) the distributions on the generator level are significantly different from those on the detector level[4].

---

[4]The "trick" will/can be used later on for the calculation of the forward-backward charge asymmetry errors (see chapter 6) as the selection variables involved there do not display the generator-detector level discrepancies referred to above.

5.4.1   Event Selection Errors

The effective position of a nominal cut on a variable in the selection of the hadrons is related to the precision with which this variable is measured. A standard method to investigate systematic errors related to the choice of the cut positions, is to change each cut within plus and minus one sigma of its precision keeping all other cuts fixed and to evaluate the effect on the cross section. For each variation performed this way, the presence of a significant systematic error is established using a standard χ^2-test for a horizontal line going through the central value. If the probability of this "fit" is less than 5%, a systematic error is assumed to be indeed present and its size derived from a (sloped) linear or a parabolic fit through the central value of the set of cross sections. Using the fitted function, the cross sections at the borders of the range and the corresponding absolute differences with the central value are evaluated. The systematic error is then found as the quadratic sum of average of these absolute differences and the (additional) variation of the cross section resulting from the errors on the fit parameters.

The range used for the number of ASRCs follows from the criteria used in the grouping of hits into primitive objects and in the matching procedure to arrive at ASRCs. From these procedures, an error on the number of N_{ASRC} of ≈ 2 appears reasonable.

In order to estimate the ranges for the energy cuts, the error on N_{ASRC} is combined with the error on the average ASRC energy. From distributions of the ECAL and HCAL energy, it follows that for a typical $q\bar{q}$ event, the total visible energy is deposited for about 60% in the ECAL and for about 40% in the HCAL. The average number of ECAL and HCAL clusters is about 40 and 5, respectively. Using these numbers the average cluster energies are estimated to be (1.25 ± 0.03) GeV and (7.0 ± 1.8) GeV for the ECAL and HCAL, respectively, where the errors are calculated using expressions 2.2 and 2.3. Substituting these average numbers in equations 2.8, 2.11 and 2.10, the ranges for the low visible energy and the energy imbalances cuts are found to be nearly equal and approximately ± 0.1; the range of the high visible energy cut is approximately ± 0.25.

No systematic errors arise from the cut on the ECAL energy. At an ECAL energy of 5 GeV, the range for the cut to be varied within is too small to lead to effects visible in the systematic error. The systematic error due to the HCAL noise background subtraction is already presented in table 5.2.

Figure 5.3 shows the relative variations of the cross section for the 1993 P period, as a function of the cut positions; table 5.8 gives a complete overview for all periods. For most periods, the systematic errors from the minimum visible energy cut and the transverse energy imbalance yield the most important contributions.
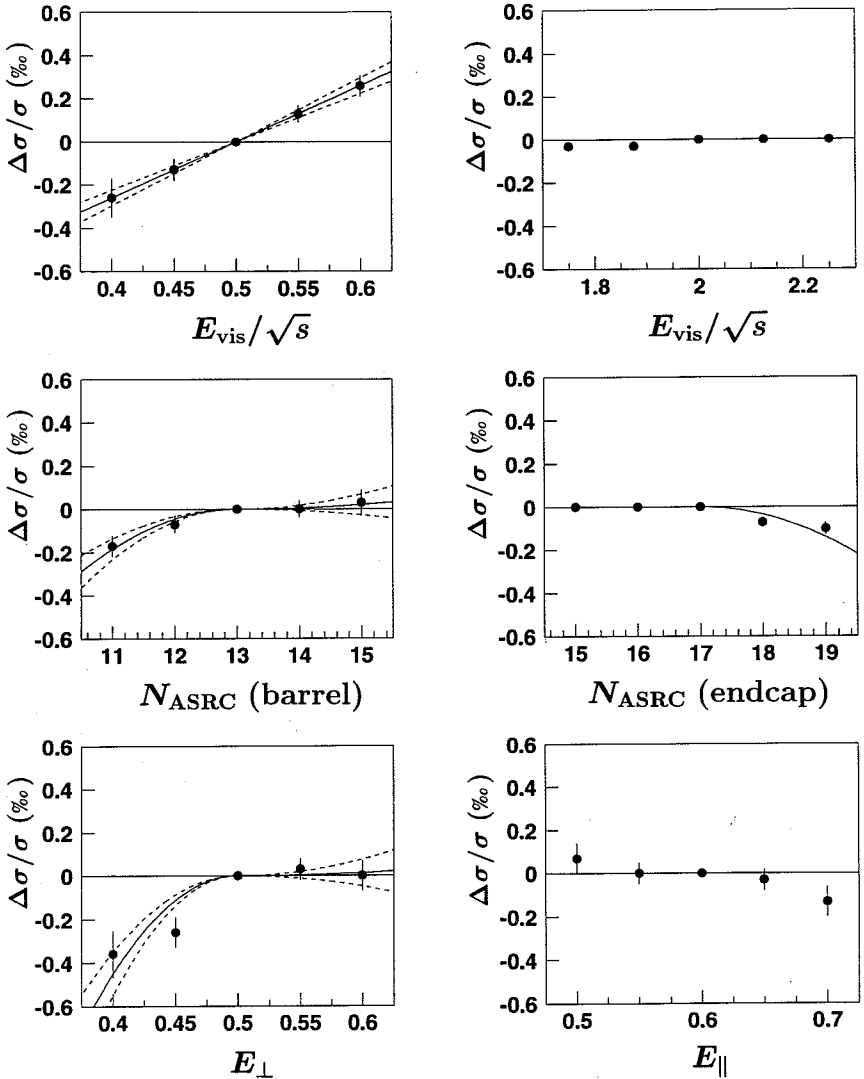
Figure 5.3: *The relative cross section variations as a function of the cut position for the 1993 P period. Also the fitted functions are drawn; the dashed curves indicate the errors on the fitted functions. For the high-E_{vis} cut and the N_{ASRC} cut in the endcap, the errors on the fitted function are too small to be visible.*

	1992	1993			
Cut	P	Pre	P−2	P	P+2
E_{vis}-low	0.4‰	0.6‰	0.4‰	0.3‰	0.5‰
E_{vis}-high	—	—	—	—	0.1‰
$E_\perp$	0.1‰	0.1‰	0.5‰	0.3‰	0.3‰
$E_\parallel$	0.1‰	0.1‰	0.2‰	—	0.3‰
N_{ASRC} barrel	0.1‰	—	0.1‰	0.2‰	—
N_{ASRC} endcap	—	—	0.2‰	—	—
Total	0.4‰	0.6‰	0.7‰	0.5‰	0.7‰

Table 5.8: *Systematic errors resulting from the event selection. Errors smaller than 0.05‰ (i.e. negligible errors) are indicated by −.*

5.4.2 Fill-to-Fill Variations

Changes with time of the performance of the detector are checked by tracking the time dependence of the cross section. For each fill, the cross section $\sigma \pm \Delta\sigma$ is calculated from the number of events and the corresponding luminosity, and divided by an average cross section σ_{av} for the period to which the fill belongs. Figure 5.4 shows the 1993 $\sigma/\sigma_{\mathrm{av}}$ dependence on the fill number.
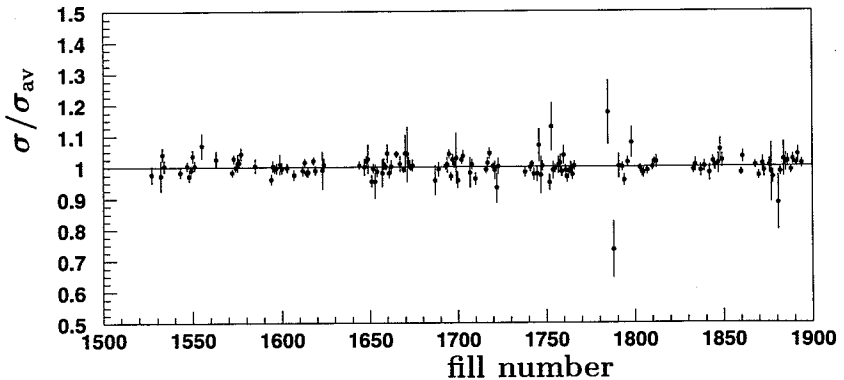
Figure 5.4: *Dependence of the scaled total cross section on the fill number for 1993 data.*

These fill values are subsequently combined into four cross sections, each of which corresponds to approximately one quarter period of 1992 or 1993. Figures 5.5(a) and (b) display the variation of these combined cross sections as a function of the period for 1992 and 1993, respectively. At the 95% CL no significant dependence on time is observed.
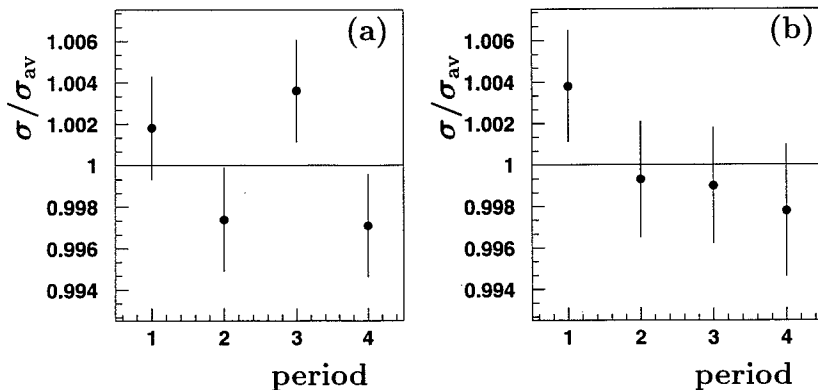
Figure 5.5: *Variation of the scaled total cross section for four 1992 and 1993 periods.*

5.4.3   Summary of Systematic Errors

The systematic errors are summarised in table 5.9. From period to period, the errors on the hadron acceptances and the errors on the Bhabha and $\tau^+\tau^-$ backgrounds are uncorrelated, since they are determined using separate Monte Carlo samples; all other errors however, although statistically independent, are 100% correlated. Note also that the luminosity and beam spread errors are 100% correlated with the corresponding errors for the other $f\bar{f}$ final state cross section measurements.

For all periods, the total systematic error is dominated by the luminosity error. Among the hadronic sources, the event selection yields the dominant error. Errors due to e^+e^- background, the level 1 inefficiencies and electronics noise are negligible. The non-resonant background systematic error changes significantly from period to period, because the methods to determine this background only yield consistent results for the 1993 P and P+2 periods.

5.5   Results

The number of events and the acceptances listed in table 4.1 and the luminosities listed in table 5.1 are substituted in equation 5.2 to yield the cross section values.

	1992	1993			
Source	P	Pre	P−2	P	P+2
Luminosity (stat)	1.0‰	1.6‰	1.3‰	1.2‰	1.3‰
Luminosity (sys)	6‰	1.5‰	1.5‰	1.5‰	1.5‰
Beam energy spread	0.2‰	0.1‰	−	0.1‰	0.1‰
SUBTOTAL	6.1‰	2.2‰	2.0‰	1.9‰	2.0‰
$q\bar{q}$ acceptance	0.1‰	0.1‰	0.2‰	0.1‰	0.2‰
e^+e^- background	−	−	−	−	−
$\tau^+\tau^-$ background	−	−	0.1‰	−	0.1‰
NR background	0.2‰	0.6‰	0.3‰	−	0.1‰
Electronics noise	−	−	0.1‰	−	−
Level 1 inefficiency	−	−	−	−	−
Level 2 inefficiency	0.1‰	0.3‰	0.4‰	0.2‰	0.4‰
Event selection	0.4‰	0.6‰	0.7‰	0.5‰	0.7‰
SUBTOTAL	0.5‰	0.9‰	0.9‰	0.5‰	0.8‰
TOTAL	6.1‰	2.4‰	2.2‰	2.0‰	2.1‰

Table 5.9: *Summary of the systematic errors contributing to the total cross section measurements. All errors smaller than 0.05‰ (i.e. negligible errors) are denoted by −.*

Before substitution, the number of events is corrected for the beam spread and the level 1 and 2 inefficiencies. Also the background contributions listed in tables 5.2 and 5.5 are taken into account. The total cross sections with their statistical and total systematic errors thus obtained are presented in table 5.10.

Period	$\sqrt{s}$ (GeV)	σ_h (nb)
1992	91.294	30.516±0.038±0.186
1993 Prescan	91.319	30.596±0.075±0.073
1993 P−2	89.448	10.053±0.034±0.022
1993 P	91.204	30.247±0.057±0.060
1993 P+2	93.031	13.884±0.040±0.030

Table 5.10: *Total $e^+e^- \to \gamma/Z \to q\bar{q}$ cross sections σ_h. The first error quoted is statistical, the second systematic.*

6

Forward-Backward Charge Asymmetry Measurements

The sample obtained after the forward-backward hadron selection was presented in chapter 4. This chapter discusses how this information is converted into a measurement of the forward-backward hadron charge asymmetry. The elements of the method required to achieve this are discussed together with the sources leading to systematic corrections and errors.

6.1 Method of the Measurement

The task at hand is a measurement of $A^{ch}_{\mathrm{FB,h}}$ as defined in equation 1.21. Rather than trying to establish the forward-backward nature of the event on an event-by-event basis (which – see appendix B – in our case would be next to impossible anyway) we will revert to a weighting method which directly leads to a statistically averaged charge asymmetry measurement. The method was used for the first time by the JADE experiment [44] and later by the OPAL experiment [45]. The properties and merits of the weighting method vis-a-vis the event-by-event method (or cuts-method) and the in principle statistically most powerful method, the maximum likelihood technique, were discussed by R. Barlow [46] and are (shortly) reviewed in appendix B[1].

In the weighting method, each event is assigned a weight w^F, representing the probability that the event is forward. As defined in the end of section 1.2, a forward event is an event in which a negatively charged quark is produced in the hemisphere defined by the incident *electron*. The event weight is determined using a function

---

[1] Also the $< Q_{\mathrm{FB}} >$ method, mentioned in footnote 2 of chapter 1, uses an averaging technique which can be considered as a special case of the weighting method, albeit one which does not explicitly use its probabilistic features.

which depends on variables containing event charge information. For the present analysis, variables are used related to the *three* leading "good" tracks resulting from the selection and ordering scheme described in chapter 4. For each of these leading tracks, a variable z_i is defined:

$$z_i = q_i \frac{p_{\|,i}}{E_{\text{beam}}}, \qquad (6.1)$$

where q_i is the charge of the i-th track, $p_{\|,i}$ its momentum component parallel to the event thrust axis (see equation 4.1) and E_{beam} the beam energy [2]. The situation is schematically depicted in figure 6.1. The use of three tracks per hemisphere
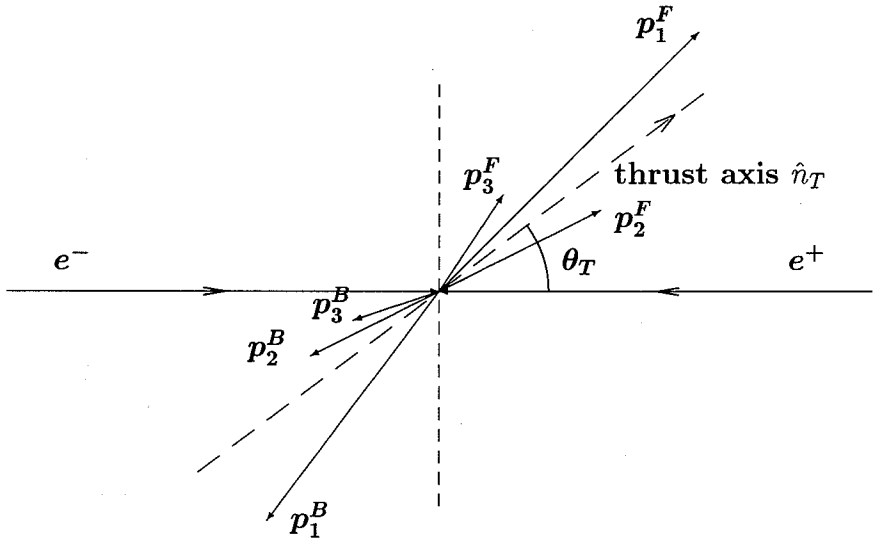
Figure 6.1: *Schematic view of the three leading tracks in each thrust axis hemisphere, used for the forward-backward charge asymmetry measurement.*

is a compromise between statistics and charge information content. Reducing the number of leading tracks to only two results in a loss of charge information which is not compensated by the slight improvement in statistics. The fourth and fifth leading track still contain some residual charge information, but requiring four, respectively five "good" tracks in each hemisphere would significantly reduce the size of our data sample.

---

[2] As in the OPAL-analysis we have also examined the result of just using $z = q$. Quite generally this leads to inferior results, in particular to higher statistical errors.

Distributions of the z_i variables both for measured and for Monte Carlo data are shown in figure 6.2. For each z_i variable, the distributions in the forward and
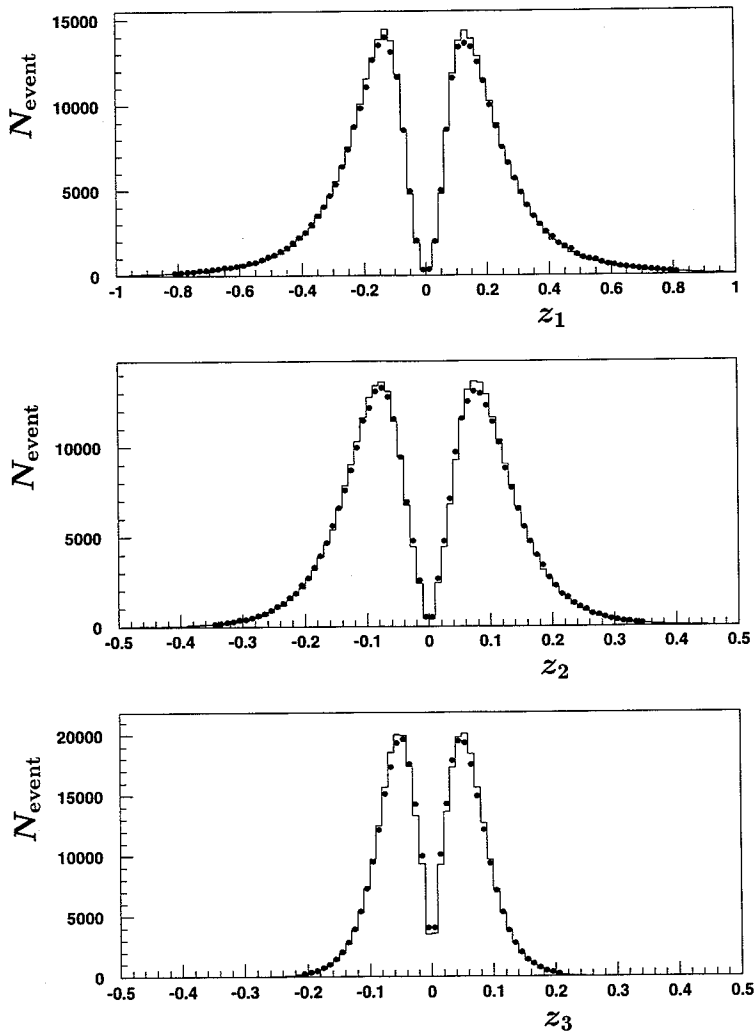
Figure 6.2: *Distributions of the z variables for the three leading tracks. Dots represent the data; the histogram the Monte Carlo. The Monte Carlo distributions are normalised to the number of hadrons in the data. Note the horizontal scale differences between the z_1-plot and the z_2,z_3-plots.*

backward hemisphere with respect to the thrust axis are added. Thus the positive z_i region contains all the *positively* charged tracks irrespective of the fact whether they are in the forward or backward thrust axis hemisphere, while the negative z_i region contains all the *negatively* charged tracks again irrespective of their being forward or backward. A rather good agreement is observed in all z_i distributions.

Using formula 6.1 and the three leading tracks, we obtain a set of three z_i variables in each hemisphere, denoted by:

$$[z]^F = \{z_1^F, z_2^F, z_3^F\} \quad \text{and} \quad [z]^B = \{z_1^B, z_2^B, z_3^B\}, \tag{6.2}$$

where F indicates the forward and B the backward hemisphere and the indices 1,2,3 the first, second and third leading track, respectively.

In order to illustrate the sensitivity of each of the leading tracks to the event being forward or backward, figure 6.3 shows in arbitrary units the z_i^F distributions obtained by Monte Carlo in the case that the event is forward. From integration
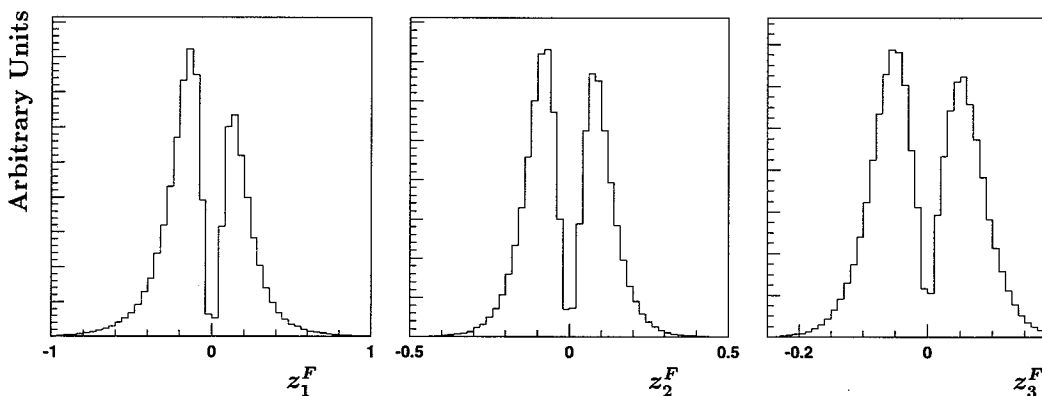
Figure 6.3: *Monte Carlo distributions for forward events of the z_i variables in the forward hemisphere. Note the horizontal scale differences between the z_1^F, z_2^F and z_3^F-plots.*

of the histograms for $z_i^F < 0$, one finds that the track fractions corresponding to a negative charge constitute respectively 58.8% , 53.1% and 52.8% of the total number of leading tracks. As expected, the first leading track is the most sensitive to the event being forward. The second and third track contain less information about the original event direction, but their combined use with the first leading track does increase the probability of properly identifying the event as either a forward or a backward one.

The weight w_F assigned to each event can be written as:

$$w^F = W^F([z]^F, [z]^B), \tag{6.3}$$

where W^F is the weight function, chosen such that the forward events (the "signal" events) are enhanced and the backward events (the "background" events) suppressed. A differently chosen weight function would not bias the final result, but only lead to a different sensitivity for the signal (see appendix B).

The weight function W^F is determined from Monte Carlo data. Its shape is calculated using two six-dimensional distributions of $([z]^F, [z]^B)$: one for forward generated and one for backward generated events, denoted as $f([z]^F, [z]^B)$ and $b([z]^F, [z]^B)$, respectively. The weight function is then defined as a combination of these two distributions:

$$W^F([z]^F, [z]^B) = \frac{f([z]^F, [z]^B)}{f([z]^F, [z]^B) + b([z]^F, [z]^B)}. \tag{6.4}$$

As usual, usage of such a Monte Carlo derived distribution requires a good agreement between data and Monte Carlo on the level of the input variables. Note that a weight function as defined in equation 6.4 is in essence the probability that any event, whether it is in reality forward or backward, is *identified* as a forward event. Thus for a forward event w^F should be $> \frac{1}{2}$; conversely $w^F < \frac{1}{2}$ for a backward event.

The Monte Carlo statistics available to calculate a function depending on six variables is far from sufficient. Therefore, a simplification is introduced, based on the assumption that the fragmentation of the forward jet is independent from the backward one, and vice versa. This assumption will cause no (or negligible) bias in the results, since only the leading tracks are considered, i.e. tracks which will seldom cross from one hemisphere to the other. The assumption of independent hemisphere fragmentation is equivalent with assuming that the distributions f and b can be factorised as follows:

$$\begin{aligned} f([z]^F, [z]^B) &= n([z]^F) \cdot p([z]^B), \\ b([z]^F, [z]^B) &= p([z]^F) \cdot n([z]^B), \end{aligned} \tag{6.5}$$

where n and p are the distributions for the three leading tracks in the hemisphere containing the negative and positive quark, respectively. This simplification results in a calculation of two three-dimensional histograms instead of one six-dimensional histogram.

Subsequently, each of the z-distributions is divided into 6 bins of unequal width, such that the numbers of events projected in each z-bin are approximately equal. The bin borders are found as:

$$\begin{array}{llllllll} z_1 : & -1, & -0.25, & -0.15, & 0, & 0.15, & 0.25, & 1; \\ z_2 : & -1, & -0.12, & -0.085, & 0, & 0.085, & 0.12, & 1; \\ z_3 : & -1, & -0.075, & -0.05, & 0, & 0.05, & 0.075, & 1. \end{array} \tag{6.6}$$

Two remarks can be made about the weight function. First, not only W^F but all multidimensional histograms introduced so far can be interpreted as probabil-

ity distributions. Thus the probability that a forward event yields the configuration $([z]^F, [z]^B)$ is given by $f([z]^F, [z]^B)$; the probability that a negative (positive) quark yields values $[z]$ is n (p), etc. Second, formulae 6.5 are $F \leftrightarrow B$ symmetric: $f([z]^F, [z]^B) = b([z]^B, [z]^F)$. This is however only valid in the approximation that the detector fully possesses this symmetry, which is not the case: the ECAL "dead" regions are not in symmetric positions and the ATRK matching will therefore not produce totally symmetric distributions. The solution to this problem is to separately factorise the forward and backward events:

$$\begin{aligned} f([z]^F, [z]^B) &= n^F([z]^F) \cdot p^B([z]^B), \\ b([z]^F, [z]^B) &= p^F([z]^F) \cdot n^B([z]^B). \end{aligned} \qquad (6.7)$$

The weight function is now obtained by a Monte Carlo determination of n^F, p^B, p^F and n^B. The resulting distributions are shown in figure 6.4. In each plot the sum of the open (forward) and shaded (backward) distribution is normalised proportional to the Standard Model number f_q (see equation 1.20) of the flavour under consideration. Thus the all-quark distribution is just a sum of all the other plots. The separative power of the weight function is clearly observed.

In order to take into account effects of the detector geometry, the weight function is constructed as a function of $|\cos\theta_T|$. Both the data and Monte Carlo samples are grouped in $|\cos\theta_T|$-bins of 0.2 width. Denoting i as the bin for which $0.2(i-1) < |\cos\theta_T| < 0.2i$, we call $N_{i,F}$ and $N_{i,B}$ the number of events where the negative quark travels in the direction $0.2(i-1) < \cos\theta_T < 0.2i$ and $-0.2i < \cos\theta_T < -0.2(i-1)$, respectively. Thus the right hand side of equation 6.3 and all quantities in equations 6.4, 6.5 and 6.7 obtain an extra subscript i.

The weights averaged over the i-th $|\cos\theta_T|$ bin are then given by:

$$\bar{w}_{i,F}^F = \frac{1}{N_{i,F}^{\text{MC}}} \sum_{n=1}^{N_{i,F}^{\text{MC}}} w_n^F, \qquad (6.8)$$

$$\bar{w}_{i,B}^F = \frac{1}{N_{i,B}^{\text{MC}}} \sum_{n=1}^{N_{i,B}^{\text{MC}}} w_n^F, \qquad (6.9)$$

where $N_{i,F}$ and $N_{i,B}$ represent the total number of forward and backward events in bin i, respectively. The number w_n^F is the weight for event n (belonging to bin i), as given by equation 6.3. The number of forward and backward events in the data are found by averaging the calculated event weights of the data sample. The average weight $\bar{w}_i^F$ in bin i is then given by[3]:

$$N_i \bar{w}_i^F = \sum_n^{N_i} w_n^F = N_{i,F} \cdot \bar{w}_{i,F}^F + N_{i,B} \cdot \bar{w}_{i,B}^F, \qquad (6.10)$$

---

[3] For a discussion of formula 6.10 and the following ones, see appendix B.
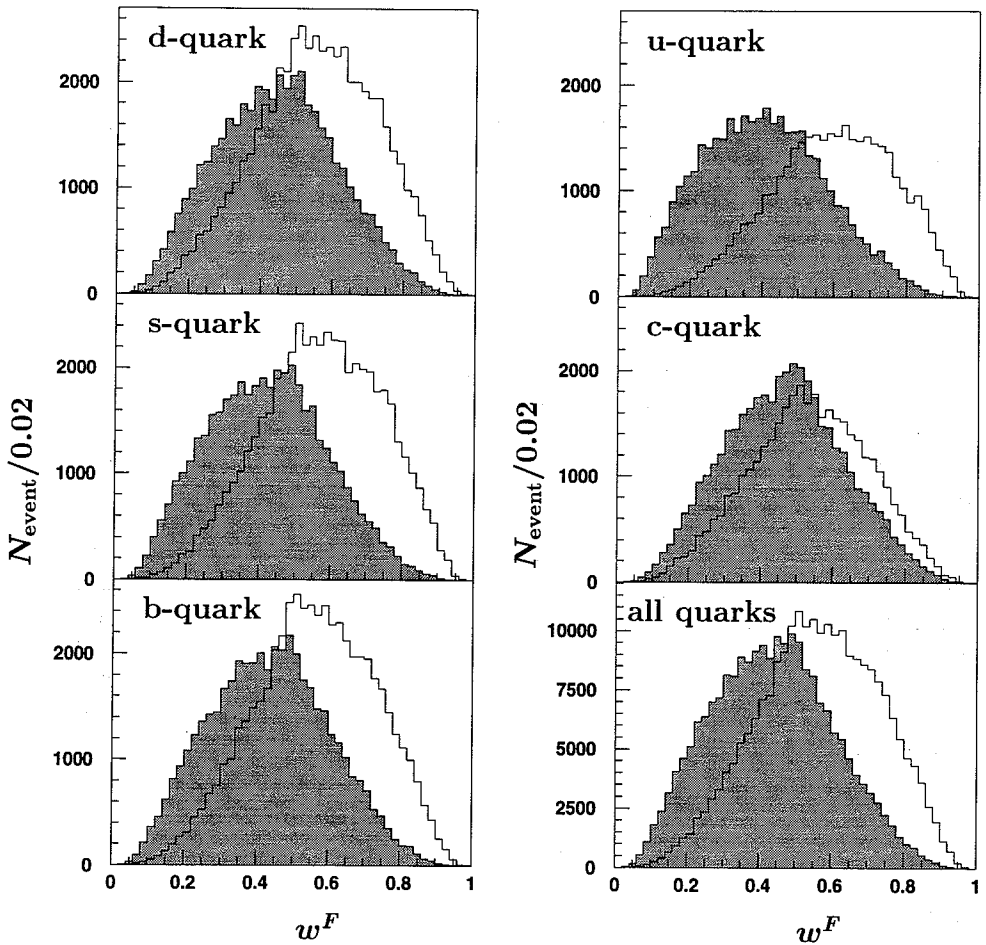
Figure 6.4: *Monte Carlo distributions of the weights w^F for forward (open histogram) and backward quarks (shaded histogram). The distributions are made both for each quark flavour separately and for all quark types together. See the text for the normalisations of these distributions.*

where N_i is the number of data-events in $|\cos\theta|$-bin i. Note that both $\bar{w}^F_{i,F}$ and $\bar{w}^F_{i,B}$ are determined entirely by Monte Carlo, but $\bar{w}^F_i$ by substituting measured $[z]^F$ and $[z]^B$ configurations in a Monte Carlo determined weight function.

Using the self-evident relation

$$N_i = N_{i,F} + N_{i,B},$$

one obtains two equations with two unknown variables $N_{i,F}$ and $N_{i,B}$. Solving these equations yields the number of forward and backward events in each $|\cos\theta_T|$ bin:

$$N_{i,F} = N_i \cdot \frac{\bar{w}_i^F - \bar{w}_{i,B}^F}{\bar{w}_{i,F}^F - \bar{w}_{i,B}^F}, \quad N_{i,B} = N_i \cdot \frac{\bar{w}_{i,F}^F - \bar{w}_i^F}{\bar{w}_{i,F}^F - \bar{w}_{i,B}^F}. \tag{6.12}$$

The corresponding statistical error on the number of forward and backward events is given by:

$$\Delta N_{i,F} = \Delta N_{i,B} = \sqrt{\frac{N_{i,F} N_{i,B}}{N_i} + \frac{N_{i,F} \cdot \sigma_{i,F}^2 + N_{i,B} \cdot \sigma_{i,B}^2}{(\bar{w}_{i,F}^F - \bar{w}_{i,B}^F)^2}}, \tag{6.13}$$

where $\sigma_{i,F}$ and $\sigma_{i,B}$ are the widths of the weight distribution for forward and backward events in bin i, respectively. The first term under the square root is the contribution due to the binomial distribution of $N_{i,F}$ and $N_{i,B}$; the second term results from the error on the weight function itself and reflects the imperfect separation power of the weight function. In the following discussion, the statistical error will be denoted by ΔN, omitting the subscripts F and B. Note that the errors on $N_{i,F}$ and $N_{i,B}$ are 100% anti-correlated.

From the data, asymmetries are obtained for the P-2, the combined Pre+P and the P+2 periods. Thus for each of these periods, an average weight $\bar{w}_i^F$ and a number of forward and backward events $N_{i,F}$ and $N_{i,B}$ is calculated in each $|\cos\theta_T|$-bin i. For all periods, the same weight function is used to evaluate the average weights.

Table 6.1 shows the average Monte Carlo weights for each quark type per $|\cos\theta_T|$-bin. As the difference of the average weights with $\frac{1}{2}$ is the largest in the bins $0.4 < |\cos\theta_T| < 0.6$ and $0.6 < |\cos\theta_T| < 0.8$, the data in these bins will also produce the best separation between forward and backward events.

A comparison per $|\cos\theta_T|$-bin of the weight distributions between data and Monte Carlo is given in figure 6.5. The distributions display a good agreement. As can be seen from table 6.2, the flavour-averaged Monte Carlo weights are also in good agreement with the average weights for data of the combined Pre+P period.

In principle, the forward-backward charge asymmetry is found by fitting the distribution $C(1 + \cos^2\theta_T + \frac{8}{3} A_{FB,h}^{ch} \cos\theta_T)$ – a simplified expression of equation 1.6 – to the numbers $N_{i,F}$ and $N_{i,B}$. To obtain a reliable result for $A_{FB,h}^{ch}$ we must first eliminate the detector effects which already cause an "unphysical" non-$(1 + \cos^2\theta_T)$ behaviour of the sum distribution $N_{i,F} + N_{i,B}$ (see figure 4.8 below). For this purpose the numbers $N_{i,F}$ and $N_{i,B}$ (and their errors) are scaled with a $|\cos\theta_T|$ dependent term such that the rescaled sum distribution shows the required $(1 + |\cos\theta_T|^2)$

Quark	Bin	$|\cos\theta_T|_i$	$\bar{w}_{i,F}^F$	$\bar{w}_{i,B}^F$
d-quark	1	0.0-0.2	0.5204±0.0012	0.4747±0.0012
	2	0.2-0.4	0.5607±0.0017	0.4408±0.0018
	3	0.4-0.6	0.5660±0.0016	0.4330±0.0018
	4	0.6-0.8	0.5667±0.0014	0.4355±0.0016
u-quark	1	0.0-0.2	0.5413±0.0015	0.4602±0.0015
	2	0.2-0.4	0.6060±0.0020	0.3946±0.0019
	3	0.4-0.6	0.6152±0.0020	0.3858±0.0016
	4	0.6-0.8	0.6113±0.0017	0.3856±0.0016
s-quark	1	0.0-0.2	0.5320±0.0012	0.4683±0.0013
	2	0.2-0.4	0.5805±0.0017	0.4158±0.0018
	3	0.4-0.6	0.5923±0.0016	0.4088±0.0018
	4	0.6-0.8	0.5911±0.0014	0.4074±0.0016
c-quark	1	0.0-0.2	0.5180±0.0013	0.4835±0.0013
	2	0.2-0.4	0.5381±0.0020	0.4627±0.0019
	3	0.4-0.6	0.5372±0.0019	0.4586±0.0018
	4	0.6-0.8	0.5403±0.0017	0.4610±0.0016
b-quark	1	0.0-0.2	0.5265±0.0012	0.4727±0.0013
	2	0.2-0.4	0.5704±0.0017	0.4301±0.0018
	3	0.4-0.6	0.5799±0.0016	0.4235±0.0017
	4	0.6-0.8	0.5740±0.0014	0.4257±0.0016
all quarks	1	0.0-0.2	0.5281±0.0006	0.4720±0.0006
	2	0.2-0.4	0.5709±0.0008	0.4292±0.0008
	3	0.4-0.6	0.5781±0.0008	0.4221±0.0008
	4	0.6-0.8	0.5767±0.0007	0.4234±0.0007

Table 6.1: *Average forward and backward weights $\bar{w}_{i,F}^F$ and $\bar{w}_{i,B}^F$ for Monte Carlo events.*

Bin	$|\cos\theta_T|_i$	$\bar{w}_i^F$ Monte Carlo	$\bar{w}_i^F$ Data
1	0.0-0.2	0.5006±0.0004	0.5009±0.0008
2	0.2-0.4	0.5023±0.0006	0.5031±0.0012
3	0.4-0.6	0.5037±0.0006	0.5033±0.0012
4	0.6-0.8	0.5041±0.0005	0.5041±0.0010

Table 6.2: *Average weights $\bar{w}_i^F$ derived from data and Monte Carlo for the combined 1993 (Pre+P) running periods.*
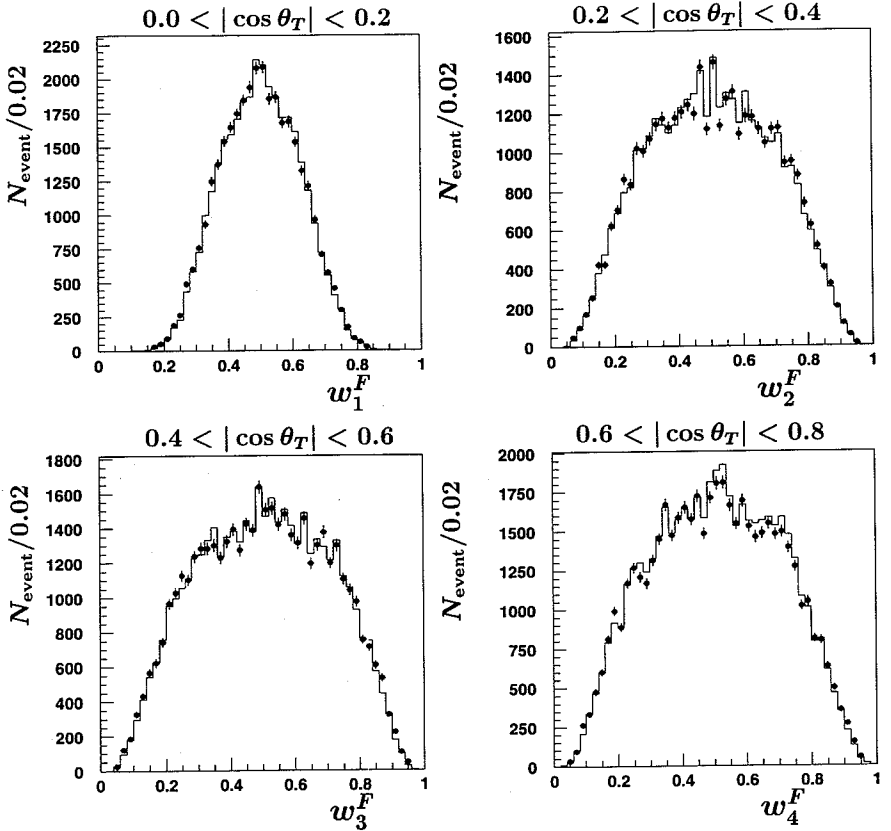
Figure 6.5: *Comparison of the weight distribution for data in the Pre+P period (dots) and the Monte Carlo (histogram) for the four* $|\cos\theta_T|$*-bins. The Monte Carlo distributions are normalised to the number of hadrons in the data.*

behaviour. As both $N_{i,F}$ and $N_{i,B}$ are scaled with the same factor, the asymmetry is independent of this scaling. The asymmetry is then found by fitting the function

$$0.2 \cdot \frac{3}{8}(1 + \cos^2\theta_T) + 0.2 \cdot A^{ch}_{FB,h} \cos\theta_T \qquad (6.14)$$

to the scaled event *fractions*; the factor 0.2 results from taking into account the $|\cos\theta_T|$-bin width.

The fit itself cannot be performed using the entire range $-1 < \cos\theta_T < 1$, since $N_{i,F}$ and $N_{i,B}$ in each bin i are 100% anti-correlated[4]. However, the fit can be done

---
[4] This limitation was neglected in the OPAL analysis [45].

with a standard interpretation for the resulting χ^2 just using either the set of (scaled) forward events or the set of (scaled) backward events. The fits for each period are shown in figure 6.6 together with the input forward and backward fractions used. For completeness the data-points obtained for the bin $0.8 < |\cos\theta_T| < 1.0$ – although not included in the analysis and the fits – are also shown. The fit results obtained are presented in table 6.3. Note that these values still need further corrections (see section 6.2).

period	A_{FB}^{ch}	χ^2/df
P$-$2	0.0471$\pm$0.0137	0.8
Pre+P	0.0405$\pm$0.0057	1.1
P+2	0.0313$\pm$0.0116	3.7

Table 6.3: *Uncorrected Charge asymmetries obtained from the fits shown in figure 6.6. Only the statistical errors are shown; the χ^2/df refers to one hemisphere of data points.*

6.2   Charge Asymmetry Corrections

The following effects lead to biases on the measurement of the forward-backward charge asymmetry and require corrections:

- the exact z-position of the vertex: the determination of the ASRC θ and ϕ angles (and thus the thrust axis $\hat{n}_T$) is based on the assumption that the interaction vertex lies exactly at the origin of the L3 coordinate system, which is generally not the case;

- the values used for the parameters ϵ_c and ϵ_b (see formula 1.33) in the fragmentation and hadronisation of the heavy quarks c and b: subsequent studies indicated that the values used in the 1993 Monte Carlo generation were too large [47].

The above-mentioned effects are different from the ones influencing the cross section measurement and described in chapter 5. Beam spread factors do not need to be applied because of the nearly linear behaviour of the asymmetry as a function of the CM energy (see figure 1.5). Most of the already small backgrounds are rejected by the cut on $\cos\theta_T$ (see figure 4.8); their contribution to the forward-backward charge asymmetry is therefore negligible. The triggers are only inefficient in the very forward and backward regions, i.e. the region we have excluded from the $A_{\mathrm{FB,h}}^{ch}$ selection.
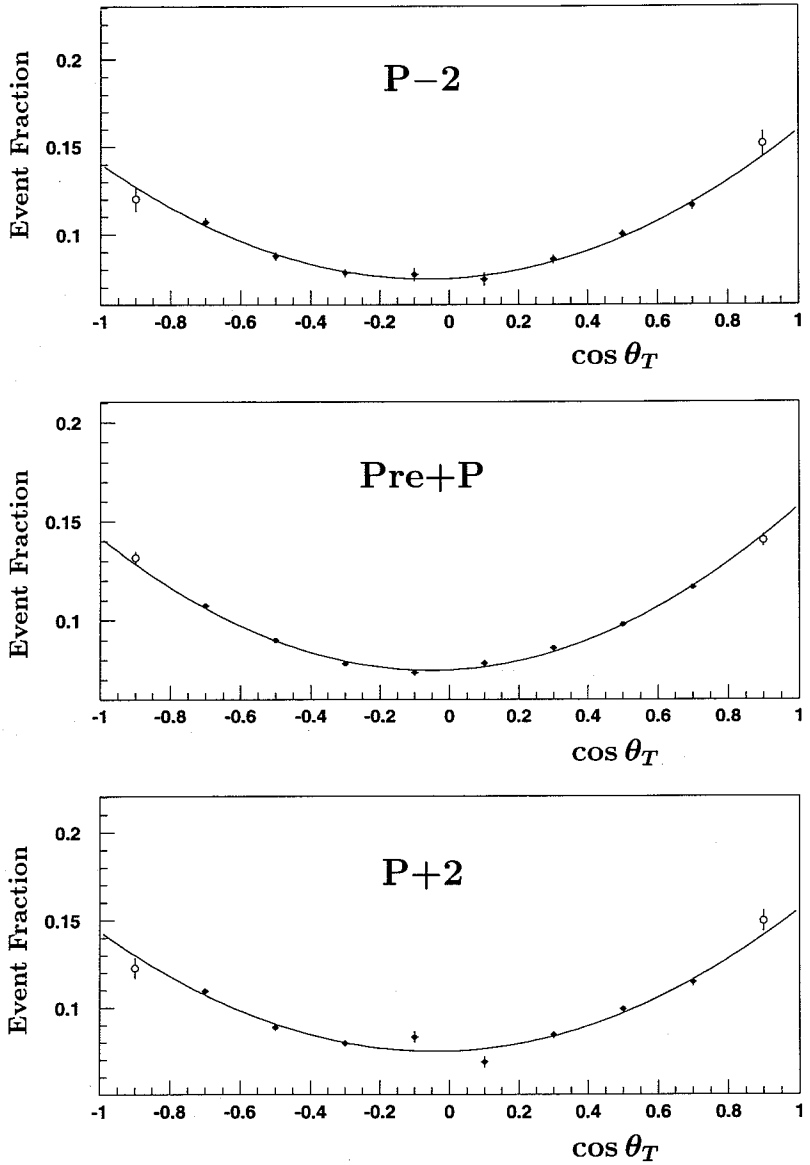
Figure 6.6: *Forward-backward asymmetry fits to the scaled forward and backward events. Not included in the fit are the (open) endcap points.*

6.2.1 Vertex Corrections

An incorrectly determined $\hat{n}_T$ leads to wrong w_i^F values. Taking into account the exact vertex position on an event-by-event basis turns out to be unreliable as it requires using the (often inaccurate) TEC z-information. However, an average fill-by-fill correction – using a list of vertex positions corresponding to the runs under consideration – is possible however.

The correction turns out to affect N_F and N_B in the bin $|\cos\theta_T| < 0.2$ bin only. It is evaluated by calculating the fraction of events which shift from the forward to the backward region (or vice versa) for a given shift of the vertex in z (positive or negative) and by subsequently translating this fraction-shift into an average weight-shift for the $|\cos\theta_T| < 0.2$ bin. The correction leads to the weights and asymmetry changes presented in table 6.4. The χ^2/df of the P+2 period improves from 3.7 (see table 6.3) to 2.7 but is still not satisfactory. Also shown is the *average* fill vertex position for each period. The errors on the asymmetry correction itself turn out to be negligible.

Period	$< z_{fill} >$ (mm)	$\Delta\bar{w}_1^F$	$\Delta A_{\mathrm{FB,h}}^{ch}$
P−2	−2.93±0.24	0.00068±0.00006	0.0005
Pre+P	−2.88±0.09	0.00068±0.00002	0.0005
P+2	−2.84±0.22	0.00069±0.00005	0.0004

Table 6.4: *Corrections to the weights and to the forward-backward charge asymmetries for the $|\cos\theta_T| < 0.2$ bin due to the shifts in the vertex z position.*

6.2.2 Fragmentation Function Corrections

The fragmentation and hadronisation parameters in JETSET have an influence on the configuration of the three leading tracks in each hemisphere. They control the fragmentation and hadronisation processes as described in chapter 1 and therefore affect the course of the track ordering process and the distributions of the leading tracks.

Using the variable x_E defined in section 1.4, the average ratios of the primary hadron energies are found to be $< x_E(c) >= 0.484 \pm 0.008$ and $< x_E(b) >= 0.702 \pm 0.008$ [47], which in terms of central values corresponds to $\epsilon_c = 0.031$ and $\epsilon_b = 0.0035$. The Peterson fragmentation parameters used in the JETSET generator of 1993 were however $\epsilon_c = 0.07$ and $\epsilon_b = 0.008$. A correction is estimated using events on the generator level (see chapter 3). A Monte Carlo sample is generated with the correct fragmentation parameters, and used to recalculate the weight function, the average weights $\bar{w}_{i,F}^F$ and $\bar{w}_{i,B}^F$ and the (correct) forward-backward charge

asymmetry. This new weight function is applied to a second Monte Carlo sample generated with the 1993 parameters, thus yielding a second (incorrect) forward-backward charge asymmetry. Making the assumption that the difference between the correct and incorrect asymmetry will not be significantly modified when going from the generator to the detector level, we thus obtain a correction from the difference between the correct asymmetry and the incorrect asymmetry. In order to obtain sufficient statistics, for both sets of parameters a Monte Carlo sample containing six million events was generated. For each sample this leads to a Monte Carlo statistical error of 0.0011 (see section 6.3.5), and to an error of 0.0015 on the difference referred to above.

A small correction of -0.0001 ± 0.0015 is obtained and applied to all asymmetry measurements.

6.3   Systematic Errors

The sources which, in principle, could cause significant systematic errors on $A_{\mathrm{FB,h}}^{ch}$, are:

- The event selection procedures. Three sources are of particular significance: the uncertainties related to the positions of the cuts on the sphericity ($S < 0.12$), on the polar thrust angle ($|\cos\theta_T| < 0.8$) and on the charge confusion ($CC < 10\%$).

- The polar angle measurement. Here two sources are expected to cause errors: the fill vertex position corrections discussed under section 6.2.1 as well as the distortions in the θ measurement of charged tracks.

- The Monte Carlo simulation. Again three sources could contribute: uncertainties in the modelling of the fragmentation/hadronisation processes, the deficiencies in the simulation of the TEC and the limited size of the Monte Carlo samples used.

Contrary to the procedure followed for the cross section measurements, where the task was to obtain precisions at the permille level and we were dealing with a strongly varying *relative* non-resonant background, the systematic errors on the forward-backward charge asymmetry will be determined for the peak energy data only and assumed to be also valid for the off-peak points. The reason for this assumption is that one a priori does not expect the contributing sources to be so energy dependent as to create systematic error variations over the small energy region involved, which are significant with respect to the order of 10% type errors expected for (some of) the systematic errors referred to above.

6.3.1   Event Selection Errors

To estimate the systematic error on the charge asymmetry resulting from the sources mentioned above, methods similar to the one described in section 5.4.1 are used.

The range over which the sphericity cut is varied (0.10-0.14), is based on an estimate of the effect on S resulting from the ASRC direction and energy measurement uncertainties. The $|\cos\theta_T|$-range is taken from the empirical fact that around $|\cos\theta_T| = 0.8$, the width of the distribution of the difference between the reconstructed thrust axis and the original quark direction is approximately 0.04. The range for the CC-cut (5% to 15%) follows from the discussion in section 4.2.

The variations of the forward-backward charge asymmetry as a function of the cut positions are shown in figure 6.7. At the 95% CL, none of these variations lead to a significant effect on $A_{\mathrm{FB,h}}^{ch}$. Therefore no systematic errors caused by the event selection are assigned.
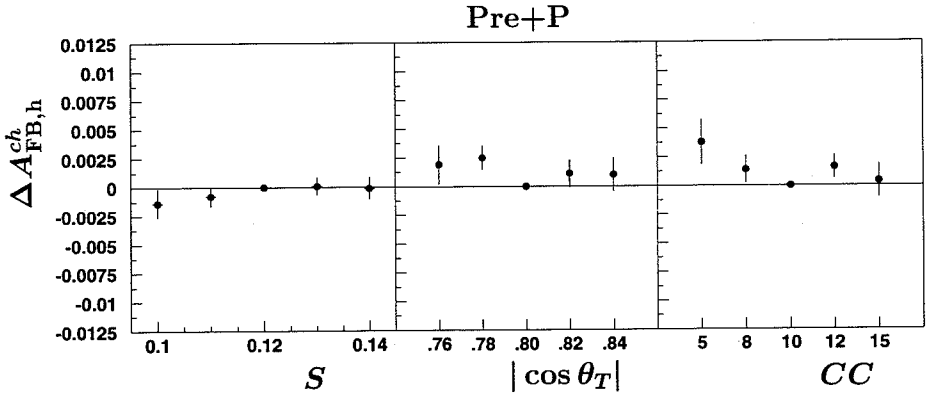
Figure 6.7: *The change of the Pre+P forward-backward charge asymmetry as a function of the position of the cut on the sphericity, on the polar angle of the thrust axis and on the charge confusion.*

Note that the general hadron selection criteria and the other sources discussed in section 5.4 do not cause significant contributions for the charge asymmetry measurement. These general criteria yield errors at the permille level (see table 5.8) whereas the largest of the systematic errors referred to above will turn out to be of the order of 10%.

Other cuts used in the event selection which, in principle, could contribute to the systematic error are the track pre-selection criteria of section 3.2.2, the hit distance criteria of section 3.2.2, the requirements that there be no tracks with momentum larger than the beam energy, and the cut on $N_{\mathrm{hit}}^{r\phi}$, the minimum number of hits containing $r\phi$ information. Both the systematic error due to the track pre-selection

criteria and to the $p < E_{\text{beam}}$ cut are fully correlated with the CC cut error and therefore do not need an independent variation[5]. The systematic contribution caused by the hit-distance criteria is also correlated, this time with the TEC modelling (see section 6.3.4). Finally, the influence of the position of the $N_{\text{hit}}^{r\phi}$ cut was tested by changing its central value from 20 to 25; no significant changes were observed.

6.3.2   Track Polar Angle Measurement Errors

The systematic error associated with the measurement of the track polar angle of the leading tracks can be estimated by inspecting the quantity $\Delta\theta = \theta - \theta_{\text{TTRK}}$, where θ is the polar angle of the matched track and θ_{TTRK} the polar angle of the unmatched track (see chapter 2). This can be done both as a function of the event $|\cos\theta_T|$ or as a function of the track $\cos\theta$.

Figure 6.8 shows a comparison of $\Delta\theta$ between data and Monte Carlo for a typical
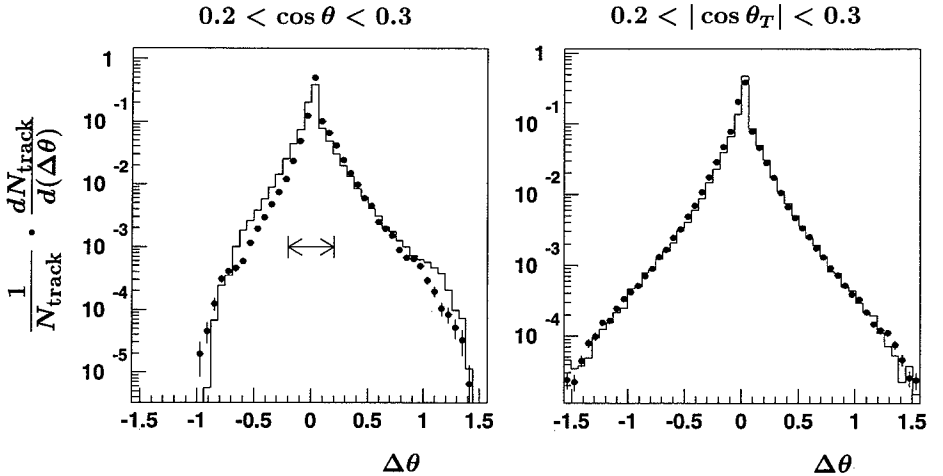
Figure 6.8: *The difference $\Delta\theta$ of the leading tracks for for measured data (solid points) and for Monte Carlo (histogram). The left plot is made in a typical bin of the track polar angle; the right plot of the polar angle of the thrust axis. The arrows indicate the region of the tracks with the best θ-measurements. Both distributions are normalised to one.*

---

[5]This argument is based on the assumption that the region defined by the 10% CC cut is more restrictive in the four-dimensional space of the variables p_T, ϕ_{local}, $|\cos\theta|$ and $N_{\text{hit}}^{r\phi}$ than the one defined by the pre-cuts on these variables themselves. We have explicitly checked this assumption and found two small violations; one for the drift region region in the TEC, where the $p < E_{\text{beam}}$ cut is somewhat more severe, and one for the $\cos\theta$ region near the TEC flanges where the $|\cos\theta| < 0.9$ cut is more restrictive. However, the number of events populating these regions are too small to cause any significant effect.

bin of $\cos\theta$, i.e. $0.2 < \cos\theta < 0.3$. One observes that the data peak is narrower than the Monte Carlo one. The asymmetric shape of the distribution is due to the fact that the θ before matching, i.e. obtained from the TEC-reconstruction only, is more confined to the central region than the θ after matching. The distributions of $\Delta\theta$ as a function of $|\cos\theta_T|$ show a similar behaviour. However, they are more symmetric (they do not suffer from the θ-pull referred to above) and the agreement between data and Monte Carlo is better.

No large effect is expected due to tracks with insufficient θ-information, because these tracks are in the tails of the $\Delta\theta$ distributions and the agreement between data and Monte Carlo is rather good. An estimate for a possible systematic error is obtained by comparing the total sample $A_{\text{FB,h}}^{ch}$ with the one obtained by just using the sample-half with the best θ-measurements, i.e. events with all leading tracks having a $|\Delta\theta| < 0.2$. For the Pre+P period the asymmetry changes by 0.0016. Comparing this number with the expected statistical fluctuation between these two subsamples, i.e. 0.0083, we conclude that no significant effect due to uncertainties in the polar angle measurement are observed.

6.3.3 Fragmentation and Hadronisation Modelling Errors

The parameters which are of importance for the hadronic forward-backward charge asymmetry are the following:

- Q_0: the mass cut-off parameter where the phase of parton showering stops and the hadronisation phase starts.
- Λ_{QCD}: the Λ cut-off value which is related to the running QCD coupling constant α_s.
- σ_q: the width of the transverse momentum distributions for hadrons produced during the hadronisation phase.
- b: a parameter in the Lund symmetric fragmentation function 1.32[6].
- ϵ_c and ϵ_b: the parameters of the Peterson function 1.33.
- γ_s: the relative rate of $s\bar{s}$ vs. $d\bar{d}$ and $u\bar{u}$ quark pair production during the fragmentation process.
- $V/(V + P)$: the ratio of vector to pseudoscalar meson production.
- χ_d and χ_s: the parameters describing the $B_0\bar{B}_0$-mixing.

For the reason given in section 6.2.2, the influence of the uncertainties of these parameters on the charge asymmetry needs an examination. They all somehow affect either the number of final state particles or their momenta.

The parameter Λ_{QCD} influences the course of the parton showering process, Q_0 determines where this process stops and thus together they affect the number of partons present when the hadronisation phase starts. The parameters σ_q and b

control the hadronisation process for the light quarks, in particular the momenta of the hadrons produced; ϵ_c and ϵ_b play the same role for the heavy quarks.

Via the production of $s\bar{s}$ quark pairs during fragmentation, the parameter γ_s controls the number of K_S^0 and K_L^0 particles, which appear both approximately once per $q\bar{q}$ event. The K_L^0 particle does not decay in the TEC region and thus leads to less detected charged particles.

The ratio $V/(V + P)$ affects the amount of orbitally excited mesons produced at the end of the hadronisation phase. As all these particles decay, dividing their energies over the decay products, their number again affects the amount and the momenta of the final state particles. However, since they are produced at the end of the hadronisation phase, their effect on the asymmetry is not large.

In the case of a $Z/\gamma \to b\bar{b}$ event, the $B_0\bar{B}_0$ mixing directly affects the charge of the detected final state hadrons.

Similar to the calculations of the fragmentation function corrections discussed in 6.2.2, systematic errors related to the JETSET parameters are evaluated entirely at the generator level. Each parameter is given three values within plus and minus one standard deviation and for each variation, $A_{\mathrm{FB},h}^{ch}$ is recalculated. A systematic error is considered to be present if an effect at 95% CL is visible. Only the effect of Q_0 and $B_0\bar{B}_0$ mixing is treated differently (see further). For each different parameter value, a different and modified Monte Carlo sample of about two million events is generated. Note that the statistical error on $A_{\mathrm{FB},h}^{ch}$ following from this "limited" generator Monte Carlo statistics is 0.0017 (or about 4% of $A_{\mathrm{FB},h}^{ch}$). Thus each parameter contribution examination is based on twelve million Monte Carlo events.

An overview of the central values of the parameters and their ranges is given in table 6.5. The Λ_{QCD}, σ_q and b ranges for $Q_0 = 1$ GeV are those given in reference 48. The range for the γ_s parameter is based on TASSO and PETRA measurements [49, 50]. The Peterson parameters ϵ_c and ϵ_b are varied around their corrected values within the ranges given in section 6.2.2; as they are tuned separately, they are varied independently and their errors uncorrelated. The ranges of the $V/(V + P)$-ratios are taken from a recent retuning presented in reference 51. The range of the $B_0\bar{B}_0$ mixing parameter χ_B is taken from reference 52.

After performing the parameter variation and the χ^2-tests, no parameter was found to lead to a significant systematic error. The variation which came closest to yielding a significant contribution was the one resulting from γ_s. As an illustration, figure 6.9 shows this variation[7].

---

[7] A criticism of this finding could be that the possibilities for the systematic errors to manifest themselves, are a priori limited by the size of the Monte Carlo (generator) samples used to estimate them. The first point to note then would be that the size of the reference Monte Carlo sample (the six million "correct" generator level events mentioned in section 6.2.2) and the fluctuations this sample does (or does not) allow are not relevant here, as each parameter variation starts from this same reference sample. More to the point however would be to question the size of the Monte Carlo samples generated after each parameter variation (two million per point; twelve million per parameter variation plot). We have tried to make an estimate of the possible effects

Parameter	Central Value	Range
Q_0 (GeV)	1.0	2.0
$\Lambda_{\rm QCD}$ (GeV)	0.30	0.27-0.33
σ_q (GeV)	0.39	0.36-0.42
b (GeV^{-2})	0.76	0.68-0.84
ϵ_c	0.031	0.026-0.037
ϵ_b	0.0035	0.0026-0.0045
γ_s	0.30	0.24-0.36
$V/(V+P)_{u,d}$	0.50	0.40-0.60
$V/(V+P)_s$	0.60	0.40-0.70
$V/(V+P)_{c,b}$	0.75	0.40-0.80
χ_B	0.145	0.129-0.161

Table 6.5: *Central values of the JETSET PS parameters and the ranges over which they are varied to estimate systematic error contributions.*
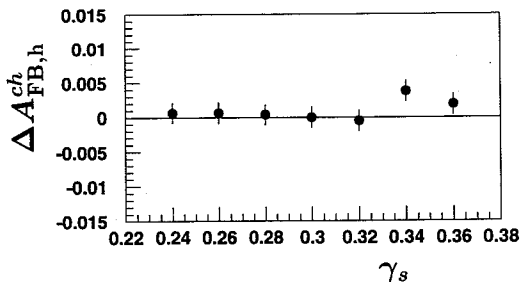
Figure 6.9: *Variation of the forward-backward charge asymmetry as a function of the fragmentation parameter γ_s; the fluctuations are consistent with the error on the central value at $\gamma_s = 0.3$.*

The systematic error related to the Q_0 choice is estimated by generating two Monte Carlo samples; one with $Q_0 = 1$ GeV and $\Lambda_{\rm QCD}$, σ_q and b as given in table 6.5

of the limitations and found it to be of the order of 2%; in other words: the size of the Monte Carlo samples used prevents detecting systematic effects smaller than 2%. This limitation should be compared to the statistical error (15%) and the systematic error (10%) on $A_{\rm FB,h}^{ch}$ (see tables 6.6 and 6.7). One should also note that substantially increasing the Monte Carlo samples is not only a non-trivial computer task (even on the event generator level), one also risks hitting the limits both of the validity of the Monte Carlo modelling itself and of the assumption that the shifts observed on the generator level are representative for those remaining on the detector level.

and one with $Q_0 = 2$ GeV using its (own) retuned set of Λ_{QCD}, σ_q and b values (0.29 GeV, 0.48 GeV and 0.82 GeV^{-2}, respectively [48]). Comparing the $A^{ch}_{\text{FB,h}}$ for these samples did also not yield a significant contribution.

The effect of $B_0\bar{B}_0$ mixing is calculated analytically using the theoretical $b\bar{b}$ asymmetry as input. In terms of the mixing parameter χ_B, the systematic error due to the uncertainty of the $B_0\bar{B}_0$ mixing parameters reads:

$$\delta A^{ch}_{\text{FB,h}} = f_b \cdot 2\Delta\chi_B \cdot A_{\text{FB},b}, \tag{6.15}$$

where f_b and $A_{\text{FB},b}$ are the same variables as used in equation 1.21. The resulting systematic error is found to be 0.0003.

Thus the only error which is found to contribute to the fragmentation and hadronisation uncertainties, is the one from $B_0\bar{B}_0$ mixing.

6.3.4   TEC Simulation Errors

As the distributions given in figures 4.9 and especially in figures 3.9 still show some disagreement between data and real Monte Carlo, another source which contributes to the systematic error are the imperfections in the modelling of the TEC hit smearing. Also the imperfections in the description of the TEC sector efficiencies are a source which contributes to the systematic error.

In principle the first systematic error could to be obtained by changing the hit smearing function within the error ranges of its parameters, but this would be a major Monte Carlo task. The systematic error is therefore estimated using the relative differences in the discrepancies before and after smearing between data and Monte Carlo in the ϕ_{local} distribution of $\sigma(d_{\text{hit}})$. These estimates are derived per ϕ_{local}-bin and subsequently averaged over the inner and outer TEC and over all sectors. An average scaling factor of 0.208 ± 0.025 is obtained. The forward-backward charge asymmetry error consequences of the TEC simulation error are then obtained by multiplying this scale factor with the absolute difference $|\Delta A^{ch}_{\text{FB,h}}|$, i.e. the difference in $A^{ch}_{\text{FB,h}}$ before and after smearing.

The absolute difference is found to be $|\Delta A^{ch}_{\text{FB,h}}| = 0.0027$. After multiplication with the scaling factor, the systematic error from uncertainties in the smearing is derived as $\delta A^{ch}_{\text{FB,h}} = 0.0006$. As explained in section 6.3.1, this error also accounts for systematic contributions from the hit elimination procedure.

The deficiencies in the simulation of the sector efficiencies are found from a propagation of the error on the efficiency of the left half of sector 4 (see equation 3.2) to the forward-backward charge asymmetry. As only this half-sector is inefficient and the track ordering replaces a rejected leading track in this half-sector by another leading track, the systematic error related to the half sector simulation deficiencies is negligible.

6.3.5 Monte Carlo Statistical Errors

The statistical error due to the limited Monte Carlo sample is taken into account by means of a systematic error on $N_{i,F}$ and $N_{i,B}$. It is given by:

$$\delta N_i^{\text{MC}} = \frac{N_i}{(\bar{w}_{i,F}^F - \bar{w}_{i,B}^F)^2} \cdot \sqrt{(\bar{w}_i^F - \bar{w}_{i,F}^F)^2 \frac{\sigma_{i,B}^2}{N_{i,B}^{\text{MC}}} + (\bar{w}_i^F - \bar{w}_{i,B}^F)^2 \frac{\sigma_{i,F}^2}{N_{i,F}^{\text{MC}}}}. \qquad (6.16)$$

The formula applies both to $N_{i,F}$ and $N_{i,B}$. Note that, similar to the case of the statistical error (see equation 6.13), the error on $N_{i,F}$ is 100% anti-correlated with the corresponding error on $N_{i,B}$.

The added error on $N_{i,F}$ (and $N_{i,B}$) translates into a systematic error on the forward-backward charge asymmetry. For each $|\cos\theta_T|$-bin i, a Gaussian random number is generated with a width given by equation 6.16. This number is added to $N_{i,F}$ (or equivalently subtracted from $N_{i,B}$). The asymmetry is then refitted with the modified $N_{i,F}$, thus leading to an $(A_{\text{FB,h}}^{ch})'$. This procedure is repeated 10,000 times. The resulting $(A_{\text{FB,h}}^{ch})'$s are histogrammed and a Gaussian function is fitted. The width of this Gaussian is used as an estimate of the systematic error following from the limited Monte Carlo statistics.

The Monte Carlo statistical error turned out to be the same for all periods and equal to 0.0037.

6.3.6 Summary of Systematic Errors

Table 6.6 gives a summary of all systematic errors on the forward-backward charge asymmetry. The total systematic error is obtained by adding the systematic errors from each source in quadrature.

Source	$\delta A_{\text{FB,h}}^{ch}$
Peterson correction	0.0015
MC statistics	0.0037
TEC simulation	0.0006
Fragmentation/Hadronisation	0.0003
Total systematics	0.0040

Table 6.6: *Summary of the systematic errors for the forward-backward charge asymmetry measurement.*

We observe that after applying the real TEC simulation described in chapter 3, the systematic error due to the remaining uncertainties in the TEC modelling are small. The dominant charge asymmetry error source is the limited real detector Monte Carlo statistics.

6.4   Results

The forward-backward charge asymmetries obtained after the corrections for the fill vertex position (see section 6.2.1) and the Peterson fragmentation function parameters (see section 6.2.2) are presented together with their errors in table 6.7. These asymmetries will be used as input for the Standard Model fits to be described in chapter 7.

Period	$A_{\text{FB,h}}^{ch}$	χ^2/df
P$-$2	$0.0474\pm0.0137\pm0.0040$	0.5
Pre+P	$0.0399\pm0.0059\pm0.0040$	1.4
P+2	$0.0316\pm0.0116\pm0.0040$	2.7

Table 6.7: *Forward-backward charge asymmetries $A_{\text{FB,h}}^{ch}$ obtained from the 1993 data. The first errors are statistical, the second systematic.*

7

Standard Model Tests and Fits

The hadronic cross section and the forward-backward charge asymmetry measurements can be used for tests of the Standard Model. From the hadronic cross section data the mass and width of the Z boson can be derived; using in addition the hadronic forward-backward charge asymmetries yields a measurement of the effective weak mixing angle. The use of these data alone is however not sufficient to perform a complete test of the Standard Model; also the leptonic data, i.e. the results from $e^+e^- \to \gamma/Z \to \ell^+\ell^-$ are needed as input. So-called *model-independent* fits are then performed to these data which yield the effective parameters occurring in the (radiatively corrected) improved Born approximation.

A first test is obtained by performing a fit to the hadronic and leptonic cross section data at the various energy points. This yields the Z mass and width M_Z, Γ_Z and the partial widths Γ_h, Γ_e, Γ_μ, and Γ_τ (see equations 1.11 and 1.12). These widths can be compared with the Standard Model predictions, evaluated from the input parameters M_Z, M_H, m_t, $\alpha_s(M_Z^2)$ and $\alpha(M_Z^2)$. A second test is obtained when also the leptonic forward-backward charge asymmetry data are used: this yields M_Z, Γ_Z, Γ_h and the effective lepton coupling constants $\bar{g}_V^e$, $\bar{g}_A^e$, $\bar{g}_V^\mu$, $\bar{g}_A^\mu$, $\bar{g}_V^\tau$, and $\bar{g}_A^\tau$ which can again be compared with the Standard Model predictions.

Apart from small mass effects in the τ channel, the Standard Model predicts the lepton couplings to be exactly equal – this is called lepton universality. The assumption is tested by performing the fits with and without imposing this equality. We will also make consistency checks by comparing $\sin^2 \bar{\theta}_W$ values obtained using different types of measurement input.

Once its validity established, fits can be performed within the Standard Model framework, and its parameters derived. Results are obtained either for a fit leaving all parameters free or for fits which fix some of these parameters to an externally determined range.

In a strict sense, the first method is not completely model independent. There is a $\gamma - Z$ interference term in the expression of the differential cross section 1.6, which is difficult to measure. It is therefore put equal to its Standard Model value using as input the values obtained in reference 16, i.e. $m_t = 175$ GeV, $M_H = 300$ GeV and $\alpha_s = 0.123$. In principle one should iterate this procedure, but the interference term turns out to be small and the improvements resulting from iteration negligible[1]. Another (small) model dependence is introduced by the way we take into account the s and t channel interference terms of the Bhabha channel. To predict their contribution the ALIBABA program is used [54] and the result obtained is subtracted from the measured e^+e^- cross sections before using them in the fits.

The quantities to be determined are calculated by means of a χ^2 fit to the above mentioned input data. The ZFITTER package [14], already used to derive the curves plotted in figures 1.5, is employed to calculate the theoretical cross sections and forward-backward charge asymmetries from the fit parameters. The minimisation procedure itself is performed using the MINUIT program [55]. In the fit all errors on the input quantities have to be taken into account. There is a group of systematic uncertainties which enter *both* in the hadronic and leptonic channels, namely the errors on the luminosity, the LEP energy and the beam spread factors; such errors must be entered in the corresponding covariance matrix fully correlated.

7.1   Model Independent Results

As stated above, our first step is a fit of the widths of the various channels involved to the measured hadron and lepton cross sections. Both fits with and without assuming lepton universality are performed; the results are presented in table 7.1. Good χ^2/df values are obtained. The results with and without assuming lepton universality are in good agreement. They also compare well with the Standard Model predictions, using $M_Z = 91.1919$ GeV, $m_t = 175$ GeV, $M_H = 300$ GeV and $\alpha_s = 0.123$ as input.

The contribution of the LEP beam energy errors to the total error on the mass and width of the Z boson is estimated by repeating the fit without using the error on the LEP beam energy and taking the quadratic difference of the total error obtained from the fits with and without the inclusion of the uncertainty on the LEP energy. This procedure yields the following results:

$$
\begin{aligned}
M_Z &= (91.1915 \pm 0.0030 \pm 0.0025)\ \text{GeV}, \\
\Gamma_Z &= (2.5023 \pm 0.0051 \pm 0.0019)\ \text{GeV},
\end{aligned}
\tag{7.1}
$$

---

[1] The interference term can actually be measured by including in the fits cross section data off the Z peak [53].

parameter	no lepton univ.	lepton univers.	Standard Model
M_Z (GeV)	91.1915±0.0039	91.1915±0.0039	-
Γ_Z (GeV)	2.5023±0.0054	2.5023±0.0054	2.4963
Γ_h (GeV)	1.7499±0.0071	1.7474±0.0056	1.7432
Γ_e (GeV)	0.08383±0.00031	-	0.08393
Γ_μ (GeV)	0.08380±0.00058	-	0.08393
Γ_τ (GeV)	0.08475±0.00072	-	0.08374
Γ_ℓ (GeV)	-	0.08396±0.00023	0.08387
χ^2/df	78.6/74	80.9/76	

Table 7.1: *Results of the model independent fits to the hadron and lepton cross section data with and without assuming lepton universality.*

where the first error is experimental and the second is the LEP beam energy error; one concludes that for M_Z both errors are of about equal size, whereas for Γ_Z the experimental error dominates. For comparison, the values given in Filthaut's thesis [7] were $M_Z = 91.197 \pm 0.006 \pm 0.007$ GeV and $\Gamma_Z = 2.492 \pm 0.010 \pm 0.005$ GeV. The much smaller beam energy errors in equation 7.1 are the result of using the resonant depolarisation technique for all energy points during the 1993 scan period.

In a second step, the effective leptonic coupling constants $\bar{g}_V^f$ and $\bar{g}_A^f$ are fitted, which requires adding the lepton forward-backward charge asymmetry measurements to the fit-input data (see equations 1.16 and 1.17). As the cross sections and forward-backward asymmetries are available for each leptonic channel separately, the individual effective couplings for the leptons can be fitted. The hadron input information is however still limited. To obtain all individual quark effective couplings, the cross sections and the forward-backward charge asymmetries for each flavour separately would be needed. For L3, only the $b\bar{b}$ fraction f_b and the forward-backward charge asymmetries $A_{FB,b}$ were measured [56, 57]; we therefore have to limit ourselves to the determination of an overall Γ_h width.

Again the fits are performed with and without the assumption of lepton universality. The results are shown in table 7.2. Note that the signs of the coupling constants are chosen as required by neutrino scattering data [58]. Like the fits to the cross section data only, good χ^2/df are obtained and the results from the fits with and without lepton universality are again in agreement both with each other and with the Standard Model predictions.

parameter	no lepton univ.	lepton univers.	Standard Model
M_Z (GeV)	91.1919±0.0039	91.1919±0.0039	–
Γ_Z (GeV)	2.5022±0.0054	2.5022±0.0054	2.4963
$\Gamma_{\rm h}$ (GeV)	1.7502±0.0063	1.7471±0.0056	1.7432
$\bar{g}_A^e$	−0.5014±0.0010	-	−0.5012
$\bar{g}_V^e$	−0.026±0.013	-	−0.0362
$\bar{g}_A^\mu$	−0.4996±0.0033	-	−0.5012
$\bar{g}_V^\mu$	−0.050±0.029	-	−0.0362
$\bar{g}_A^\tau$	−0.4971±0.0094	-	−0.5012
$\bar{g}_V^\tau$	−0.089±0.052	-	−0.0362
$\bar{g}_A^\ell$	-	−0.5011±0.0007	−0.5012
$\bar{g}_V^\ell$	-	−0.0386±0.0038	−0.0362
χ^2/df	118.0/131	124.1/135	

Table 7.2: *Results of the model independent fits to the hadron and lepton cross section and to the lepton forward-backward charge asymmetry data with and without assuming lepton universality.*

A comparison of the fitted hadron cross section curve with the experimental measurements is displayed in figure 7.1(a). As the errors in this plot are too small to be visible, a "linearised" blow-up is given in figure 7.1(b). Note that the 1993 statistical cross section errors for the off-peak points are significantly smaller than for the 1990 and 1991 data. As reflected by the χ^2/df of the fit, the experimentally measured cross sections are in good agreement with the fitted curve.

We can also use the hadron and lepton cross sections together with the hadron forward-backward charge asymmetries to derive an effective weak mixing angle. In practice this is done by fitting M_Z, Γ_Z and $\sin^2 \bar{\theta}_W$ to five data points, three supplied by the hadron forward-backward charge asymmetry and two by the fit-results for M_Z and Γ_Z given in table 7.1. The result obtained is:

$$\boxed{\sin^2 \bar{\theta}_W = 0.2327 \pm 0.0023 \pm 0.0019,} \tag{7.2}$$

where the first error is statistical and the second systematic. Summing these errors in quadrature yields a total uncertainty on the mixing angle of 0.0030. Note that M_Z and Γ_Z are essentially controlled by $\sigma_{\rm h}$; the role of σ_ℓ is a minor one. One could therefore qualify this $\sin^2 \bar{\theta}_W$ determination as one which is primarily based on hadronic data only.
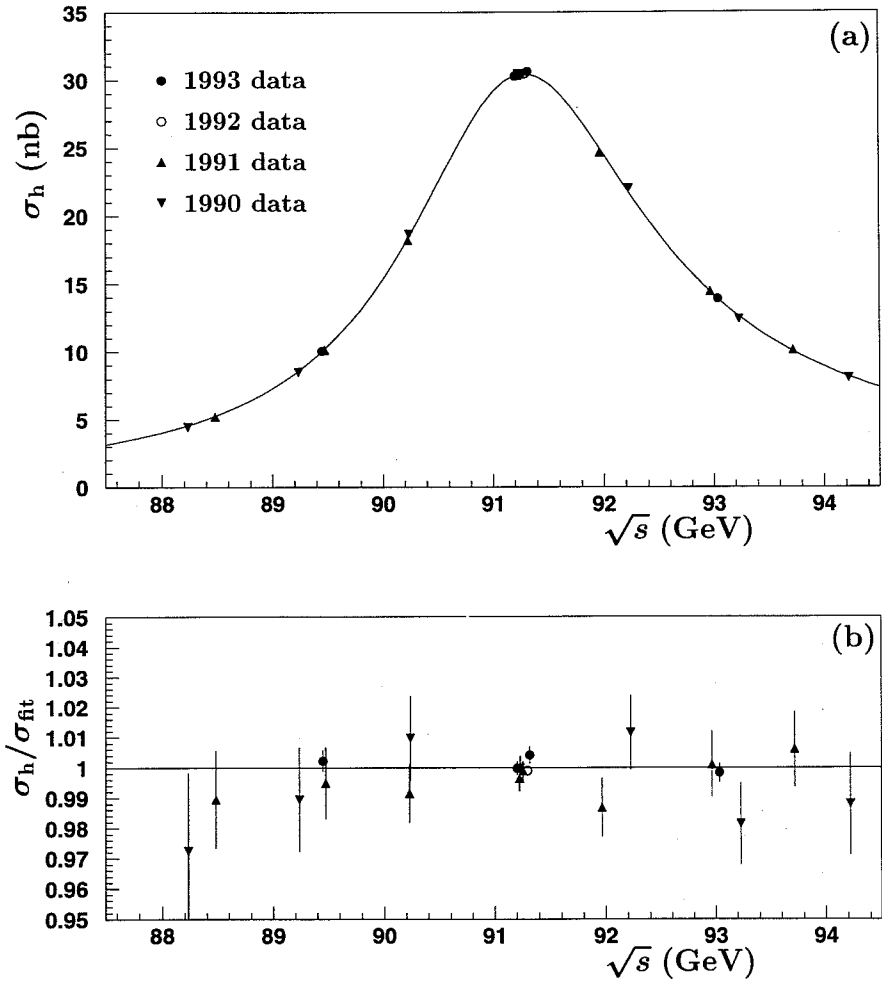
Figure 7.1: *Comparison of the fitted hadron line shape to the measured hadronic cross sections. Only the statistical errors are shown.*

Figure 7.2 displays the contours at the 68% CL in the $\bar{g}_V^\ell$-$\bar{g}_A^\ell$ plane, calculated with and without including the hadron asymmetries. Taking into account the hadronic forward-backward charge asymmetry data leads to a small improvement of the errors on $\bar{g}_V^\ell$ and $\bar{g}_A^\ell$, while the minimum shifts to a somewhat lower $\bar{g}_V^\ell$-value. Also drawn are the Standard Model predictions for these coupling constants as a function of the top and Higgs mass. The variations in m_t and M_H indicate that our results are sensitive to the top mass but hardly so to the Higgs mass.
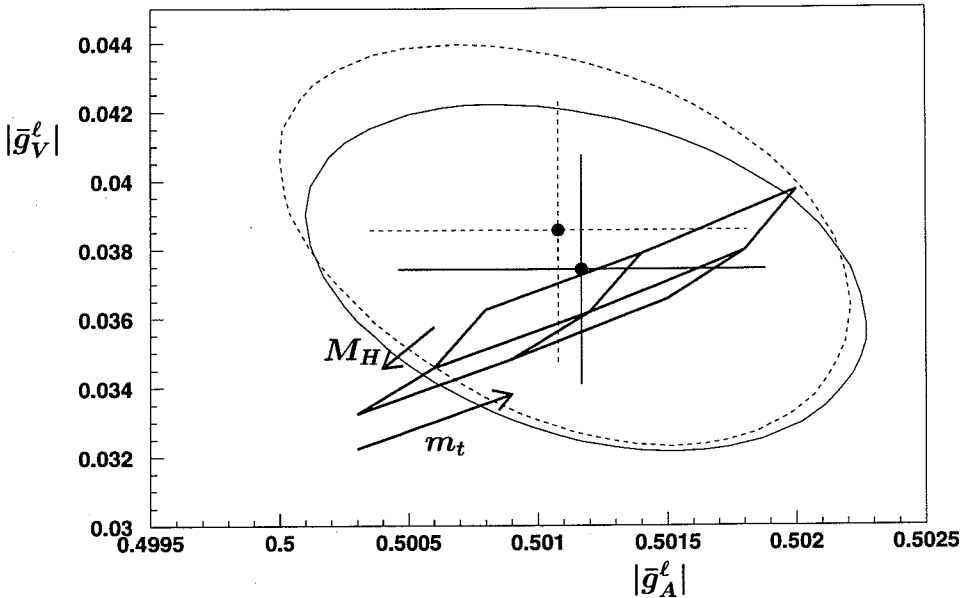
Figure 7.2: *Contour plots at 68% CL in the $\bar{g}_V^\ell$-$\bar{g}_A^\ell$ plane around the central fit values with the constraint on $\sin^2\bar{\theta}_W$ obtained from the hadron forward-backward charge asymmetry data (solid curve) and without (dashed curve). The raster corresponds to the Standard Model prediction for different values of m_t (150 GeV, 175 GeV and 200 GeV) and M_H (60 GeV, 300 GeV, 1000 GeV). The arrows point in the direction of increasing m_t and M_H values.*

A comparison of $\sin^2\bar{\theta}_W$ values obtained by other LEP experiments, also based on hadronic data only, is presented in table 7.3. We observe that all numbers agree well within the errors.

Experiment	Data	$\sin^2 \bar{\theta}_W$
ALEPH [59, 9]	90-94 final	$0.2322 \pm 0.0008 \pm 0.0011$
DELPHI [60, 61]	91-94 prel.	$0.2311 \pm 0.0010 \pm 0.0014$
OPAL [45, 8]	91-94 prel.	$0.2326 \pm 0.0012 \pm 0.0013$
This analysis	93	$0.2327 \pm 0.0023 \pm 0.0019$

Table 7.3: *Comparison between the effective electroweak mixing angles measured by other LEP experiments and our result, all measured using in essence hadron data only.*

In table 7.4 our "hadronic" weak mixing angle is compared with values obtained from other types of measurements using L3 data, namely from the b quark charge asymmetry [57], from the τ polarisation [62], and from $\bar{g}_V^\ell$ and $\bar{g}_A^\ell$ (see table 7.2). Once more all numbers are in good agreement with each other, which is again a

Measurement	$\sin^2 \bar{\theta}_W$
$A_{\mathrm{FB,b}}$	0.2335 ± 0.0021
τ Pol.	0.2309 ± 0.0016
$\bar{g}_V^\ell$-$\bar{g}_A^\ell$	0.2308 ± 0.0019
This analysis	0.2327 ± 0.0030

Table 7.4: *Comparison between effective electroweak mixing angles obtained from other L3 measurements and our "hadronic" result.*

confirmation of the Standard Model.

We can make a "best" $\sin^2 \bar{\theta}_W$ determination for the L3 data up to and including 1993 by combining all the information referred to above. In practice this is done by fitting M_Z, Γ_Z, Γ_h, $\bar{g}_V^\ell$ and $\bar{g}_A^\ell$ (assuming lepton universality) to the hadronic and leptonic cross section and to the leptonic asymmetry data, and adding three "data" points resulting from $A_{\mathrm{FB,h}}^{ch}$, $A_{\mathrm{FB,b}}$ and P_τ as additional constraints[2]. From the fitted $\bar{g}_V^\ell$ and $\bar{g}_A^\ell$ thus obtained, we derive a "best" $\sin^2 \bar{\theta}_W$:

$$\sin^2 \bar{\theta}_W = 0.2316 \pm 0.0010. \tag{7.3}$$

---

[2]There is a correlation between the $A_{\mathrm{FB,h}}^{ch}$ and $A_{\mathrm{FB,b}}$ results. This correlation has been estimated to be between 20% to 25%, and only leads to a small change on the effective weak mixing angle; it has therefore been neglected.

As a check, in figure 7.3 the $A_{\text{FB,h}}^{ch}$ prediction curve, following from using result 7.3 as input, is directly compared to the $A_{\text{FB,h}}^{ch}$ results of table 6.7; as expected a good agreement is observed.
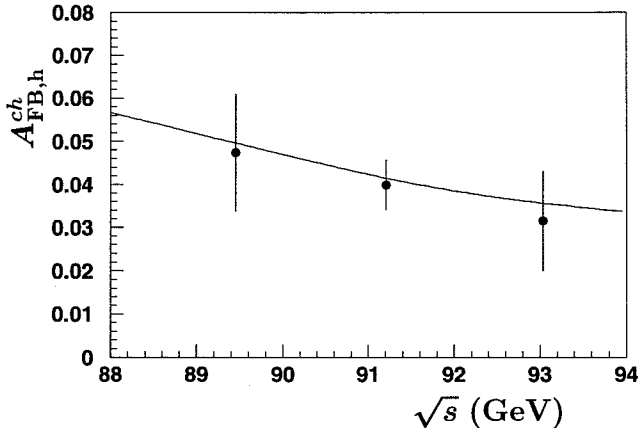

Figure 7.3: *Comparison of the $A_{\text{FB,h}}^{ch}$ prediction following from result 7.3 and the measured hadronic forward-backward charge asymmetries. Only the statistical errors are shown.*

7.2   Standard Model Results

Given the agreement between the Standard Model prediction and the fit results described in the previous section, one can perform fits within the framework of the Standard Model and determine the parameters M_Z, m_t, M_H, $\alpha_s(M_Z^2)$ and $\alpha(M_Z^2)$. As the sensitivity of the data to the Higgs mass is logarithmic (see equation 1.28) and thus very weak, this parameter is not treated as a fit variable but fixed to a central value of 300 GeV; its effect on the fitted parameters is studied a posteriori by varying this mass between 60 GeV and 1000 GeV and taking the resulting fit-parameter changes as an additional error.

Instead of directly fitting to the cross section and asymmetry data, one generally fits to the outcome of the model independent fits given in table 7.2, i.e. M_Z, Γ_Z, Γ_{h}, $\bar{g}_V^\ell$ and $\bar{g}_A^\ell$, again complemented by the three "data" points supplied by the $A_{\text{FB,h}}^{ch}$, $A_{\text{FB,b}}$ and P_τ measurements already used to obtain result 7.3. The fits take into account the full covariance matrix on the fitted parameters and assume lepton

universality. The resulting parameters are:

$$
\begin{aligned}
M_Z &= (91.1916 \pm 0.0039)\ \text{GeV}, \\[2mm]
m_t &= (173^{+27+14}_{-31-8})\ \text{GeV}, \\[2mm]
\alpha_s(M_Z^2) &= 0.1315 \pm 0.0082^{+0.0021}_{-0.0011}, \\[2mm]
\alpha(M_Z^2) &= 1/(129.05 \pm 0.58^{+0.09}_{-0.22}),
\end{aligned}
\tag{7.4}
$$

where the first error is experimental (statistical and systematic) and the second due to the Higgs mass variation (the mass M_Z is independent of the Higgs mass).

The value obtained for the mass of the Z boson is consistent with the result derived from the model independent fits. The top mass value is in agreement with the combined CDF/D0 result $m_t = (175 \pm 6)$ GeV [2]. The result for $\alpha_s(M_Z^2)$ compares well with the value $\alpha_s = 0.123 \pm 0.006$ obtained from event shape measurements at LEP [63]. The measurement $\alpha(M_Z^2)$ overlaps with the result $\alpha = 1/(128.90 \pm 0.09)$ obtained in a recent re-analysis of low-energy hadronic cross section data [64, 65]. Figure 7.4 illustrates the m_t versus $\alpha_s(M_Z^2)$ dependence within 68% CL resulting
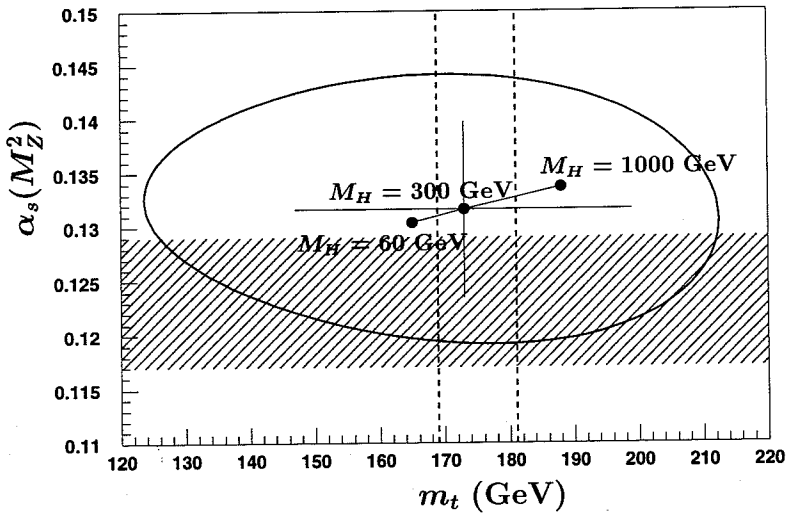

Figure 7.4: *Contour plot at 68% CL in the m_t-$\alpha_s(M_Z^2)$ plane around the central value. The points denote the position of the central value as a function of the Higgs mass. The hatched area denotes the α_s measurement obtained from event shape variables; the vertical dashed lines show the m_t limit from the combined CDF and D0 results.*

from the fit; the hatched band represents the $\alpha_s(M_Z^2)$ event shape measurement.

An attempt is made to determine the mass of the Higgs boson. For this purpose $\alpha_s(M_Z^2)$ and $\alpha(M_Z^2)$ are fixed to the (precise) external values referred to above; m_t, M_H and M_Z are left free parameters. The value found for M_Z is identical to the one given before (see result 7.4); for the other two parameters one finds:

$$m_t = (167^{+40}_{-21}) \text{ GeV},$$
$$M_H = (68^{+1259}_{-56}) \text{ GeV}. \tag{7.5}$$

The asymmetric errors for M_H are due to the logarithmic dependence of the radiative corrections on M_H (see equation 1.28). When in addition m_t is constrained to the value (175 ± 6) GeV resulting from combining the CDF and D0 results [2], the accuracy of the result improves significantly:

$$M_H = (124^{+336}_{-111}) \text{ GeV} \tag{7.6}$$

This Higgs mass result is less restrictive than, but consistent with, the lower limit obtained from direct searches, $M_H > 58.4$ GeV at 95% CL [1]. From result 7.6 we can also conclude that at 68% CL the Higgs mass should be < 460 GeV.

Figure 7.5 shows the M_H-m_t contour plot at 68% CL. Note the logarithmic scale of the y-axis. Without the m_t constraint the M_H information is – as expected – very weak; the allowed region even stretches into the region $M_H \gtrsim 1$ TeV where the Higgs theory is no longer expected to be valid [66]. Use of the precision of the CDF and D0 result is essential to obtain a meaningful Higgs-mass estimate.

7.3   Conclusions and Outlook

The measurements of the $e^+e^- \rightarrow \gamma/Z \rightarrow q\bar{q}$ cross section and forward-backward asymmetries reported in this thesis are part of the ever growing amount of experimental data which confirm the validity of the Standard Model and increase the precision with which we know its parameters. In terms of hadronic forward-backward (charge) asymmetries, most results reported thus far have been for the easily identifiable $\gamma/Z \rightarrow b\bar{b}$ hadron final state. Our results measure – and this for the first time on the basis of L3 data – this charge asymmetry averaged over all quark species. Although less sensitive to Standard Model parameters than the $b\bar{b}$ forward-backward asymmetry alone, it does constitute an important link in the chain of experimental confirmations of the Standard Model and is as such also one of the last major Standard Model observables which had not yet been determined using L3 data.

Looking at the future of measurements as described here: for the total cross sections and the on-peak data, the systematic errors (especially the one related to
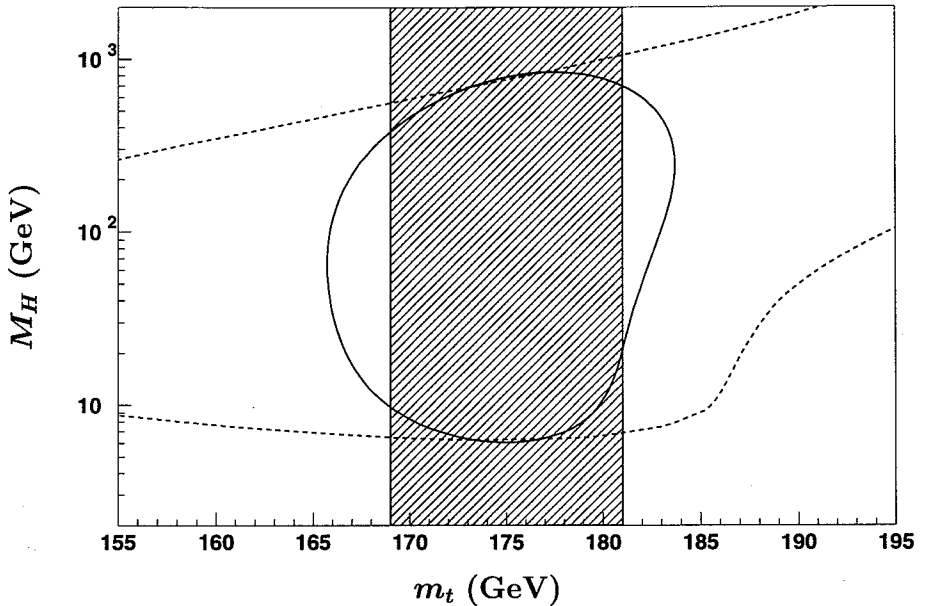
Figure 7.5: *Contours at 68% CL in the M_H-m_t plane around the central value with the constraint on m_t obtained from the combined CDF and D0 measurements (solid curve) and without (dashed curve). The combined CDF and D0 constraint on m_t is indicated by the hatched area.*

the luminosity) are rapidly becoming the limiting factor; for the off-peak data (and thus for the line shape parameters) further statistical improvements are possible. For the hadronic forward-backward charge asymmetry there is still plenty of room for improvement, both systematically and statistically. Part of these improvements will come "automatically" from the analysis of the data collected in 1994 and 1995. Not only will these data yield a statistical increase of approximately a factor 2.5, the fact that they are (in particular for L3) taken with an improved central tracking detector (the Silicon Micro-vertex Detector) should substantially increase the precision on the track transverse momentum, p_T, one of the most crucial variables for the hadronic forward-backward charge asymmetry measurement. The net effect should be a reduction of the statistical error on $A_{\mathrm{FB,h}}^{ch}$ by at least a factor of two. Also the systematic error on the forward-backward charge asymmetry can be improved, either by running more Monte Carlo events – if one wants to keep relying on the weighting method as used here – or by resorting to other, less Monte Carlo dependent, methods (e.g. the $< Q_{\mathrm{FB}} >$ one) if one is willing to accept their statistical consequences.

A more broader question concerns the continuing need to run on and around the Z peak to further confirm the Standard Model and to increase the precision on its parameters. To some extent the answer to this question has already been given. At CERN the Z peak region data collection has been stopped (at least for the time being) and LEP has moved into its LEP-2 phase. Runs on the Z peak have become calibration runs. Hints of possible small Standard Model violations have disappeared as the analysed data samples grew larger. For some parameters (sub)permille precisions have been reached. Time appears indeed to have come to take our checking of the Standard Model and the determination of its parameters into the energy region above the W^+W^- threshold using LEP-2 and the Fermilab TEVATRON and – for the future – into the energy region which is going to be laid open by the Large Hadron Collider.

Appendix A

TEC Hit Smearing

The distribution of the weighted distance d_{hit} (see chapter 3) in the ideal Monte Carlo has to be adapted to the data. In principle, this can be realised by a smearing based on the width of the distribution. Fitting a Gaussian to the distribution in the data and Monte Carlo leads to the widths σ^{dat} and σ^{MC}, and to a correction quantity

$$\sigma^{corr} = \sqrt{(\sigma^{\text{dat}})^2 - (\sigma^{\text{MC}})^2}. \tag{A.1}$$

The idea of a Gaussian smearing is rather simple: for each point $x = d_{\text{hit}}$, a Gaussian random number r is generated, and x replaced by

$$x^{new} = x + \sigma^{corr} * r \tag{A.2}$$

As can be seen from figure 3.8 however, fitting a single Gaussian to the distribution d_{hit} leads to a very large χ^2/df, mainly as a result of the non-reproduced distribution tails. The solution is to fit a double Gaussian distribution (see figure A.1), leading to a much better χ^2/df. The double Gaussian reads

$$f_1 \exp\left[-\frac{1}{2}\left(\frac{x}{\sigma_1}\right)^2\right] + f_2 \exp\left[-\frac{1}{2}\left(\frac{x}{\sigma_2}\right)^2\right], \tag{A.3}$$

where σ_1 and σ_2 are the widths of the two Gaussians and f_1 and f_2 their amplitudes. By convention, we constrain $\sigma_1 < \sigma_2$. The relative area A_1 of the first Gaussian with respect to the sum of the areas is given by:

$$A_1 = \frac{f_1 \sigma_1}{f_1 \sigma_1 + f_2 \sigma_2}, \tag{A.4}$$

and a similar expression for the relative area A_2 of the second Gaussian.

The double Gaussian smearing technique requires fitting a double Gaussian both to the measured data (leading to σ_1^{dat}, σ_2^{dat}, f_1^{dat} and f_2^{dat}) and to the Monte Carlo data (leading to σ_1^{MC}, σ_2^{MC}, f_1^{MC} and f_2^{MC}). Subsequently the "thin" Gaussian in Monte Carlo is smeared with

$$\sigma_1^{corr} = \sqrt{(\sigma_1^{\text{dat}})^2 - (\sigma_1^{\text{MC}})^2}, \tag{A.5}$$

and the "broad" Gaussian with

$$\sigma_2^{corr} = \sqrt{(\sigma_2^{\text{dat}})^2 - (\sigma_2^{\text{MC}})^2}. \tag{A.6}$$
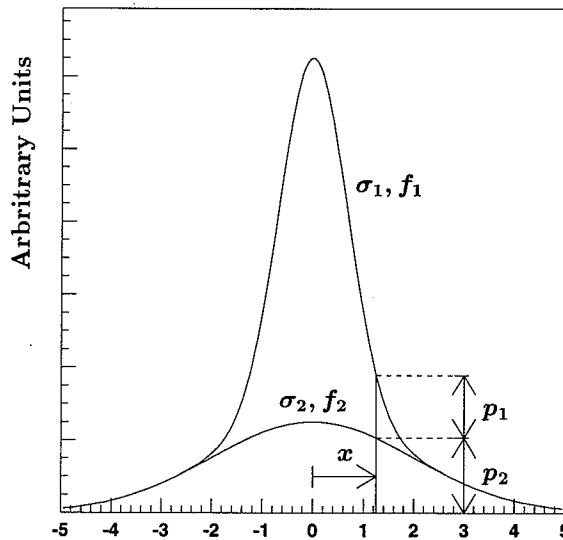
Figure A.1: *The double Gaussian smearing.*

The correction of the variable d_{hit} requires a more complicated formula than the one given by A.2, because of a dependence on the value $x = d_{\text{hit}}$ itself: the smaller the variable $|x|$, the higher the probability p_1 that the hit lies on the thin Gaussian and conversely, the higher $|x|$, the higher the probability p_2 that it lies on the broad Gaussian. The situation is drawn in figure A.1.

The probability p_1 that the thin Gaussian has to be used, is given by

$$p_1 = \frac{f_1 \exp\left[-\frac{1}{2}\left(\frac{x}{\sigma_1}\right)^2\right]}{f_1 \exp\left[-\frac{1}{2}\left(\frac{x}{\sigma_1}\right)^2\right] + f_2 \exp\left[-\frac{1}{2}\left(\frac{x}{\sigma_2}\right)^2\right]} \tag{A.7}$$

with a similar expression for the probability p_2. A uniform random number y is generated, and if $p_1(x) < y$, the smearing is applied using σ_1^{corr}; if on the other hand $p_2(x) > y$, one uses σ_2^{corr}.

A complication occurs, because both for the inner and outer TEC $A_1^{\text{dat}} > A_1^{\text{MC}}$. In order to obtain the proper relative areas in the real Monte Carlo, a fraction of the "thick" Gaussian, given by the relative difference $1 - (A_2^{\text{dat}}/A_2^{\text{MC}})$, is smeared with

$$\sigma_{12}^{corr} = \sqrt{(\sigma_1^{\text{dat}})^2 - (\sigma_2^{\text{MC}})^2}. \tag{A.8}$$

and the remaining fraction with A.6. The procedure then encounters a second complication if $\sigma_1^{\text{dat}} < \sigma_2^{\text{MC}(1)}$. This is the case for the inner TEC. To overcome the latter complication, use is made of the fact that the relative areas before and after smearing are slightly different because of statistical fluctuations. The method is to constrain the Monte Carlo relative area A_1^{MC} when determining first σ_1^{MC} and σ_2^{MC} before smearing, then perform the smearing and next redetermine A_1^{MC}, σ_1^{MC} and σ_2^{MC} after smearing. This procedure is performed for several initial A_1^{MC} choices, and the set yielding the best agreement with the data after smearing is retained. For consistency reasons the outer TEC smearing is treated the same way.

Table A.1 shows the values of σ_1, σ_2 and A_1 for data and Monte Carlo before

	parameter	σ_1	σ_2	A_1	χ^2/df
INNER TEC	data	0.621(8)	1.47(4)	0.646(9)	2.9
	MC ideal (before)	0.644(3)	0.966(5)	0.667(-)	1.5
	MC real (after)	0.648(10)	1.30(3)	0.634(15)	1.0
OUTER TEC	data	0.646(3)	1.409(14)	0.673(4)	4.4
	MC ideal (before)	0.566(1)	0.839(2)	0.719(-)	8.1
	MC real (after)	0.655(4)	1.349(16)	0.674(6)	0.8

Table A.1: *The widths and areas for the Gaussians used in the smearing of the distribution d_{hit}.*

and after the smearing. Note that for the data, the χ^2/df values, although orders of

---

[1]This problem can also be present in the single Gaussian smearing technique.

magnitude better than for a single Gaussian, are still not adequate due to remnant non-reproduced tail-effects[2]. The Monte Carlo χ^2/df for the outer TEC however shows a substantial improvement after smearing.

---

[2]In principle, this could be overcome by a smearing with three Gaussians. However, when aiming for a better smearing (i.e. a smearing which does give a better reproduction of the tails), the first step would not be to increase the number of Gaussians but to make the smearing ϕ_{local} dependent.

Appendix B

The Event Weighting Method

The event weighting method is a technique used to divide the members (in our case: the events) of a sample over different categories without making an unambiguous choice for each member (event) individually. Each event just receives a weight (in most cases: a probability) of belonging to a specific category, thus leading to a *statistical* separation of the sample rather than to an event-by-event separation. The application of this method to particle physics problems was discussed and examined in some detail by R. Barlow [46].

To illustrate the functioning and the utility of the weighting method, Barlow considered the simple case of the separation of a sample, obtained as a function of some variable x, in a signal and background component (see figure B.1). A standard procedure to extract a signal from such a plot is to make cuts on the x-variable. However, in a situation as depicted in figure B.1, cuts are a very crude tool. Placing the cuts at the tails of the signal peak would lead to the inclusion of a large amount of background; making the cuts narrower on the other hand, would lead to a significant loss of signal. The weighting method tries to solve this problem by starting from the obvious fact that the x-behaviour of the signal and the background are different and that it is therefore possible to apply a weight function to each event which enhances the signal vis-a-vis the background, i.e. to apply a function which is large, where the signal is large, intermediate when both signal and background are contributing and small where there is little or no signal. For example, in the situation of figure B.1, a multiplication of each event with a weight $w(x) = x$ would clearly enhance the signal and suppress the background, and obviously, $w(x) = 1-(x-0.5)^2$ would do this even better[1]. Making the crucial assumption that the behaviour of the background, as a function of x, is sufficiently well known (e.g. via extensive Monte Carlo calculations) Barlow goes on to prove that one can then "statistically" separate the signal and background sample (see formulae below) and that the results thus obtained are in

---

[1] Although – without further calculations – we cannot quantify *how* much better.
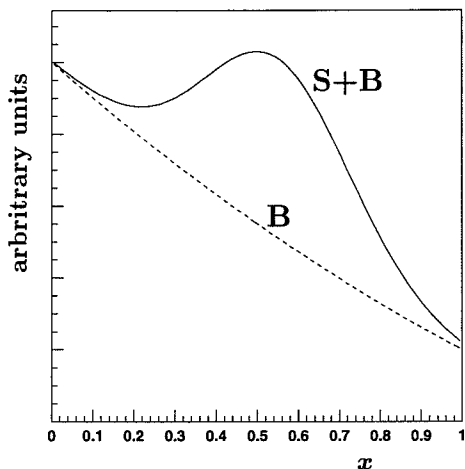
Figure B.1: *The problem of the separation of a signal from the background. The signal S (the solid line) is plotted on top of the background B (the dashed line).*

general statistically superior to those following from using straight cuts. The Barlow paper referred to above also compares the weight method with the in principle most powerful statistical method, the maximum likelihood technique. His conclusion is that in many situations, the weighting method is easier to interpret and understand while, statistically speaking, it yields nearly always as good a result.

The choice of the x-variable, the discriminator, and its physical interpretation is of no direct relevance for the analysis; the only important feature it should possess is that signal and background behave differently when expressed as a function of x. Note that x can be (and in most cases is) a multi-dimensional variable, e.g. a vector or a set of vectors. Actually it is in those circumstances that the weighting method often becomes more transparent than the maximum likelihood technique, because it reduces many distributions to a function of just one variable, the weight $w(x)$ (see figures 6.4 and 6.5).

For our analysis the plots at hand are not of the figure B.1 type, but as shown in figure B.2 (see figures 6.2 and 6.3), i.e. plots which are even more problematic in terms of the usage of cuts. The signal (i.e. the forward events) and the background (i.e. the backward events) distributions have the same shape, the only difference being that in the region $x > 0$ there is somewhat more signal over background than for the $x < 0$ region. There appears to be no straightforward way to separate the

signal from the background just using cuts[2] and relying on the weighting method is not just a possible but a necessary alternative.
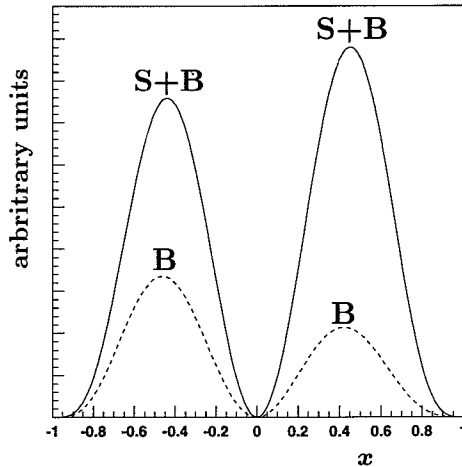

Figure B.2: *Signal and background for a typical plot in the forward-backward asymmetry analysis. The signal S (the solid line) is plotted on top of the background B (the dashed line).*

Applying the weighting method to our separation problem we face three questions:

- How is the signal extracted?

- How are the errors on the extracted signal calculated?

- How does one choose the best weight function?

The extraction of the signal is quite straightforward. Calling the number of signal and background events N_S and N_B respectively, the *unweighted* event total (designated by N_U) and the *weighted* event total (designated by N_W) are then given by:

$$N_U = N_S + N_B, \tag{B.1}$$

$$N_W = \bar{w}_S N_S + \bar{w}_B N_B, \tag{B.2}$$

---

[2]Note that for the purpose of illustration, the negative-positive x region difference has been exaggerated as compared to the situation displayed in figure 6.2, where the peak height differences are considerably less pronounced than in figure B.2.

where $\bar{w}_S$ and $\bar{w}_B$ are the average weights for the signal and background events respectively. Assuming that the knowledge of the dependence of the signal and background on x, i.e. the functions $w_S(x)$ and $w_B(x)$ have been determinated by Monte Carlo calculations, these averages are given by:

$$\bar{w}_S = \frac{1}{N_S^{\text{MC}}} \sum_{n=1}^{N_S^{\text{MC}}} w(x_n), \quad \bar{w}_B = \frac{1}{N_B^{\text{MC}}} \sum_{n=1}^{N_B^{\text{MC}}} w(x_n), \tag{B.3}$$

where N_S^{MC} and N_B^{MC} are the number of signal and background events in the Monte Carlo sample. Solving equations B.1 and B.2 yields an estimate for the number number of signal events:

$$\hat{N}_S = \frac{N_W - \bar{w}_B N_U}{\bar{w}_S - \bar{w}_B} = \frac{\sum_n [w(x_n) - \bar{w}_B]}{\bar{w}_S - \bar{w}_B}. \tag{B.4}$$

As the expectation value of $\hat{N}_S - N_S$ is zero, the $\hat{N}_S$ estimate is unbiased. A different weight function will therefore lead to the same number of signal events; only its error (see below) might be either larger or smaller. Note that N_S and N_B might refer to all the data in the sample or just to the number of events falling in one bin of a histogram[3].

The error on the number of signal events depends on the actual conditions of the experiment and on the quantity one is seeking to estimate. In general, these conditions can be arranged in several classes, each class with its own error evaluation. Our case corresponds to the situation in which the total number of events is fixed but the signal and background numbers follow a binomial distribution. Thus N_U is fixed and the error on $\hat{N}_S$ is given by

$$\begin{aligned} \text{Var}\left(\hat{N}_S\right) &= \frac{N_S N_B}{N_U} + \frac{N_S[\bar{w}_S^2 - (\bar{w}_S)^2] + N_B[\bar{w}_B^2 - (\bar{w}_B)^2]}{(\bar{w}_S - \bar{w}_B)^2} \\ &\equiv \frac{N_S N_B}{N_U} + X. \end{aligned} \tag{B.5}$$

The first part of B.5 is just the variance of a binomial distribution for fractions N_S/N_U and N_B/N_U. The second part, denoted by X, depends on the choice of the weight function.

Obviously, the optimal weight function is the one which minimises X. Evaluating the variation $\delta(X)$ as a function of $\delta w(x)$ around the minimum, one finds (see reference 46):

$$[w(x)]_{optimal} = \frac{N_S \cdot s(x)}{N_B \cdot b(x) + N_S \cdot s(x)}, \tag{B.6}$$

---

[3] The latter will actually be our case, as we will use the method to split samples of events falling into different thrust axis angle $|\cos\theta_T|$ bins.

where $s(x)$ and $b(x)$ are the normalised x-distributions for signal and background, respectively. Equation B.6 can be interpreted as the probability that an event is part of the signal: all weights obtained are between 0 and 1 and for any given x, the number of signal and background events having this x-value is given by $N_S s(x)$ and $N_B b(x)$ respectively. Note that the numerator of equation B.6 exactly represents the solid (S+B) curves of figures B.1 and B.2.

A problem related to the choice of the optimal weight function as defined by equation B.6 is that it depends on N_S and N_B, quantities which are a priori unknown as they are the ones to be measured to begin with. Considering a second order expansion around the minimum X in terms of the ratio N_S/N_B, it can be shown (see Barlow, reference 46) that the variation of X is almost negligible when N_S/N_B is not more different from the true ratio than a factor of ten. Thus a crude a priori knowledge (or estimate) of N_S/N_B is sufficient. In principle one could then still continue searching for the best weight function (i.e. the best separation) by an iterative procedure. However in the case of the forward-backward asymmetry an iteration is not necessary because this asymmetry is so close to zero. Starting from this assumption leads to errors which are (within a few percent) already optimal.

A few final remarks are in order. First, all the statements made above in terms of quality comparisons (with the cuts-method, the maximum likelihood technique, etc.) primarily apply to the statistical errors only. Inclusion of the systematic errors could modify them.

Second, the weighting method strongly depends on the crucial assumption that the x behaviour of both the signal and the background is well understood, or translated to our situation, that a good agreement is found between the data and the Monte Carlo distributions in terms of x. Thus the results of the weighting method are strongly dependent both on the quality of the Monte Carlo simulation and on the size of the Monte Carlo sample. As such this dependence on Monte Carlo simulation is not unusual. Also other methods have to rely on Monte Carlo e.g. to correct for the amount of signal lost by a cut, or to obtain a proper representation of the background contribution in the case of maximum likelihood fitting, etc. In the limit of infinite Monte Carlo statistics and a perfect agreement between data and Monte Carlo x distributions, the level of dependence on Monte Carlo would be irrelevant. When however these conditions are not satisfied, reliance on Monte Carlo becomes an important factor (and specifically, a significant source of systematic error). As shown in chapter 6, this is the case for our analysis[4].

---

[4]The $< Q_{\text{FB}} >$ method – see footnote 2 in chapter 1 – e.g. is able to derive some of the information – for which we have to rely on Monte Carlo – directly from the data itself; this reduces the systematic error following from a limited Monte Carlo sample. This same method however yields less optimal statistical errors.

Bibliography

[1] L. Montanet *et al.* , Phys. Rev. D50, 1173 (1994) and 1995 off-year partial update for the 1996 edition available on the PDG WWW pages (URL: http://pdg.lbl.gov/).

[2] P. Tipton, "Experimental Top Quark Physics", talk presented at ICHEP96, Warsaw, 25-31 July 1996, to appear in the proceedings.

[3] N. Watson, talk presented at the LEPC meeting, CERN, 8 October 1996.

[4] L.B.Okun, "Leptons and Quarks", Elsevier Science Publishers (1982).

[5] Contribution by the working group on Electroweak Radiative Corrections, in: "Z-Physics at LEP 1", Vol.1, eds. G. Altarelli, R. Kleiss and C. Verzegnassi, CERN 89-08.

[6] G. Raven, "Measurement of Invisible Z Decays", Ph.D. Thesis, Univ. of Utrecht (1995).

[7] F. Filthaut, "Hadronic Cross Section Measurements on the Z Resonance with the L3 Detector", Ph.D. Thesis, Univ. of Nijmegen (1993).

[8] OPAL Collaboration, "A Determination of $\sin^2 \theta_{\mathrm{W}}^{\mathrm{eff,e}}$ from an Inclusive Sample of Multihadronic Events, OPAL PN195.

[9] ALEPH Collaboration, D. Buskulic *et al.*, "Determination of $\sin^2 \theta_{\mathrm{W}}^{\mathrm{eff}}$ Using Jet Charge Measurements in Hadronic Z Decays", CERN-PPE/96-09, submitted to Z. Phys. C.

[10] Contribution by K. G. Chetyrkin, J. H. Kühn and A. Kwiatkowski, in: "Reports of the Working Group on Precision Calculations for the Z Resonance", eds. D. Bardin, W. Hollik and G. Passarino, CERN 95-03, 175.

[11] R. Kleiss, "Precision tests of the Electroweak Theory, Part II", in the Proceedings of the 1989 CERN-JINR School of Physics, Egmond-aan-Zee, CERN 91-07.

[12] Contribution by the working group on Forward-Backward Asymmetries, in: "Z-Physics at LEP 1", Vol.1, eds. G. Altarelli, R. Kleiss and C. Verzegnassi, CERN 89-08.

[13] Contribution by the Z Line Shape working group, in: "Z-Physics at LEP 1", Vol.1, eds. G. Altarelli, R. Kleiss and C. Verzegnassi, CERN 89-08.

[14] "ZFITTER, An Analytical Program for Fermion Pair Production in e^+e^- Annihilation", D.Bardin *et al.*, CERN-TH 6443/92.

[15] Contribution by the electroweak working group (D. Bardin *et al.*), in: "Reports of the Working Group on Precision Calculations for the Z Resonance", eds. D. Bardin, W. Hollik and G. Passarino, CERN 95-03, 7.

[16] The LEP Electroweak Working Group (J. Alcaraz *et al.*) and the SLD Heavy Flavour Group (G. Crawford *et al.*), "A Combination of Preliminary LEP and SLD Electroweak Measurements and Constraints on the Standard Model", L3 Internal Note 1975.

[17] T.Sjöstrand, "PYTHIA 5.6 and JETSET 7.3 Physics and Manual", CERN-TH.6488/92.

[18] B.Anderson, G.Gustafson and B.Söderberg, "A General Model for Jet Fragmentation", Z. Phys. C20 (1983) 317.

[19] C.Peterson *et al.*, "Scaling violations in inclusive e^+e^- annihilation spectra", Phys. Rev. D27 (1983) 105.

[20] E. Koffeman, "Luminosity determination in the L3 experiment", Ph.D. Thesis, Univ. of Nijmegen (1996).

[21] The working Group on LEP Energy and the LEP Collaborations ALEPH, DELPHI, L3 and OPAL, "Measurement of the mass of the Z boson and the energy calibration of LEP", L. Arnaudon *et al.*, Phys. Lett. B307 (1993) 187.

[22] The working Group on LEP Energy, "The Energy Calibration of LEP in 1992", L. Arnaudon *et al.*, CERN SL/93-21 (DI) (1993).

[23] The working Group on LEP Energy, "The energy calibration of LEP in the 1993 scan", R. Assmann *et al.*, Z. Phys. C66 (1995) 567.

[24] The working Group on LEP Energy, "LEP Energy Calibration in 1993, 1994 and 1995", LEP Energy Group/96-05.

[25] L3 Collab., B. Adeva *et al.*, "The construction of the L3 experiment", Nucl. Instr. and Meth. A289 (1989) 35.

[26] J. Wenninger, "Mesure de paramètres électro-faibles du Z avec la réaction $e^+e^- \to e^+e^-(\gamma)$", Ph. D. Thesis, University of Geneva (1992).

[27] Yu. Galaktionov et al., "The performance of a uranium gas sampling calorimeter", Nucl. Instr. and Meth. A251 (1986) 258.

[28] C. Timmermans, "Measurement of muon pair production around the Z-resonance using the L$_3$ detector at LEP", Ph. D. Thesis, Univ. of Nijmegen (1992).

[29] I. C. Brock et al., "Luminosity Measurement in the L3 Detector at LEP", CERN-PPE/96-89.

[30] R. Rosmalen, "A test of QED with $e^+e^- \to \gamma\gamma$ at LEP energies", Ph.D. Thesis, Univ. of Nijmegen (1994).

[31] A. Kunin, M. Maity and G. Majumder, "G-Factors", L3 Internal Note 1840.

[32] R. Brun et al., "GEANT3", CERN-DD/EE/84-1 (revised) (1987).

[33] O. Adriani et al., "Hadron Calorimetry in the L3 Detector", L3 Internal Note 854.

[34] G. Gratta, "The First BGO calibration with the RFQ", L3 Internal Note 1557.

[35] A. Biland, "Messung der Lebensdauer des τ-Leptons mit dem L3-Detektor", Diss. ETH Nr. 9970 ,Zürich (1992).

[36] B. Bouwens, "Measurement of the mean lifetime of B hadrons with the L3 detector", Ph.D. Thesis, Univ. of Amsterdam (1995).

[37] U. Uwer, private communication.

[38] S. Jadach and Z. Wạs, "Monte Carlo simulation of the process $e^+e^- \to \tau^+\tau^-$, $\tau^\pm \to X^\pm$ including radiative $\mathcal{O}(\alpha^3)$ QED corrections, mass and spin effects", Comp. Phys. Comm. 36 (1985) 191.

[39] M. Böhm, A. Denner and W. Hollik, "Radiative corrections to Bhabha scattering at high energies (I)", Nucl. Phys. B304 (1988) 687.

[40] J. H. Field, T. Riemann, "BHAGENE3, a Monte Carlo event generator for lepton pair production and wide-angle Bhabha scattering in e^+e^- collisions near the Z peak", Comp. Phys. Comm. 94 (1996), 53.

[41] F.A. Berends, R. Kleiss and P.H. Daverveldt, Leiden preprint "Complete Lowest Order Calculations for Four-lepton Processes in e^+e^- Collisions" (1984).

[42] C. Paus, private communication.

[43] Contribution by T. Sjöstrand on QCD generators, in: "Z Physics at LEP 1, Volume 3: Event Generators and Software", eds. G. Altarelli, R. Kleiss and C. Verzegnassi, CERN 89-08.

[44] JADE Collaboration, T. Greenshaw *et al.*, "A measurement of the charge asymmetry of hadronic events in electron positron annihilation", Z. Phys. C42 (1989) 1.

[45] OPAL Collaboration, P. D. Acton *et al.*, "A measurement of the forward-backward charge asymmetry in hadronic decays of the Z^0", Phys. Lett. B294 (1992) 436.

[46] R. Barlow, "Event Classification Using Weighting Methods", J. Comp. Phys. 72 (1987) 202.

[47] The LEP heavy flavour group, "Presentation of LEP Electroweak Heavy Flavour Results for Summer 1996 Conferences", L3 Internal Note 1969.

[48] L3 Collaboration, B. Adeva *et al.*, "Studies of hadronic event structure and comparisons with QCD models at the Z^0 resonance", Z. Phys. C55 (1992) 39.

[49] TASSO Collaboration, M. Althoff *et al.*, "A Detailed Study of Strange Particle Production in e^+e^- Annihilation at High Energy", Z. Phys. C27 (1985) 27.

[50] JADE Collaboration, "Charged Particle and Neutral Kaon Production in e^+e^- Annihilation at PETRA", Z. Phys. C20 (1983) 187.

[51] QCD Working Group, "QCD Event Generators", A. Blondel *et al.*. (to be published) and A. Nippe, private communication.

[52] B.C.C. van der Zwaan, "Experimental Study of Mixing and Asymmetry in $Z \to b\bar{b}$", Ph.D. Thesis, University of Nijmegen (1995).

[53] A. Blondel *et al.*, "An Investigation of the Interference between Photon and Z-Boson Exchange", L3 Internal Note 1812.

[54] W. Beenakker, F. A. Berends and S. C. van der Marck, "Large-angle Bhabha Scattering", Nucl. Phys. B349 (1991) 323.

[55] F. James, MINUIT manual CERN–D506 (1992).

[56] L3 Collaboration,). Adriani *et al.*, "Measurement of $\Gamma_{b\bar{b}}/\Gamma_{\text{had}}$ from hadronic decays of the Z", Phys. Lett. B307 (1993) 237.

[57] L3 Collaboration, "Measurement of the $B^0 - \bar{B}^0$ Mixing Parameter and the $Z \to b\bar{b}$ Forward-Backward Asymmetry", CERN-PPE/94-89 (1994).

[58] CHARM II Collaboration, P. Vilain *et al.*, "Precision measurement of electroweak parameters from the scattering of muon-neutrinos on electrons", Phys. Lett. B335 (1994) 246.

[59] ALEPH Collaboration, D. Decamp *et al.*, "Measurement of charge asymmetry in hadronic Z decays", Phys. Lett. B259 (1991) 377.

[60] DELPHI Collaboration, P. Abreu *et al.*, "A measurement of $\sin^2 \theta_W$ from the charge asymmetry of hadronic events at the Z^0 peak", Phys. Lett. B277 (1992) 371.

[61] DELPHI Collaboration, U. Flagmeyer, K. Hamacher, K. Münich and W. Neumann, "Measurement of the Inclusive Charge Flow in Hadronic Z Decays", DELPHI 96-19 PHYS 594.

[62] L3 Tau Analysis Group, O. Adriani *et al.*, "A Measurement of τ Polarisation", L3 Internal Note 1637 (1994).

[63] S. Bethke, "Summary of α_s Measurements", Proceedings of the QCD '94 Conference, Montpellier, France, Nucl. Phys. B (Proc Suppl) 39B,C (1995) 198.

[64] S. Eidelman and F. Jegerlehner, "Hadronic contributions to $(g-2)$ of the leptons and to the effective fine structure constant $\alpha(M_Z^2)$", Z. Phys. C67 (1995) 585.

[65] H. Burkhardt and B. Pietrzyk, "Update of the hadronic contribution to the QED vacuum polarisation", Phys. Lett. B356 (1995) 398.

[66] M. Lindner, "Implications of Triviality for the Standard Model", Z. Phys. C31 (1986) 295.

Summary

The subject of this thesis is the measurement of the cross section and the forward-backward charge asymmetry of the reaction $e^+e^- \rightarrow q\bar{q} \rightarrow$ hadrons.

The process $e^+e^- \rightarrow q\bar{q}$ can be described by the Standard Model; the phase $q\bar{q} \rightarrow$ hadrons by phenomenological fragmentation and hadronisation models. At center-of-mass energies around and at the mass of the intermediate Z boson this reaction can be investigated thoroughly by means of the resonant process $e^+e^- \rightarrow Z \rightarrow q\bar{q}$, which leads to a copious production of the final state. This results in a very accurate measurement of the most important parameters of the Standard Model, in particular of the mass of the Z boson and of the mixing angle $\sin^2 \theta_W$, a quantity which parameterises the mixing of the electromagnetic current and the neutral weak current. This requires that the most important higher order processes – the so-called radiative corrections – are taken into account. In these corrections, the heavy top quark and the yet undetected Higgs particle play a role.

The measurement is performed with data recorded by the L3 detector, one of the four experiments around the LEP accelerator. In order to make precision measurements, a thorough calibration of the beam energies is performed. During the years 1992 and 1993, LEP produced about 1.3 million hadron events corresponding to a total integrated luminosity of $56pb^{-1}$. The L3 detector consists of a series of concentric subdetectors around the LEP beam pipe. Starting from the interaction point and going outwards, one meets a central tracking detector, an electromagnetic calorimeter, a hadronic calorimeter and muon drift chambers, the whole embedded in a large magnet producing a nearly homogeneous field of 0.5 T. By means of physics criteria, a trigger system decides if the event has to be read out. All desired events are written onto tape and with the reconstruction program a variety of event properties are calculated.

Simulation of events is necessary in order to take into account the consequences of the deficiencies and limitations of the detector. This is effectuated by means of Monte Carlo programs. The simulation takes place starting from the interaction of the incoming electron and positron up to and including the readout of the hits in the drift chambers and the energy depositions in the calorimeters. In order to measure cross sections, a simulation of the calorimeters is required and for a correct forward-backward charge asymmetry determination also a simulation of the central tracking detector. The latter simulation is realised by means of applying a smearing to the

135

hits simulated in this subdetector. In addition, hits which are too close to the anode and cathode planes are eliminated both in real and simulated tracks, before the definitive track parameters are calculated. The exclusion of tracks in certain sectors neutralises undesired local effects. These hit modifications result in a significantly improved description and simulation of the charged tracking detector.

The hadron events are selected by means of criteria based on calorimetric information. These criteria result in a high efficiency of about 99.2% and in a small contribution of the background processes. The total statistics for 1992 and 1993 thus consisted of 646,263 respectively 651,990 selected hadronic events. For the forward-backward charge asymmetry selection, the event has to have a two-jet shape and sufficient charge information. For the latter there have to be at least three charged tracks in each hemisphere, defined with respect to the thrust axis of the event. In turn, the three most energetic charged tracks must have a sufficient number of hits and their charge confusion must not be too large. These relatively severe criteria limit the statistics available for the determination of the forward-backward charge asymmetry to 166,333 hadronic events for the 1993 period.

From the selected hadron events the cross sections are calculated with a statistical accuracy of better than 2 to 3‰ for every value of the beam energy. After subtraction of the background, the cross sections are corrected with about 1‰ for the beam energy spread and with about 1.5‰ for the trigger inefficiencies. The corrections induce extra inaccuracies of about 0.3‰ in the measurement; other systematic errors are due to limitations and inaccuracies in the knowledge of the background (less than 0.5‰), the hadron selection (0.4 to 0.7‰) and the measurement of the integrated luminosity (6‰ for 1992 and 1.5‰ for 1993). At the Z peak and for the 1993 scan period, a total cross section is measured of $\sigma_{\mathrm{h}} = (30.25 \pm 0.06 \pm 0.06)$ nb.

The forward-backward charge asymmetries are calculated by means of a statistical separation of events. To each event a weight is assigned which is a function of the three most energetic charged tracks in each hemisphere. The weight represents the probability that the corresponding event is forward, i.e. the negatively charged quark travelled in the same direction as the incoming electron. By averaging these weights the fractions of forward and backward events can be calculated. The statistical uncertainty of this asymmetry is 0.006 (15%). The asymmetries obtained are corrected for small systematic shifts of the position of the interaction vertex and small errors on the parameters used in the hadronisation models. Systematic errors are mainly due to the limited Monte Carlo statistics (10%). For the Pre+P period, this results in a forward-backward charge asymmetry of $A_{\mathrm{FB,h}}^{ch} = 0.040 \pm 0.006 \pm 0.004$.

The measurements of the cross sections and forward-backward charge asymmetries are used to test the Standard Model. This requires that also cross section and forward-backward asymmetry data from the leptonic channels have to be used. The model independent fits result in a good agreement with the predictions of the Standard Model. The Z mass is measured as $M_Z = (91.1919 \pm 0.0039)$ GeV and its width as $\Gamma_Z = (2.5022 \pm 0.0054)$ GeV. The effective mixing angle derived from the hadronic

forward-backward charge asymmetries, $\sin^2 \bar{\theta}_W = 0.2327 \pm 0.0030$, agrees with the values obtained from other experiments and from the leptonic forward-backward asymmetries. Performing calculations in the framework of the Standard Model a strong coupling constant $\alpha_s = 0.1316 \pm 0.0082^{+0.0021}_{-0.0012}$, a measured electromagnetic coupling constant $\alpha_{\mathrm{QED}} = 1/(129.04 \pm 0.58^{+0.09}_{-0.22})$ and a top mass $m_t = (173^{+26+15}_{-31-9})$ GeV can be derived, all consistent with results obtained by other measurements. If variations of the strong coupling constant, the QED coupling constant and the top mass are constrained to the best experimental results presently available, an upper limit on the Higgs mass $M_H < 460$ GeV is derived at a confidence level of 68%.

Samenvatting

Meting van
Hadronische Werkzame Doorsnedes
en Asymmetrieën
op de Z Resonantie

Dit proefschrift behandelt de meting van de werkzame doorsnede en de voorwaarts-achterwaarts ladings-asymmetrie van de reactie $e^+e^- \to q\bar{q} \to$hadronen.

Het proces $e^+e^- \to q\bar{q}$ kan worden beschreven door het zgn. Standaard Model; de fase $q\bar{q} \to$hadronen door fenomenologische fragmentatie en hadronisatie modellen. Bij zwaartepunts-energiën in de buurt van en op de massa van het intermediair Z boson kan deze reactie zeer grondig worden onderzocht door de aanwezigheid van het resonante proces $e^+e^- \to Z \to q\bar{q}$, dat voor een overvloedige productie van de eindtoestand zorgt. Dit levert een zeer nauwkeurige meting op van de belangrijkste parameters van het Standaard Model, in het bijzonder van de massa van het Z boson en van de mengingshoek $\sin^2 \theta_W$, een grootheid die de opmenging van de electromagnetische wisselwerking en de neutrale zwakke wisselwerking parameteriseert. Een en ander vereist een inachtname van de belangrijkste hogere orde processen, de zogenaamde stralingscorrecties. In die correcties spelen de massa van de zware top quark en het nog niet waargenomen Higgs deeltje een rol.

De meting is gedaan aan de hand van data opgenomen door de L3 detector, een van de vier opstellingen rond de LEP versneller. Om precisie-metingen te verrichten, is een grondige calibratie van de bundel-energiën gedaan. Gedurende de jaren 1992 en 1993 heeft LEP in het L3 interactiegebied 1,3 miljoen hadron gebeurtenissen geproduceerd, overeenkomende met een geïntegreerde luminositeit van $56pb^{-1}$. De L3 detector bestaat uit een reeks concentrische subdetectoren om de LEP bundelpijp heen. Gaande van binnen naar buiten, ontmoet men achtereenvolgens een geladen sporen detector, een electromagnetische calorimeter, een hadronische calorimeter en de muon drift kamers; het geheel is ingebed in een zeer grote magneet die een bijna homogeen veld van 0,5 T produceert. Een trigger systeem beslist aan de hand

van fysica-criteria of de gebeurtenis uitgelezen moet worden. Vervolgens worden de gewenste gebeurtenissen naar band geschreven en met het reconstructieprogramma allerlei eigenschappen van deze gebeurtenissen berekend.

Simulatie van gebeurtenissen is noodzakelijk om de gevolgen van gebreken en beperkingen van de detector in aanmerking te kunnen nemen. Dit wordt gedaan door middel van zogenaamde Monte Carlo programma's. De simulatie vind plaats vanaf de interactie van het inkomende electron en positron tot en met het uitlezen van de "hits" in de drift kamers en de energiedeposities in de calorimeters. Om werkzame doorsnedes te meten is een simulatie nodig van het gedrag van de calorimeters en voor een correcte bepaling van de voorwaarts-achterwaarts ladings-asymmetrieën tevens een simulatie van de geladen sporen detector. Deze laatste is gerealiseerd door middel van het aanbrengen van een spreiding op de in deze subdetector gesimuleerde "hits". Daarnaast worden zowel in de echte als de gesimuleerde geladen sporen, "hits" die te dicht bij de anode- en cathodevlakken liggen en daardoor onnauwkeurig zijn, geëlimineerd alvorens de definitieve parameters van de geladen sporen te berekenen. Het uitsluiten van geladen sporen in bepaalde sectoren neutraliseert ongewenste locale effecten. Een en ander resulteert in een significant verbeterde beschrijving en simulatie van de het gedrag van de geladen sporen detector.

De hadron gebeurtenissen worden geselecteerd aan de hand van criteria gebaseerd op calorimetrische informatie. Deze criteria resulteren in een hoge efficientie van circa 99,2% en in een lage bijdrage van de achtergrond-processen. De totale statistiek voor 1992 en 1993 bestond aldus uit 646.263 respectievelijk 651.990 hadron gebeurtenissen. Voor de voorwaarts-achterwaarts ladings-asymmetrie selectie moet de gebeurtenis een twee-jet vorm hebben en voldoende ladingsinformatie bezitten. Voor dit laatste moeten zich in ieder jet-halfrond, gedefiniëerd ten opzichte van de drift-as van de gebeurtenis, tenminste drie geladen sporen bevinden. Vervolgens moeten de drie meest energetische onder deze sporen een voldoende aantal "hits" hebben en mag de onzekerheid op hun ladingsbepaling niet te hoog zijn. Deze relatief strenge criteria beperken de statistiek voor het bepalen van de voorwaarts-achterwaartse ladings-asymmetrie tot 166.333 hadron-gebeurtenissen uit de 1993 verzameling.

Uit de totale hadron verzameling worden werkzame doorsnedes afgeleid met een statistische nauwkeurigheid van beter dan 2 tot 3‰, voor iedere waarde van de bundel energie. Na het aftrekken van de achtergrond zijn de werkzame doorsnedes verder gecorrigeerd met circa 1‰ voor de spreiding van de bundelenergie en met circa 1,5‰ voor de trigger-inefficienties. De correcties introduceren extra onnauwkeurigheden van ongeveer 0.3‰ in de meting; daarnaast zijn er systematische fouten ten gevolge van beperkingen en onnauwkeurigheden in de kennis van de achtergrond (minder dan 0,5‰), de hadron selectie (0,4 tot 0,7‰) en de meting van de geïntegreerde luminositeit (6‰ voor 1992 en 2‰ voor 1993). Anderzijds blijkt de werkzame doorsnede geen tijdsafhankelijke drift te vertonen. Op de Z piek wordt voor de 1993 scan periode aldus een totale werkzame doorsnede gemeten van $\sigma_{\rm h} = (30,25 \pm 0,06 \pm 0,06)$ nb.

De voorwaarts-achterwaarts ladings-asymmetrieën worden berekend door een statistische scheiding van de gebeurtenissen. Als functie van de drie meest energetische geladen sporen in ieder jet-halfrond wordt aan ieder verschijnsel een gewicht toegekend welke de kans representeert dat het verschijnsel voorwaarts is, d.w.z. dat de negatief geladen quark zich in dezelfde richting beweegt als het inkomend electron. Door deze gewichten te middelen kunnen de fracties van voorwaartse en achterwaartse verschijnselen uitgerekend worden. De statistische nauwkeurigheid op deze asymmetrie bedraagt 0,006 (15%). De verkregen asymmetrieën worden gecorrigeerd voor kleine systematische verschuivingen in de positie van de interactievertex en voor kleine fouten in de parameters gebruikt in de hadronisatie modellen. Systematische fouten zijn in hoofdzaak afkomstig van de beperkte Monte Carlo statistiek (10%). Voor de Pre+P periode resulteert dit in een voorwaarts-achterwaartse ladings-asymmetrie van $A_{\mathrm{FB,h}}^{ch} = 0,040 \pm 0,006 \pm 0,004$ op.

De metingen van de werkzame doorsnedes en voorwaarts-achterwaarts ladings-asymmetrieën worden gebruikt om het Standaard Model te toetsen; daartoe moeten ook werkzame doorsnede en ladings-asymmetrie data afkomstig van de lepton kanalen worden meegenomen. De model-onafhankelijke fits resulteren in een goede overeenkomst met de voorspellingen van het Standaard Model. De Z massa wordt gemeten als $M_Z = (91,1919 \pm 0,0039)$ GeV en zijn breedte als $\Gamma_Z = (2,5022 \pm 0,0054)$ GeV. De effectieve mengingshoek afgeleid uit de hadron asymmetrieën, $\sin^2 \bar{\theta}_W = 0,2327 \pm 0,0030$, stemt overeen met de waardes verkregen via andere experimenten en via de leptonische ladings-asymmetrie data. Door vervolgens berekeningen uit te voeren uitgaande van de geldigheid van het Standaard Model, kan een sterke koppelings constante $\alpha_s = 0,1316 \pm 0,0082^{+0,0021}_{-0,0012}$, een electromagnetische koppelingsconstante $\alpha_{\mathrm{QED}} = 1/(129,04 \pm 0,58^{+0,09}_{-0,22})$ en een een top massa $m_t = (173^{+26+15}_{-31-9})$ GeV worden afgeleid, alle drie consistent met resultaten van andere metingen. Wanneer de variaties van de sterke koppelingsconstante, de QED koppelingsconstante en de top massa worden beperkt tot de resultaten van de op dit ogenblik "beste" experimentele metingen, kan binnen een waarschijnlijkheidsinterval van 68% een bovengrens op de Higgs massa van $M_H < 460$ GeV worden geplaatst.

Curriculum Vitae

De schrijver van dit proefschrift werd op 30 april 1969 geboren te Lommel in België. Vanaf 1981 bezocht hij het Bisschoppelijk College te Weert, wat resulteerde in het behalen van het diploma Gymnasium-B in 1987.

In september 1987 begon hij met de studie natuurkunde aan de Katholieke Universiteit te Nijmegen. In september 1988 behaalde hij zijn propaedeuse. Hij begon met het afdelingswerk op de vakgroep Theoretische Hoge Energie Fysica in 1990. Onder begeleiding van Prof. Dr. Ir. J.J. de Swart en Dr. R. Timmermans schreef hij zijn afstudeerscriptie, getiteld "Effective Range Analysis of Proton–Antiproton Scattering Data". Hij behaalde zijn doctoraal examen in september 1991. Daarnaast is hij gedurende 1988-1991 werkzaam geweest als student-assistent met als taak de werkcolleges voor natuurkunde en scheikunde studenten.

Gedurende de periode 1991-1995 was hij Assistent-In-Opleiding aan bovengenoemde universiteit, op de vakgroep Experimentele Hoge Energie Fysica. In het kader van zijn onderzoek was hij vanaf oktober 1991 gedetacheerd naar CERN te Genève, waar hij tot september 1993 verbleef. Hier leverde hij een bijdrage aan het L3 experiment en zette hij het onderzoek op, dat het onderwerp vormt van dit proefschrift.

In de daarop volgende periode heeft hij onder begeleiding van Prof. Dr. R.T. Van de Walle en Prof. Dr. E.W. Kittel zijn analyse van de L3-meetgegevens gedaan en het voorliggende proefschrift geschreven. In dezelfde periode was hij ook betrokken bij het onderwijs door het verzorgen van werkcolleges voor natuurkunde en scheikunde studenten.